Technical Transactions

Czasopismo Techniczne

Issue 7
Volume 2019 (116)

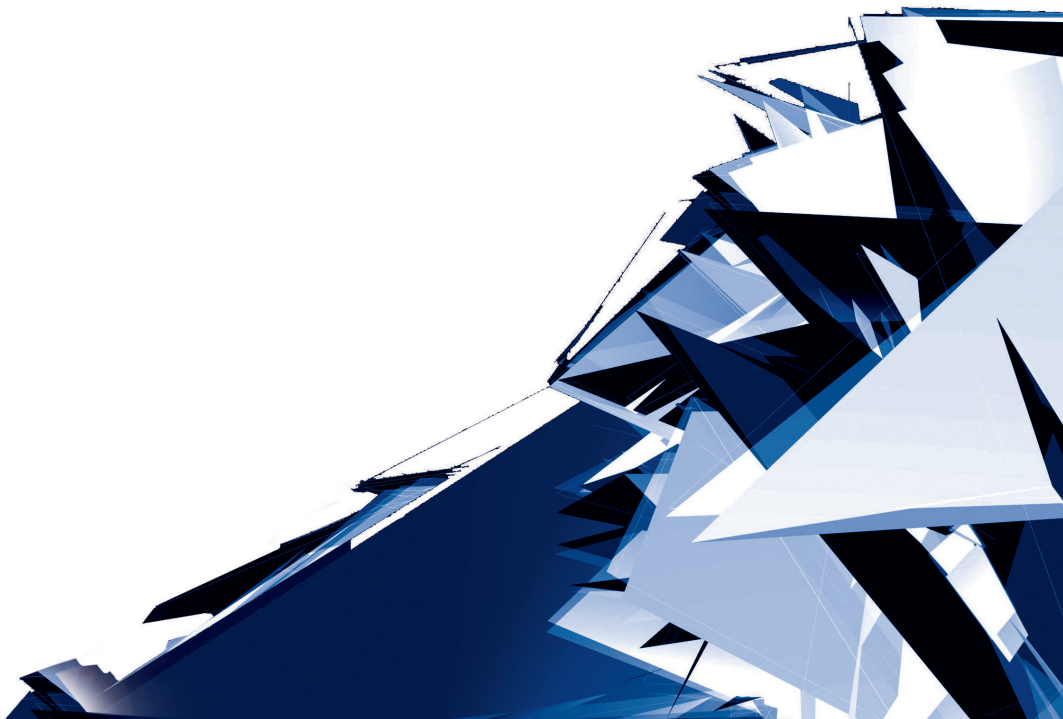

Basic version of each Technical Transactions magazine is its online version
Pierwotną wersją każdego zeszytu Czasopisma Technicznego jest jego wersja online

ISSN 0011-4561
eISSN 2353-737X

Contents

CIVIL ENGINEERING

TECHNICAL TRANSACTIONS 7/2019
CIVIL ENGINEERING
DOI: 10.4467/2353737XCT.19.067.10718
SUBMISSION OF THE FINAL VERSION: 7/07/2019

Akinori Akahoshi orcid.org/0000-0003-0918-3037
akahoshi@wei.co.jp
Wind Engineering Institute Co., Ltd., Japan
Yasushi Uematsu orcid.org/0000-0002-9186-7835
yasushi.uematsu.d8@tohoku.ac.jp
Department of Architecture and Building Science, Tohoku University, Japan

Criterion for wind environment assessment with consideration to the effect of turbulence

Kryterium oceny środowiska wiatrowego z uwzględnieniem wpływu turbulencji

Abstract

Turbulence affects the human perception of wind, the wind-induced damage to buildings, the values of wind speeds measured by 3-cup anemometers, and so on. The wind environment assessment criterion proposed by the Wind Engineering Institute Co., Ltd. is based on the relationship between the mean wind speeds measured by 3-cup anemometers and the condition of surrounding terrain. This criterion does not consider the influence of turbulence. Considering the significant urbanization of large cities and the change in anemometers used for wind speed measurements, a new criterion of wind environment assessment that considers the effect of turbulence is required. The present study discusses such a criterion based on a wind tunnel experiment, the observation at various locations, and a questionnaire survey on the wind environment that was conducted with for the residents and pedestrians in Tokyo.

Keywords: wind environment assessment, turbulence intensity, questionnaire survey, field observation, wind tunnel experiment

Streszczenie

Turbulencja wpływa na postrzeganie wiatru przez człowieka, wywołane wiatrem uszkodzenia budynków, wartości prędkości wiatru mierzone przez anemometry 3-filiżankowe etc. Kryterium oceny środowiska wiatrowego zaproponowane przez Instytut Inżynierii Wiatrowej opiera się na zależności między średnią prędkością wiatru mierzoną przez anemometry 3-filiżankowe a stanem otaczającego deszczu. To kryterium nie uwzględnia wpływu turbulencji. Biorąc pod uwagę znaczną urbanizację dużych miast i zmianę anemometrów używanych do pomiarów prędkości wiatru, wymagane jest nowe kryterium oceny środowiska wiatrowego, które uwzględnia wpływ turbulencji. Niniejszy artykuł omawia takie kryterium oparte na eksperymencie z tunelem aerodynamicznym, obserwacji w różnych miejscach oraz ankiecie dotyczącej środowiska wiatrowego, która została przeprowadzona dla mieszkańców i pieszych w Tokio.

Słowa kluczowe: ocena środowiska wiatrowego, intensywność turbulencji, badanie ankietowe, obserwacja w terenie, eksperyment w tunelu aerodynamicznym

1. Introduction

The criterion for wind environment assessment proposed by the Wind Engineering Institute Co., Ltd. (WEI), as shown in Table 1, has been used for several decades in Japan. This criterion is based on the relationship between the mean wind speeds measured by 3-cup anemometers and the condition of surrounding terrain with consideration to building heights and densities, as shown in Nakamura et al. [7]. However, the criterion doesn't consider the effects of turbulence on the human perception of wind. Wind turbulence significantly affects not only the human perception of wind but also the wind speed values measured by 3-cup anemometers. Therefore, the present study discusses the effects of turbulence on the current WEI criterion.

In recent years, the urbanisation of cities has progressed significantly, particularly in large cities such as Tokyo. This has resulted in a major change in public opinion concerning wind environment. In addition, ultrasonic anemometers that have lower cost and higher performance are becoming increasingly popular; these can precisely measure turbulence. In the light of these circumstances, the present study proposes a new criterion for wind environment assessment with consideration to the effect of turbulence, based on the results of field observation, a wind tunnel experiment, and a questionnaire survey on wind environment in Kamiosaki, Shinagawa-ku, Tokyo.

Table 1. WEI wind environment assessment criterion

Rank	Mean wind speeds at cumulative frequencies of 55% and 95%	
	55%	95%
A	≤ 1.2 m/s	≤ 2.9 m/s
B	≤ 1.8 m/s	≤ 4.3 m/s
C	≤ 2.3 m/s	≤ 5.6 m/s
D	> 2.3 m/s	> 5.6 m/s

2. Outline of field observation

The field observation of wind was performed at six points (MG1–MG6) close to the ground (3–5 m high) and at four points (MGO–MGR) on the rooftop of a high-rise building (Bldg. P, 115 m high) in Kamiosaki. Their locations are shown in Fig. 1. Ultrasonic anemometers were installed at MG1–3, and 3-cup anemometers were installed at MG4–6. A thermometer was installed at MG6. The period of the observation was from October 2016 to September 2017. The averaging time of the observation data was 10 minutes, and the instantaneous wind speed was obtained as a 3 second moving average. The wind speed values measured by the 3-cup anemometers were converted to these by ultrasonic anemometers, using the correction method proposed by Akahoshi et al. [1]. In order to obtain the rooftop observation data which is free from the effect of Bldg. P, the most appropriate data among those at MGO–R

was selected for each wind direction. The selection of the point for each wind direction was determined on the basis of the results of a CFD analysis and a wind tunnel experiment. The selected observation point is referred to as point 'MGZ'.

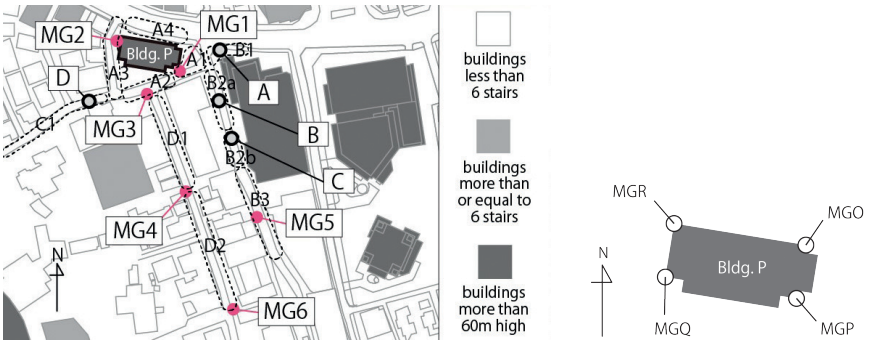

Fig. 1. Location of observation points, measurement points of wind tunnel experiment (selected) and areas of questionnaire

3. Outline of results of wind tunnel experiment

In the wind tunnel experiment, the wind speed ratio, gust factor, and turbulence intensity were measured at many points in Kamiosaki using hot-wire anemometers. The scale of the model was 1/400. The boundary layer was modelled on Category IV specified in the AIJ recommendations (2015). The reference point for these values was MGZ. In Fig. 2, these values are compared with the values obtained at the same locations in the field observation. The dashed line represents an approximate line obtained by applying the least squares method. Strong agreement is observed for the mean wind speed ratio. However, the experimental results for the gust factor and turbulence intensity are generally smaller than the observed results by approximately 20%. One of the reasons for this discrepancy is considered to be that the turbulence intensity of the inflow in the wind tunnel was smaller than that of the flow at full-scale.

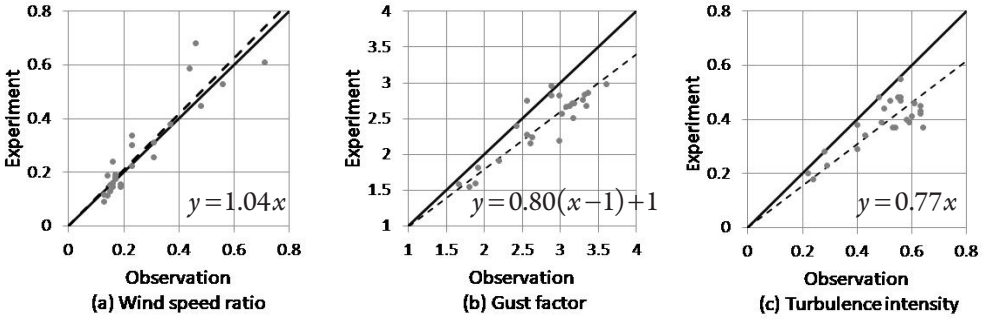

Fig. 2. Comparison for wind speed ratio, gust factor and turbulence intensity between the experiment and the field observation

4. Outline of questionnaire survey on wind environment

The questionnaire survey on the wind environment conducted with the pedestrians and residents in Kamiosaki consisted of three questions referring to Murakami et al. [5]. The details of the questions are provided in Table 2. The respondents were required to select one of the eleven areas (A1–D2) shown in Fig.1 and answer the questions in that area on as many days as possible. The appropriate period of time for evaluating the human perception of wind was not clear. Therefore, it was initially defined as one day referring to Murakami et al. [5]. There were thirty-eight respondents for the questionnaire, and 3664 answers were obtained during the period from May 2016 to October 2017. The number of answers to each question is shown in Fig. 3. Although the age and gender of respondents may affect these answers, this was not considered in this paper.

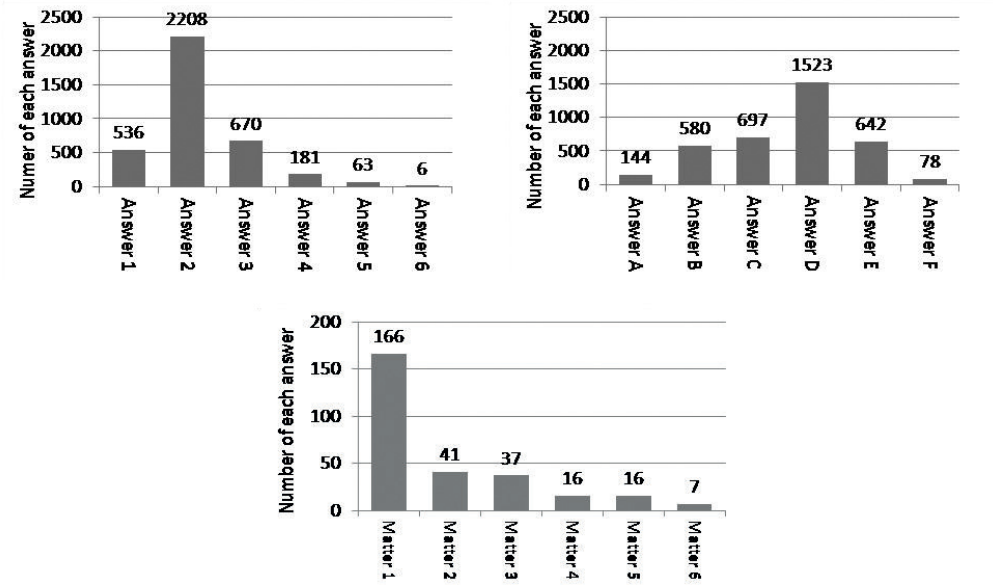

Fig. 3. Number of answers to each question

Table 2. Details of the questions

Question 1: "How was the wind strength today?"
Answer 1: calm
Answer 2: moderate
Answer 3: slightly strong
Answer 4: strong and uncomfortable
Answer 5: rather strong
Answer 6: dangerously strong

Question 2: "How was the temperature of wind today?"
Answer A: unpleasantly hot
Answer B: slightly hot
Answer C: comfortable
Answer D: neither hot nor cold
Answer E: cold
Answer F: so cold as to feel pain
Question 3: "What kind of wind-induced discomfort did you experience or see today?"
Matter 1: dishevelment of hair and/or clothing
Matter 2: difficulty in walking or falling down
Matter 3: difficulty in using umbrella or breakage of umbrella
Matter 4: falling down of bicycles or motorcycles
Matter 5: blowing up or drift of dust
Matter 6: wind too strong to go out

5. Relationship between the results of field observation, wind tunnel experiment, and questionnaire survey

5.1. Relationship between the perception of wind strength, wind speed, and turbulence intensity

The relationship between the human perception of wind and the statistics of wind speed is discussed here using the results of the field observation and wind tunnel experiment discussed above. The correspondence between the observation points (MG1–6), the measurement points of experiment (A–D), and the area of questionnaire survey (A1–D2) are shown in Fig. 1.

Figure 4 shows the dependence of relative frequency of each answer to Question 1 on the daily mean wind speed and turbulence intensity. The relative frequency of each answer, $f_i(U,I_u)$, is defined by Eqn. (1):

$$f_i(U,I_u)=\frac{N_i(U,I_u)}{\sum_{i=1}^{6}N_i(U,I_u)} \tag{1}$$

where N is the number of answers to each question; U is the mean wind speed; and I_u is the turbulence intensity.

In Fig. 4, the warm colours represent a higher relative frequency of the answers, while cold colours represent a lower relative frequency. It was found that the number of people who feel the wind strongly increases as the daily mean wind speed and turbulence intensity increase.

Figure 4 shows a clear tendency of the relationship between wind speed, turbulence intensity and human perception, although there is a dispersion. The reason for this dispersion may be that the respondents answered the question based on the perception for some specific period of time, for example, within a few minutes, not 1-day. Therefore, it was necessary to identify the specific period for which the respondents experienced the perception of wind. Although the period of time could be presumed from the time at which the respondents answered, there

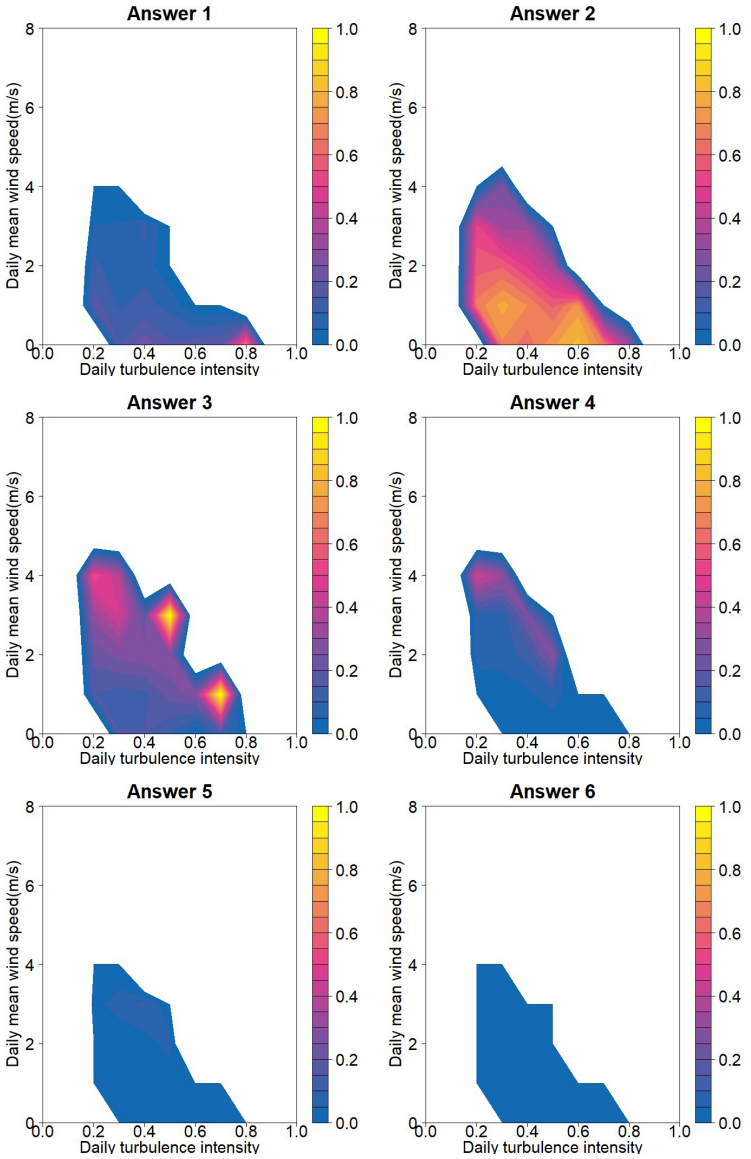

Fig. 4. Dependence of relative frequency of each answer to Question 1 on daily mean wind speed and turbulence intensity

are concerns about the error. In order to investigate this error, another questionnaire survey about the period of time for which respondents felt the perception was conducted from August 2017. The results of this survey showed that the respondents mostly answered the questions within one hour at most of when they experienced the perception. Therefore, the data of the questionnaire survey was reorganised as every 1-hour data, considering the uncertainty.

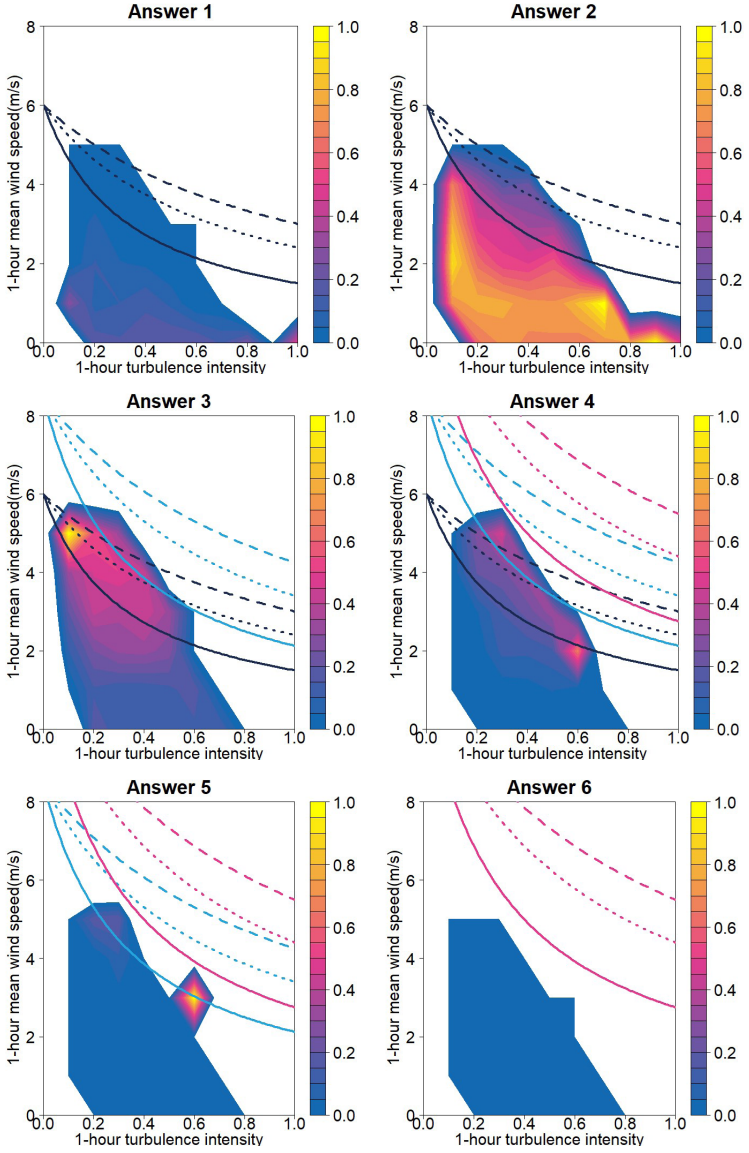

Fig. 5. Dependence of relative frequency of each answer to Question 1 on 1-hour mean wind speed and turbulence intensity (solid line: $k = 3$, dotted line: $k = 1.5$, dashed line: $k = 1$, black: $U_e = 6$ m/s, blue: $U_e = 8.5$ m/s, pink: $U_e = 11$ m/s)

Figure 5 shows the dependence of the relative frequency of each answer to Question 1 on 1-hour mean wind speed and turbulence intensity. The figure has less dispersion and shows the relation between them more clearly than Fig. 4. The curves in Fig. 5 represent the effective wind speeds U_e defined by Eqn. (2):

$$U_e = U + k\sigma_u = U(1 + kI_u) \tag{2}$$

where k is the weight coefficient, and σ_u is the standard deviation of the fluctuating wind speed.

Although we have not performed any statistical test, it seems that the curve corresponding to k = 3 correlates well with the data. Therefore, we tentatively propose this value of k in the following discussion. Figure 6 shows the relationship between the 1-hour effective wind speed with k = 3 and the relative frequency of each answer to Question 1. It is found that the relative frequency of Answers 1 and 2 (Answer 1+2) is the highest in the case where the 1-hour effective wind speed is lower than or equal to 6.5 m/s. Similarly, the relative frequency of Answer 3 is the highest in the case where the 1-hour effective wind speed ranges from 6.5 m/s to 9 m/s. The relative frequency of Answers 4 and 5 (Answer 4+5) is highest in the case where the 1-hour effective wind speed is higher than 9 m/s. These results are consistent with those of Hunt et al. [4], who showed that the effective wind speed corresponding to "For comfort and little effect on performance" is lower than 6 m/s. Similarly, they showed that the effective wind speed corresponding to "Most performance unaffected" is lower than 9 m/s. Furthermore, they explained that the upper limit of effective wind speed corresponding to "Control of walking" is 15 m/s. Based on the results mentioned above, the relationship between the perception of wind strength and the effective wind speed with k = 3 is proposed as shown in Table 3.

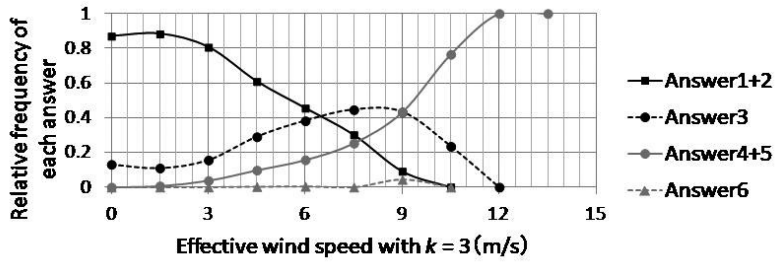

Fig. 6. Relationship between the effective wind speed with k = 3 and the relative frequencies of Answers 1–6

Table 3. Relationship between the perception of wind strength and the effective wind speed with k = 3

Effective wind speed	Perception of wind strength
$U_e \leq 6.5$ m/s	I : "agreeable"
6.5 m/s < $U_e \leq 9$ m/s	II : "slightly strong"
9 m/s < $U_e \leq 15$ m/s	III: "strong and uncomfortable"
$U_e > 15$ m/s	IV: "dangerous"

5.2. Relationship between the perception of the temperature of wind, the wind speed, and the air temperature

In this section, the dependence of the perception of the temperature of wind on the wind speed and the air temperature is discussed using the answers to Question 2. The subject of this discussion is the discomfort caused by low wind speed and high temperature. In this case, as pointed out by Murakami et al. (1985), it seems more appropriate to discuss this problem based on the mean wind speed, which corresponds to the effective wind speed with $k = 0$.

Figure 7 shows the relationship between the relative frequencies of Answers A–D and the mean wind speed when the temperature is higher than or equal to 25 °C. The relative frequency of Answers A and B (Answer A+B) is higher than those of Answers C and Answer D in the case where the mean wind speed when the temperature is higher than or equal to 25°C is lower than or equal to 1 m/s. Figure 8 shows the dependence of the relative frequencies of Answers D–F on the mean wind speed when the temperature is lower than 10°C. The relative frequency of Answers E and F (Answer E+F) is higher than that of Answer D in the case where the mean wind speed when the temperature is lower than 10 °C is higher than 0.5 m/s. Based on these results, the dependence of the perception of the temperature of wind on the mean wind speed and temperature may be provided as shown in Table 4.

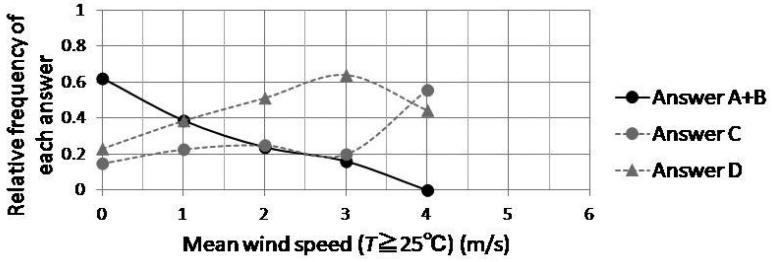

Fig. 7. Relationship between mean wind speed (air temperature is higher than or equal to 25°C) and relative frequency for Answers A–D

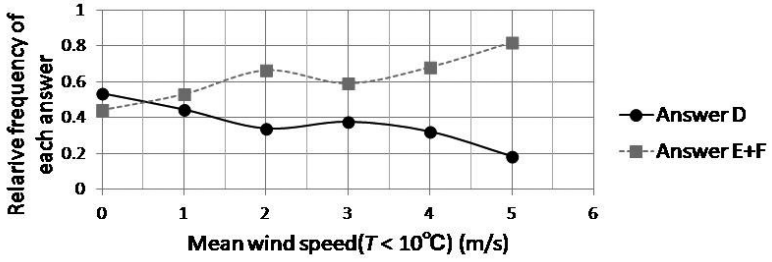

Fig. 8. Relationship between mean wind speed (air temperature is lower than 10°C) and relative frequency for Answers D–F

Table 4. Dependence of the perception of the temperature of the wind on the mean wind speed and air temperature

Mean wind speed and air temperature T	Perception of temperature of wind
$U \leq 1$ m/s ($T \geq 25$ °C)	a : "unpleasantly hot"
$U > 0.5$ m/s ($T < 10$ °C)	b : "it gets cold by the wind"

5.3. Dependence of wind-induced discomfort on the wind speed and the turbulence intensity

In this section, the dependence of wind-induced discomfort on the wind speed and the turbulence intensity is discussed, using the answers to Question 3. It may be appropriate to use the instantaneous wind speeds for this discussion. Note that the maximum instantaneous

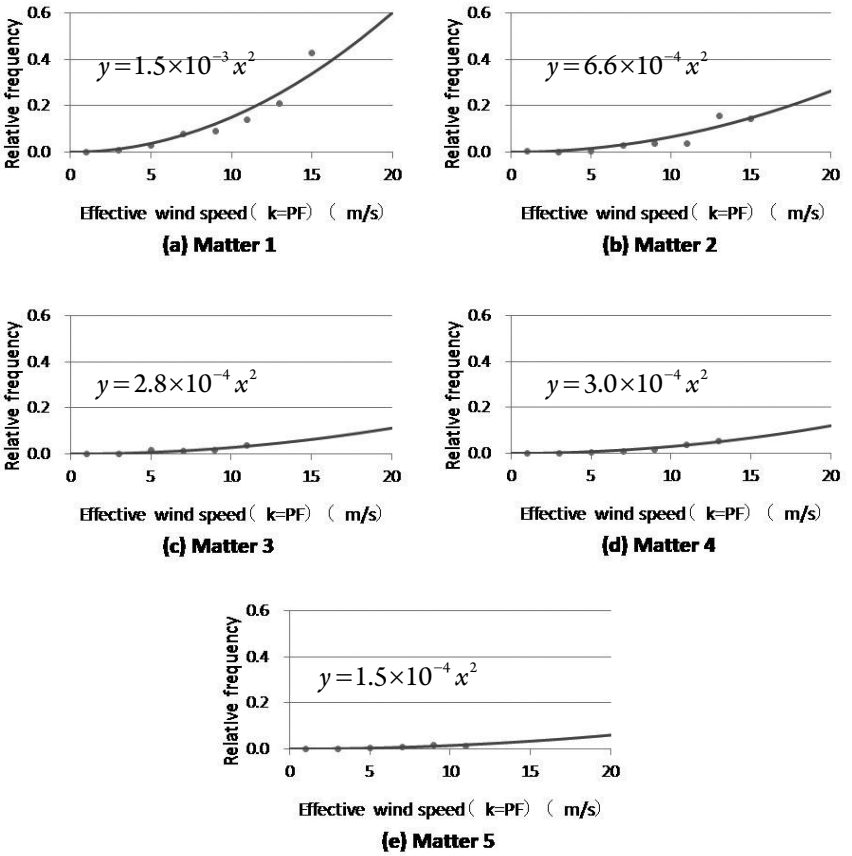

Fig. 9. Relationship between the effective wind speed with k = PF and the frequency of the wind-induced discomfort which respondents experienced or witnessed

wind speed corresponds to the effective wind speed with k = PF (peak factor). For the consistent again discussion, the effective wind speed with k = PF is used, although the maximum instantaneous wind speed can be obtained directly from the observation and experiment. In the present study, PF is provided by Eqn. (3), which is derived from an empirical formula proposed by Akahoshi et al. [2] based on the field observation at a height of 3 m above the ground. Note that this equation is a simplified form of the original:

$$g = 2.76\overline{I_u} + 2.77 \tag{3}$$

where g is a peak factor; and Iu represents 1-hour mean turbulence intensity.

The frequency of the wind-induced discomfort which the respondents experienced or witnessed is provided by Eqn. (4):

$$f_{e,i}(U_{e,PF}) = \frac{N_i(U_{e,PF})}{N(U_{e,PF})} \tag{4}$$

where $N_i(U_{e,PF})$ is the number of answers of Matter i at an instantaneous wind speed $U_{e,PF}$; $N(U_{e,PF})$ is the number of all answers at an instantaneous wind speed $U_{e,PF}$.

Figure 9 shows the relationship between the effective wind speed with k = PF and the frequency of the wind-induced discomfort which respondents experienced or witnessed.

Note that Matter 6 is excluded from the discussion because the number of answers is too small. The quadratic curve in each figure represents an empirical formula obtained by applying the least squares method to the plotted data. This result corresponds well to a finding by Nakamura et al. [8] that the frequency of the reports of human falling down by strong winds can be evaluated by the square of maximum instantaneous wind speed.

6. Proposed criterion for wind environment assessment with consideration to the effect of turbulence

6.1. Relationship between WEI criterion and the perception

Based on the results shown in Table 3 and 4, the relationship between the WEI criterion and the perception of wind is discussed. The mean wind speeds at a cumulative frequency of 55% and 95% were obtained from the field observation performed for one year at thirty-three observation points in urban area. In the same way, the relative frequencies of 1-hour effective wind speeds corresponding to the Perception I, I + II and I + II + III were obtained. Figure 10 shows the dependences of the mean wind speed at the cumulative frequencies of 55% and 95% on the cumulative frequency of the effective wind speeds corresponding to Perceptions I, I + II and I + II + III. In each figure, the solid line represents an empirical formula obtained by fitting the data, which is similar to the Weibull distribution. The vertical dashed lines represent the boundary values in the WEI criterion. From this figure, it is found that the mean wind speed at a cumulative frequency of 95% is stronger correlated with the cumulative frequency of effective wind speed than that at a cumulative frequency of 55%.

This may be due to the fact that the duration of stay of the respondents was relatively short. Therefore, in order to investigate the relationship between the perception of wind and the mean wind speed at a cumulative frequency of 55%, a longer duration of stay should be taken into account. Based on these results, the empirical formulae representing the relationship between the mean wind speed at a cumulative frequency of 95% and the perception of wind strength are proposed as follows:

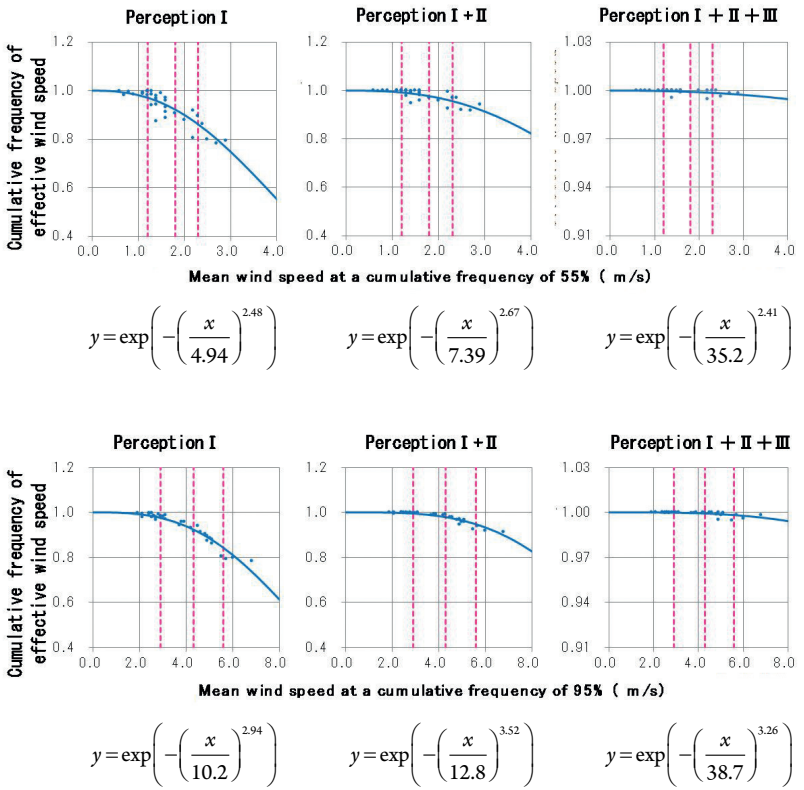

Fig. 10. Relationship between the mean wind speed at the cumulative frequencies of 55 % and 95 % and the relative frequency of effective wind speed corresponding to Perceptions I, I+II, I+II+III

$$F_1=\exp\left(-\left(\frac{U_{95}}{10.2}\right)^{2.94}\right) \tag{5}$$

$$F_{1+2}=\exp\left(-\left(\frac{U_{95}}{12.8}\right)^{3.52}\right) \tag{6}$$

$$F_{1+2+3}=\exp\left(-\left(\frac{U_{95}}{38.7}\right)^{3.26}\right) \tag{7}$$

where F_1, F_{1+2} and F_{1+2+3} are the cumulative frequencies of the effective wind speeds corresponding to the Perceptions I, I + II and I + II + III, respectively; U_{95} is the mean wind speed at a cumulative frequency of 95%.

Figure 11 shows the dependence of the mean wind speed at the cumulative frequencies and 55% and 95% when $T \geq 25°C$ on the relative frequency of the mean wind speed corresponding to Perception a (see Table 4). From the figure, it was found that the mean wind speed at a cumulative frequency of 55% is better correlated with the relative frequency of the mean wind speed than that at a cumulative frequency of 95%. The solid line represents an empirical formula obtained by fitting the data, which is similar to the Weibull distribution. The intercept of the approximate curve, 0.174, corresponds to the mean value of the relative frequency of temperature higher than or equal to 25°C obtained from the 33 observation points. Based on these results, an empirical formula representing the relationship between the mean wind speed at a cumulative frequency of 55% when $T \geq 25°C$ and the perception of the temperature of the wind is proposed by Eqn. (8):

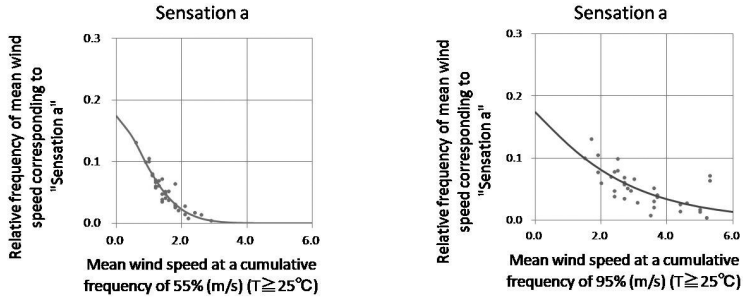

Fig. 11. Relationship between the mean wind speed at the cumulative frequencies of 55% and 95% and the relative frequency of mean wind speed corresponding to Perception a ($T \geq 25°C$)

$$F_a = 0.174 \exp\left(-\left(\frac{U_{55,T25}}{1.28}\right)^{1.59}\right) \tag{8}$$

where F_a is the relative frequency of the mean wind speed ($T \geq 25°C$) corresponding to Perception a; $U_{55,T25}$ is the mean wind speed at a cumulative frequency of 55% ($T \geq 25°C$).

6.2. New criterion

In this section, a new criterion for wind environment assessment with consideration to the effect of turbulence is proposed, using the results shown in the previous subsections. The new criterion is based on the effective wind speeds with $k = 0$ and $k = 3$.

Firstly, the criterion based on the effective wind speed with k = 3 is discussed. The cumulative frequencies of the effective wind speeds corresponding to the boundary values of the WEI criterion were provided by Eqs. (5)–(7) and the results are shown in Table 5. Furthermore, it was found that the effective wind speed followed the Weibull distribution, using the observation data at thirty-three observation points in the chosen urban area. Assuming that the relative frequency of the effective wind speed follows the Weibull distribution, the Weibull coefficients were obtained by using the least squares approximation; Table 5 presents the results. The effective wind speeds at a cumulative frequency of 95% corresponding to the boundary values of the WEI criterion were obtained from the Weibull distribution with the coefficients in Table 5; the results are summarised in Table 6.

Secondly, the criterion based on the effective wind speed with k = 0 is discussed. The ISO recommends that PPD (predicted percentage of dissatisfied) related to PMV (predicted mean vote) should be less than or equal to 10 %. In the present study, the effective wind speed, V, with k = 0 which makes the relative frequency of Perception a less than or equal to 10 %, is investigated. V is provided by Eqn. (9) assuming that coefficients in Eqn. (8) are constant regardless of the relative frequency of temperature higher than or equal to 25 °C:

$$V = 1.28\left\{-\ln\left(\frac{0.1}{P_{T25}}\right)\right\}^{0.63} \tag{9}$$

where P_{T25} is the relative frequency of temperature higher than or equal to 25°C (≥ 0.1).

The case where the effective wind speed at a cumulative frequency of 55% when $T \geq 25$°C is less than or equal to V is regarded as 'discomfort'.

The above discussion is based on the evaluating time of one hour. This should be changed to 10-minute values, because the WEI criterion is based on 10-minute values. A preliminary analysis of the data obtained at Thirty-three observation points indicated that the relative frequency of 1-hour effective wind speeds was almost the same as that of 10-minute effective wind speeds. Regarding the temperature, we obtained the similar result. Therefore, it is not necessary to convert the values obtained above to the 10-minute values.

Based on the above-mentioned results, the relationship provided in Table 6 is proposed as a new criterion for wind environment assessment with consideration to the effect of turbulence.

Table 5. Cumulative frequency of the effective wind speed corresponding to each perception, Weibull coefficients and boundary value of WEI criterion (95%)

WEI criterion		F_1	F_{1+2}	F_{1+2+3}	Weibull coefficient	
Rank	Boundary values (95%)				C	K
A	2.9 m/s	0.976	0.995	1.000	1.71	0.98
B	4.3 m/s	0.924	0.979	0.999	2.99	1.22
C	5.6 m/s	0.842	0.947	0.998	4.28	1.47

Table 6. Proposed criterion for wind environment assessment with consideration to the effect of turbulence

U_e with $k = 0$ at 55% cumulative frequency ($T \geq 25$°C)		U_e with $k = 3$ at 95% cumulative frequency	
discomfort	$\leq V$	Rank A	≤ 5.2 m/s
		Rank B	≤ 7.4 m/s
		Rank C	≤ 9.1 m/s
		Rank D	> 9.1 m/s

7. Comparison between new criterion and present criteria

A comparison between the new criterion proposed in the present study and the current criteria is made using the field observation data at thirty-three observation points in the urban area. Note that the current criteria refer to the WEI criterion shown in Table 1 and the criterion of Murakami et al. (1983) shown in Table 7.

Table 8 shows a comparison between the results evaluated by these criteria. Firstly, comparing the new criterion based on U_e with $k = 3$ and the WEI criterion, it is found that the evaluated results became worse at three points, for example, from A to B, while those at six points became better. This means that the evaluated results become better or worse by considering the effect of turbulence on the human perception. Secondly, according to the new criterion based on U_e with $k = 0$, the evaluated results at Points 17 and 33 are both 'discomfort'. At Point 33, the result evaluated by the WEI criterion is 'A', while by Murakami et al. criterion, it is 'rank 1'. Therefore, the wind is thought to be weak throughout the year. By contrast, at Point 17, the evaluated result by the WEI criterion is 'B', while by Murakami et al. criterion, it is 'rank 2'. This result indicates that the wind at Point 17 is weaker in summer than in other seasons. These results indicate that the new criterion proposed in the present study evaluates the wind environment more appropriately than the current criteria.

Table 7. Criterion of Murakami et al.

Rank	The exceeding probably of the daily maximum instantaneous wind speed		
	10 m/s	15 m/s	20 m/s
1	≤ 10 %	≤ 0.9 %	≤ 0.08 %
2	≤ 22 %	≤ 3.6 %	≤ 0.6 %
3	≤ 35 %	≤ 7 %	≤ 1.5 %
4	> 35 %	> 7 %	> 1.5 %

Table 8. Comparison between the evaluated results by the three criteria ('-' means that the evaluated result isn't 'discomfort')

Point No.	Evaluated results			
	WEI	Murakami et al.	new criterion	
			$k = 0$	$k = 3$
1	D	4	-	D
2	B	1	-	B
3	C	2	-	C
4	D	3	-	C
5	B	1	-	B
6	A	1	-	B
7	C	2	-	B
8	A	1	-	A
9	C	2	-	B
10	B	1	-	A
11	B	2	-	B
12	C	4	-	C
13	B	2	-	B
14	A	2	-	A
15	B	2	-	B
16	B	1	-	B
17	B	2	discomfort	B
18	C	3	-	C
19	C	4	-	D
20	D	4	-	D
21	C	2	-	C
22	B	1	-	A
23	A	1	-	A
24	C	3	-	C
25	D	4	-	D
26	C	2	-	B
27	A	1	-	A
28	B	1	-	A
29	B	2	-	B
30	A	1	-	B
31	A	1	-	A
32	A	1	-	A
33	A	1	discomfort	A

Table 9. Boundary values of each criterion which are redefined

Rank	WEI		Murakami et al.			new
	55 %	95 %	10 m/s	15 m/s	20 m/s	$k = 3$
1	≤ 0.40	≤ 0.97	≤ 3.33	≤ 0.30	≤ 0.03	≤ 1.73
2	≤ 0.80	≤ 1.93	≤ 6.66	≤ 0.60	≤ 0.06	≤ 3.46
3	≤ 1.20	≤ 2.90	≤ 10.0	≤ 0.90	≤ 0.08	≤ 5.20
4	≤ 1.40	≤ 3.37	≤ 14.0	≤ 1.80	≤ 0.25	≤ 5.93
5	≤ 1.60	≤ 3.84	≤ 18.0	≤ 2.70	≤ 0.42	≤ 6.66
6	≤ 1.80	≤ 4.30	≤ 22.0	≤ 3.60	≤ 0.60	≤ 7.40
7	≤ 1.97	≤ 4.73	≤ 26.3	≤ 4.73	≤ 0.90	≤ 7.97
8	≤ 2.13	≤ 5.16	≤ 30.6	≤ 5.86	≤1.20	≤ 8.54
9	≤ 2.30	≤ 5.60	≤ 35.0	≤ 7.00	≤ 1.50	≤ 9.10
10	> 2.30	> 5.60	> 35.0	> 7.00	> 1.50	> 9.10

In order to compare the results evaluated by the three criteria with each other in more detail, each criterion's boundary values are redefined by dividing them equally into 10 ranks, as shown in Table 9. Figure 12 shows a comparison between the evaluated results by the three criteria based on Table 9. It was found that the results evaluated by the new criterion approximately lie approximately between those by the WEI and the Murakami et al. criteria. This result indicates that the new criterion reflects the characteristics of both criteria.

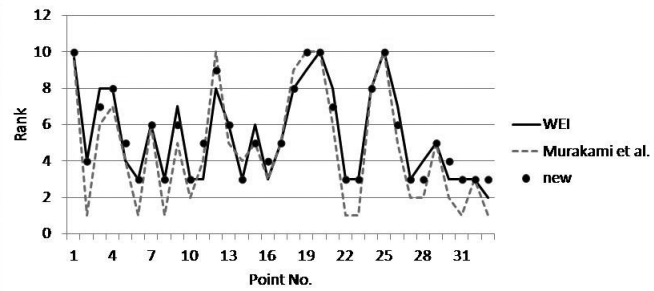

Fig. 12. Comparison between the evaluated results of three criteria by using the boundary values shown in Table 9

8. Conclusion

On the basis of the results of the field observation, the wind tunnel experiment, and the questionnaire survey in Kamiosaki, the relationship between the WEI criterion for wind environment assessment and the human perception of wind was investigated. In addition, a new criterion considering the effect of turbulence was proposed; this evaluates the wind environment more appropriately than the current criteria. However, it is necessary to improve this criterion by increasing the number of items of data in the field observation and in the questionnaire survey.

References

[1] Akahoshi A., Sarukawa A., Sasaki R., Miyashita K., Nakamura O., Uematsu Y., *Discussion on difference between 3 cup and ultrasonic anemometers of the obtained statistical values to be used for wind environment assessment*, Journal of Wind Engineering, JAWE, No.156, 2018.

[2] Akahoshi A., Sarukawa A., Sasaki R., Miyashita K., Nakamura O., Uematsu Y., *Study of relation between peak factor and turbulence intensity by using the wind observation data at various locations*, Journal of Wind Engineering, JAWE, No.153, 2017, 134–143.

[3] Architectural Institute of Japan, *Recommendation for Loads on Buildings*, 2015.

[4] Hunt J.C.R., Poulton E.C., Mumford J.C., *The effects of wind on people; New criteria based on wind tunnel experiments*, Building and Environment 11(1), 1976, 15–28.

[5] Murakami S., Iwasa Y., Morikawa Y., *Investigation of statistical characteristic of wind at ground level and criteria for assessing wind-induced discomfort: Part III Criteria for assessing wind-induced discomfort*, Transactions of the Architectural Institute of Japan 325, 1983, 74–84.

[6] Murakami S., Morikawa Y., *Criteria for assessing wind-induced discomfort considering temperature effect*, Transactions of AIJ, Journal of architecture, planning and environmental engineering 358, 1985, 9–17.

[7] Nakamura O., Yoshida M., Yokotani K., Katagiri J., *Characteristics of wind at ground level in Tokyo*, Proceedings of the 9th National Symposium on Wind Engineering, Tokyo 1986.

[8] Nakamura O., Tamura Y., Hibi K., Xu X., Yang Q., Miyashita K., *Proposal of Pedestrian Level Wind Index Based on Field Measurement Wind Speed Data at 320 Urban Sites in Japan*, Journal of Wind Engineering, JAWE, No.148, 2016, 103–111.

If you want to quote this article, its proper bibliographic entry is as follow: Akahoshi A., Uematsu Y., *Criterion for wind environment assessment with consideration to the effect of turbulence*, Technical Transactions, Vol. 7/2019, pp. 5–22.

TECHNICAL TRANSACTIONS 7/2019
CIVIL ENGINEERING
DOI: 10.4467/2353737XCT.19.069.10720
SUBMISSION OF THE FINAL VERSION: 5/06/2019

Katarzyna Baruch orcid.org/0000-0001-7982-3437
kbaruch@agh.edu.pl
Aleksandra Majchrzak orcid.org/0000-0003-3693-2953
Tadeusz Kamisiński orcid.org/0000-0002-8580-2402
Department of Mechanics and Vibroacoustics, Faculty of Mechanical Engineering and Robotics, AGH University of Science and Technology

Agata Szeląg orcid.org/0000-0002-9058-565X
Institute of Structural Mechanics, Faculty of Civil Engineering, Cracow University of Technology

An engineering method to measure structure-borne sounds transmitted through the building partitions

Metoda inżynierska pomiaru dźwięków materiałowych przenikających przez przegrody budowlane

Abstract

In this paper, the authors present an engineering method to identify the transmission paths of structure-borne sounds. The method is based on the use of a standardised impact sound source with an insulation case. The advantage of this approach is the possibility of obtaining repeatable results because the method allows the separation of structure-borne and airborne sounds; the latter do not interrupt the measurement even in the case of loose connections or elements of low acoustic insulation. The research on the verification of the method was performed on the façade of the Cracow Philharmonic building; the main structure-borne sound transmission paths were determined successfully. Knowledge of the sound transmission paths allows the subsequent design of efficient vibroacoustic protection.

Keywords: impact sound, vibrations, sound radiation

Streszczenie

W artykule zaproponowano inżynierską metodę identyfikacji dróg transmisji dźwięków przenoszonych drogą materiałową przy użyciu wzorcowego źródła dźwięków uderzeniowych z odpowiednią obudową dźwiękoizolacyjną. Zaletą tego podejścia jest możliwość uzyskania powtarzalnych wyników dzięki odizolowaniu dźwięków uderzeniowych od powietrznych, które nie zakłócają pomiaru w razie występowania nieszczelności lub elementów o niskiej izolacyjności akustycznej. W celu weryfikacji metody przeprowadzono badania budynku Filharmonii Krakowskiej – wyznaczono główne drogi transmisji dźwięków przenoszonych drogą materiałową. Ich znajomość jest niezbędna do projektowania skutecznej ochrony dźwiękoizolacyjnej.

Słowa kluczowe: dźwięk uderzeniowy, drgania, promieniowanie dźwięku

1. Introduction

In terms of building acoustics, sounds can be divided into two groups: sounds propagating in air (airborne sounds) and sounds propagating in solids such as the ground or the construction elements of buildings (structure-borne sounds). However, this distinction is not very rigorous since the airborne sounds may excite the construction of a building causing the formation of structure-borne sounds, and vice-versa – structure-borne sounds may induce airborne sounds in a gas medium (Fig. 1).

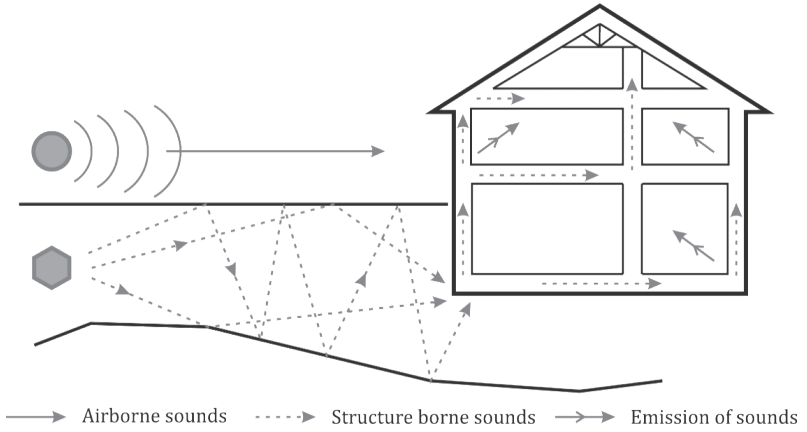

Fig. 1. Illustration of transmission paths for airborne and structure born sounds

Even though structure-borne and airborne sounds are strongly correlated, airborne sounds are much easier to be controlled and eliminated than structure-borne sounds because the transmission paths are usually clearly identified; the airborne sound transmission paths can be easily detected with standard measurement apparatus, specifically, sound pressure level meters. By contrast, the transmission paths of structure-borne sounds are very difficult to predict [4, 14]. Of course, there are a few methods which allow the determination of the structure-borne sound transmission paths; however, they have mostly been developed in the transportation industry – for example, experimental transfer path analysis (TPA) in the automotive industry [5, 13]. The TPA method is used for the analysis of the structure-borne sound transmission from point-coupled powertrains and wheel suspensions to vehicle bodies and for the analysis of transmission paths into vibration-isolated truck or tractor cabs, etc. The analysis of structure-borne sound transmission paths has also been developed in the railway industry [11, 12]; knowledge of structure-borne sound transmission paths enables effective noise protection in railway areas and prevents railway noise in the vicinity of newly designed railway routes.

In building acoustics, structure-borne sounds constitute a very important issue in all types of buildings; this is especially true in situations where the background noise level must be kept low, for example, in concert halls. Nevertheless, the determination of the structure-borne

sound transmission paths is very difficult. The main problem which is encountered during this type of measurement is the simultaneous emission of airborne sounds during the excitation of the partitions with an impact sound source [7]. Building partitions very often include numerous elements of relatively low acoustic insulation, such as windows and doors. These elements allow the transmission of airborne sounds which, in turn, disturb the measurement of structure-borne sound transmission paths. Analysis of the current literature reveals that there are some methods for the analysis of structure-borne sound transmission paths in buildings such as that described in the ISO 140-4 standard [9]. However, this procedure is complicated and demanding since all the building elements, except for the one under study, must be covered with isolating materials. This is especially troublesome in the case of large halls. Moreover, this method does not allow the determination of more complex sound transmission paths and it is applied only to sources of airborne sounds. A different approach to the measurement of structure-borne sound transmission paths proposed by other authors is the use of a hammer as a sound source in examining multilayer concrete structures [1]. This method, however, does not allow the isolation of structure-borne sounds from airborne sounds. This is why, in the following paper, the authors propose their own method of measuring structure-borne sounds transmitted through building partitions. This solution allows the isolation and measurement of structure-borne sounds; as a consequence, it is possible to determine structure-borne sound transmission paths.

2. Measurement methodology

The proposed method for the identification of structure-borne sound transmission paths is based on the use of a standardised tapping machine as an impact sound source, housed within a thoroughly insulated case. In a standardised tapping machine, five hammers of a defined mass are used for the generation of the impact sounds. The distribution of the hammers and their parameters, together with the parameters of the whole construction of the tapping machine, are described in detail in the ISO 10140-5 standard [8]. The falling hammers of the tapping machine generate not only impact sounds but also cause the propagation of airborne sounds. In order to eliminate the influence of the airborne sounds on the final measurement results, the tapping machine must be covered with an insulation case of adequate parameters, i.e. the airborne sound insulation of such a case must be efficient enough. The construction of an insulation case was precisely described in, for example, [3]. The authors proposed a multi-layered construction in which the walls of the insulation case are built from layers of plaster board, mineral wool and plywood; the connections between the floor and the case are additionally sealed with putty. Such a solution ensures the airborne sound insulation of around 35–50 dB across the whole frequency range of interest, which is sufficient for such a measurement. The proposed insulation case is shown in Fig. 2. Because of the use of a standardised tapping machine, the generated sounds are stable and do not change over time; as a consequence, the results are not dependent upon the specific sound-source device used, as long as it meets the requirements given by the standard.

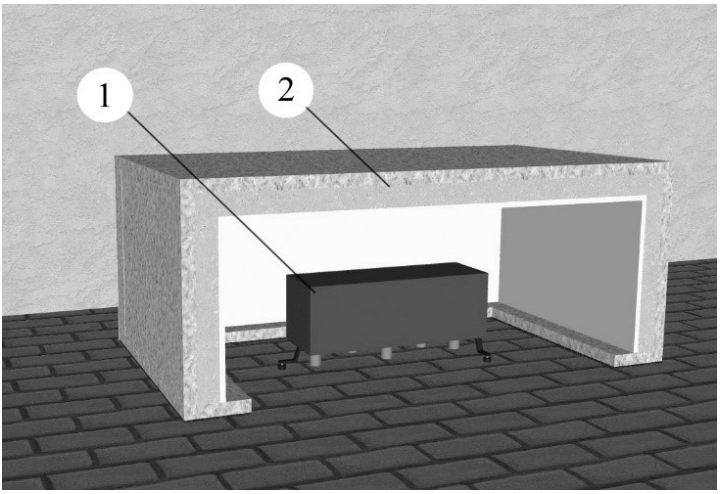

Fig. 2. A cross section through the insulation case (2) with a standardised tapping machine inside (1)

Having insulated the airborne sounds with the aforementioned insulation case, the vibrations of the ground can be measured in order to determine the intensity of the propagating structure-borne sounds. The comparison of the vibration acceleration levels on the surface of the construction elements under investigation, i.e. floors, walls and façades, enables the determination of the main propagation paths. The measurement of sound pressure level in turn enables the assessment of the impact sound levels. By correlating the spectra of the measured sound pressure levels and vibration signals, the most problematic frequencies can be determined; separate building elements can be investigated in terms of the frequencies within which the highest sound radiation can be observed.

3. The subject of investigation – Cracow Philharmonic building

In the following paper, the validity of the proposed engineering method to identify the transmission paths of structure-borne sound was examined. As an example site for the measurements, the Cracow Philharmonic building was chosen. In this concert hall, there has always been a major problem with structure-borne sounds mainly coming from two sources (Fig. 3). The first of these sources is the tram infrastructure (tram tracks run alongside two walls of the building – one of these is the external wall of the concert hall itself) and the second is the footsteps of pedestrians on the pavement along the external wall of the concert hall. It is crucial to determine which structure-borne sound transmission path is dominant; this knowledge is vital for the proper design of noise and vibration protection. In the following research, only one sound source was investigated – the footstep noise coming from the pavement on Zwierzyniecka Street, which is along the external wall of the concert hall. The tram noise was the topic of a separate analysis performed at AGH University of Science and Technology [10]. The main goal of the study presented in this paper is to

Fig. 3. View of the Cracow Philharmonic building together with the surrounding tram infrastructure and pavements [6]

determine the dominating sound transmission path. The proposed measurement method will also be verified in terms of its accuracy at identifying the precise transmission paths.

The standardised tapping machine, which imitates the real sound source (footsteps) was located along the external wall of the concert hall at a distance of 1.5 m from the wall and covered with the insulation case. The total area of the said wall is 327 m^2, including: brick wall – 270 m^2; window openings filled in with bricks – 47 m^2; wooden doors – 10 m^2. The total volume of the concert hall is 7045 m^3. The internal walls of the concert hall are made from brick, the floor is of a concrete construction and the ceiling is a suspended construction with plasterboard tiles. The measurements of the vibrations were performed on two sides of the external wall – inside and outside the building – at the same distance from the wall, and on the wall itself. The distribution of the measurement points is shown in Fig. 4 – four individual measurement points were inside the room and four individual measurement points were outside the room. The measurement points were distributed in a way which enabled obtaining

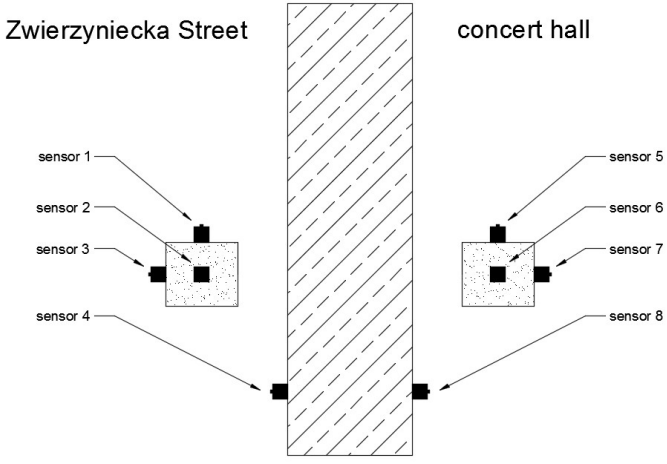

Fig. 4. Scheme of the placement of the vibration sensors [2]

information on the values and character of the vibrations of the floor on the three axes (the sensors were placed on the pavement and on the floor inside the concert hall) as well as on the wall in a perpendicular orientation. The sound pressure level of noise transmitted into the concert hall was measured at a distance of 1 m from the external wall.

The system used for the acceleration measurement consisted of a 3050-A-60 Brüel & Kjaer six-channel analyser together with six accelerometers (4500 A, Brüel & Kjaer) of the following parameters: sensitivity 1000 mV/g, measurement range 0.4 Hz – 6 kHz (± 10% amplitude), 2 Hz – 5 kHz (± 5˚ phase). The measurements were taken using a dedicated Pulse system. All the calculations and data analyses were performed in the MATLAB environment. For the measurement of sound pressure levels, a SVAN 912E sound level meter was used.

4. Analysis of the structure-borne sound transmission paths

As a result of the performed measurements, the authors obtained the spectra of the vibration acceleration recorded in all of the tested measurement points; the sound pressure level in the concert hall was also recorded. As the measurements indicate, the impact sound generated by the tapping machine propagates mainly in the vertical direction (the signal recorded by sensor 2 is characterised by the highest amplitude) although it also

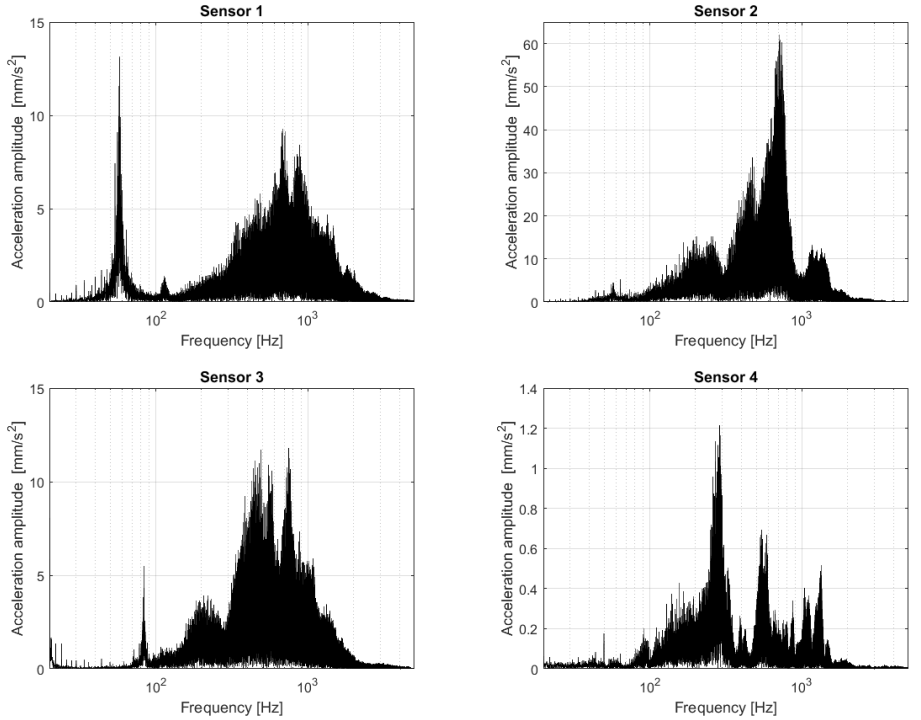

Fig. 5. The vibration spectra in the measurement points located outside the concert hall (each graph has a different scale on the y-axis)

propagates in the two horizontal directions (Fig. 5); however, the amplitudes of the signals recorded by sensors 1 and 3 are only around 21% and 19% of the maximum amplitude (as recorded in the vertical direction). Very little acoustic energy is transmitted through the wall – the amplitude of the signal recorded by sensor 4 is only 2% of what is recorded by sensor 2. The vibroacoustic background has no impact on the results – the amplitudes do not exceed 0.3 mm/s^2, which is negligible.

Analysing the acceleration spectra obtained in all the measurement points inside the concert hall (Fig. 6), it can be stated that the main structure-borne sound transmission path is through the floor, and the dominant direction of the vibrations is horizontal (sensors 5 and 7). In both cases, the prevailing frequency is about 360 Hz, which is also the dominant frequency in the spectrum of the noise measured inside the concert hall (Fig. 7). The amplitudes of vertical vibrations (sensor 6) and the vibrations of the wall on its inside (sensor 8) are not very significant – less than 30% of the maximum values recorded by sensors 5 and 7 – and they oscillate around the levels characteristic of background noise.

By means of the proposed engineering method to measure structure-borne sounds, it was possible to identify the main sound transmission path in the Cracow Philharmonic building from the impact source located on the pavement. As was indicated, this path is through

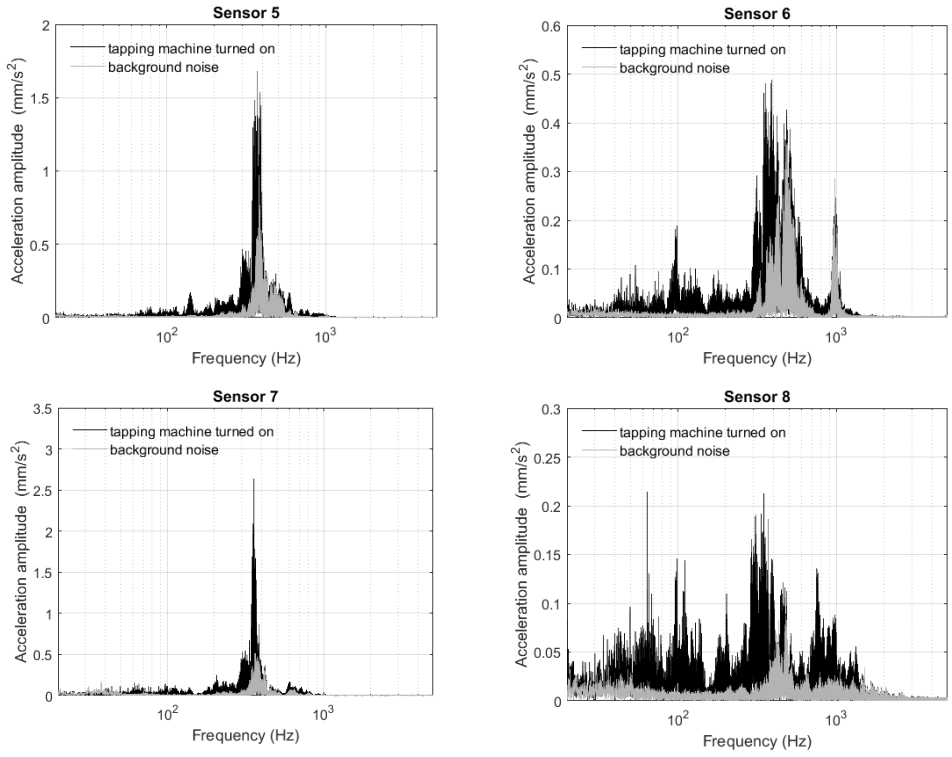

Fig. 6. The vibration spectra with background noise in the measurement points located inside (each graph has a different scale on the y-axis)

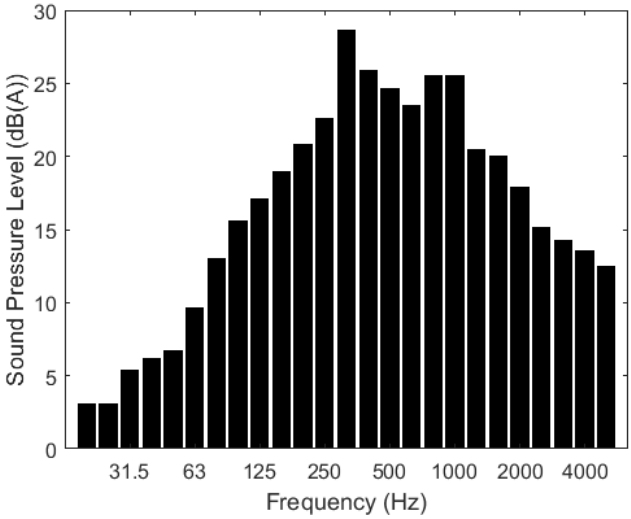

Fig. 7. Noise level inside the concert hall with tapping machine outside the concert hall turned on

the floor in the concert hall in the horizontal direction; the identification of the main sound transmission path enables the choice of proper vibroacoustic protection for the concert hall and as a consequence, will contribute to the reduction of the background noise inside the concert hall.

5. Summary and conclusions

In this paper, the authors' engineering method for the identification of the structure-borne sound transmission paths has been described and verified. The Cracow Philharmonics building was chosen as an example building to verify this method. The proposed method allowed the determination of the impact sound transmission paths from the external environment to the inside of the concert hall. In the research, the sound of footsteps from the adjacent pavement, imitated by a standardised tapping machine, was investigated. It was determined that the main structure-borne sound transmission path to the inside of the concert hall is through the concert hall floor in a horizontal direction. Knowing the main structure-borne sound transmission path will be crucial for the design of effective vibroacoustic protection.

References

[1] Asakura T., Toyoda M., Miyajima T., *Numerical and experimental investigation on structure-borne sound transmission in multilayered concrete structures*, Journal of Sound and Vibration 413, 2018, 1–25.

[2] Baruch K., Szeląg A., Majchrzak A., Kamisiński T., *Engineering method to measure structure borne sounds transmitted through the building partition*, 8th International Conference on Environmental Effects on Buildings and People: actions, influences, interactions, discomfort, 2018, 101–102.

[3] Baruch K., Szeląg A., Rubacha J., Hałoń K., *An engineering method to measure the impact sound reduction due to soft coverings on heavyweight floors*, Applied Acoustics 142, 2018, 18-28.

[4] Cremer L., Heckl M., *Structure-borne sound. Structural Vibrations and Sound Radiation at Audio Frequencies*, Springer-Verlag, Berlin 1988.

[5] Elliott A., Moorhouse A., Huntley T., Tate S., *In-situ source path contribution analysis of structure borne road noise*, Journal of Sound and Vibration 332.24, 2013, 6276–6295.

[6] Google Maps, https://goo.gl/maps/GESQd7VnvJH2 (access: 29/10/2018).

[7] Hassan O., *Building Acoustics and Vibration. Theory and Practice*, World Scientific, Singapore, 2009.

[8] ISO 10140-5:2010, Acoustics-Laboratory measurement of sound insulation of building elements-Part 5: Requirements for test facilities and equipment. International Organization for Standardization.

[9] ISO 140-4:1998, Acoustics–Measurement of sound insulation in buildings and of building elements. Part I: Requirements for laboratory test facilities with suppressed flanking transmission.

[10] Kamisiński T., Flach A., Pilch A., Rubacha J., Baruch K., Brawata K., Zastawnik M., *Pomiar hałasu i badania izolacyjności akustycznej przegród budowlanych w budynku Filharmonii im. K. Szymanowskiego w Krakowie* (Raport), Kraków 2015.

[11] Nelson J., Hugh J., *A prediction procedure for rail transportation groundborne noise and vibration*, Transportation Research Record 1143, 1987, 26–35.

[12] Ngai K., Ng C., *Structure-borne noise and vibration of concrete box structure and rail viaduct*, Journal of Sound and Vibration 255.2, 2002, 281–297.

[13] Plunt J., *Finding and fixing vehicle NVH problems with transfer path analysis,* Sound and vibration 39.11, 2005, 12–17.

[14] Szeląg A., Stypuła K., Kamisiński T., *Sound Radiation by Vibrating Building Partitions in Terms of Acceptable Vibration Values*, Acta Physica Polonica A 125, 2014, 122–126.

TECHNICAL TRANSACTIONS 7/2019
CIVIL ENGINEERING
DOI: 10.4467/2353737XCT.19.070.10721
SUBMISSION OF THE FINAL VERSION: 3/06/2019

Janusz Bohatkiewicz orcid.org/0000-0002-9659-2666
j.bohatkiewicz@pollub.pl
Michał Jukowski orcid.org/0000-0003-3750-8281
Marcin Dębiński orcid.org/0000-0002-5967-0637
Department of Roads and Bridges, Lublin University of Technology
Maciej Hałucha
EKKOM Sp. z o.o., Poland

Study of noise originating from selected bridge expansion joints

Badania hałasu pochodzącego od wybranych dylatacji mostowych

Abstract

Road noise constitutes one of the most adverse impacts of road traffic on the environment. Noise that is particularly annoying for local inhabitants is recorded in the vicinity of engineering structures where various types of expansion joints are used [1–3]. There are currently many road connections being built in Poland, including a total of almost ten thousand expansion joints. The authors of this article attempt to determine the noise differences of several of the most commonly used expansion joints – single-, double-, and multi-module, block and finger expansion joint described as one of the most advantageous from the acoustic point of view. This study also attempts to determine the im-pact of expansion joint types on the noise level in comparison to the road section not equipped with these devices, which was adopted as the base noise level.
Keywords: impulse noise, bridge expansion joints, equivalent sound level

Streszczenie

Jednym z najbardziej niekorzystnych oddziaływań ruchu drogowego na otoczenie jest hałas drogowy. Szczególnie dokuczliwy dla mieszkańców hałas notowany jest w pobliżu obiektów inżynierskich, gdzie stosowane są różnego rodzaju dylatacje [1–3]. Obecnie w Polsce wybudowano wiele połączeń drogowych, w ciągu których znajduje się prawie dziesięć tysięcy urządzeń dylatacyjnych. Autorzy artykułu podjęli próbę określenia różnic hałaśliwości dla kilku najczęściej stosowanych dylatacji – szczelnej jedno-, dwu- i wielomodułowej, blokowej oraz określanej jako jednej z najkorzystniejszej z punktu widzenia akustycznego – dylatacji palczastej. W badaniach podjęto również próbę określenia wpływu typów dylatacji na poziom hałasu w porównaniu z odcinkiem drogi niewyposażonym w te urządzenia, który został przyjęty jako bazowy poziom hałasu.
Słowa kluczowe: hałas impulsowy, dylatacje mostowe, równoważny poziom dźwięku

1. Introduction

Poland is one of the countries which, following its accession to the European Union, has observed the dynamic development of the road infrastructure, resulting in the construction of many kilometers of highways, expressways, and related technical and engineering sites. In the vast majority of cases, the connection of the road to a bridge or viaduct is made using a so-called expansion joint gap, enabling the free movement of spans resulting from, for example, differences in air temperatures, which may cause expansion or contraction of the material from which the load-bearing structure is made. From an acoustic point of view, it is the contact between the road and the engineering object that is the most significant place where the so-called impulsive noise phenomenon occurs; it is this noise which is frequently the subject of social disputes [2]. In Poland, the most frequently used types of expansion joints are: tight modular, open finger, bituminous, block, open covered with sheet metal, in the form of a dilatated structure of a platform with continuous surface, the absence of expansion joints in the case of short engineering structures. The type of expansion joint used is determined by the width of coverage, the possibility of longitudinal movements of the span and the sinking of supports, e.g. in areas of underground deposit exploitation, therefore, it is not always possible to choose a specific type of expansion joint. According to the authors' own observations, modular expansion joints seem to be the most frequently used type of expansion joints on engineering structures.

2. Impulse noise phenomenon

The acoustic phenomenon caused by the passage of vehicles over bridge structure expansion joints demonstrates the character of impulse sound. This is not a typical impulse sound, which according to the definition [4–10, 12] means one or more acoustic events of short duration (less than 1 sec) that are of high sound-pressure levels. Noise of this type occurs mainly in the working environment. In the case of the acoustic impact of expansion joints used in bridge structures, the resulting acoustic phenomenon has a slightly different character. Differences in noise amplitudes as they are in the case of other impulse sounds are not as great and the phenomenon itself, although characterised by a short duration, very often causes the excitation of material sound in the structure of the object (especially when using steel elements) of a slightly longer duration. However, sound of this character is very burdensome for people in the affected area. Although it does not exceed the acceptable noise levels in the environment, it may cause significant discomfort and stress and may disturb the sleep of nearby residents' or 'may trigger the onset of sleep disorders for local residents [3].

With regard to impulse noise in industrial scenarios, the most important indicator used in the assessment of workers' exposure to impulse noise is the peak sound pressure level or peak 'C' weighted sound level [7]. When measuring and evaluating road noise with regard to impulse noise from expansion devices, an indicator of the equivalent sound level with 'A' weighting is generally applied, which is then used to compare it with the admissible values.

Usually, although it is not precisely defined in legal regulations in Poland, appropriate correction coefficients are added to the measurement results to account for the share of impulse sound. These are coefficients that increase the results of measurements, so that the impact assessment is more reflects the opinions of residents and the discomfort to which they are exposed. This was confirmed by, among other things, a questionnaire survey performed as part of study [16], the results of which were not discussed in more detail in that article.

3. Purpose and location of measurements ground

The aim of the study was a comparative analysis of different expansion joint types used in engineering structures with regard to road noise, as well as an attempt to identify noise arising at the interface of the vehicle wheel with the bridge expansion joint. This issue is very important from an acoustic and environmental standpoint because when a car drives on the expansion joint, the impulse noise is created, which should be considered and interpreted in a different manner to road noise.

The scope of analyses included the selection of study sections and the performance of equivalent sound level and noise tests of engineering-structure expansion joints.

The results of the *in situ* study of four bridge structures located in Puławy and Dęblin in the Lubelskie Voivodeship and Knurów in the Śląskie Voivodeship are presented below. As part of the analyses, noise tests, speed measurements of vehicles passing through the expansion joint cross section and measurements of traffic intensity along with the division of the bridges into their generic structures were performed. Such an approach made it possible to verify the level of noise generated by various types of vehicles passing through the gap and also made it possible to attempt to categorise (evaluate) the surveyed bridge expansion joints in terms of their noise levels.

In order to determine the noise level generated during vehicle passage over the object (expansion joint), measurements of traffic parameters and noise on selected test areas were made. Five types of expansion joints were measured: one multi-module expansion joint, two

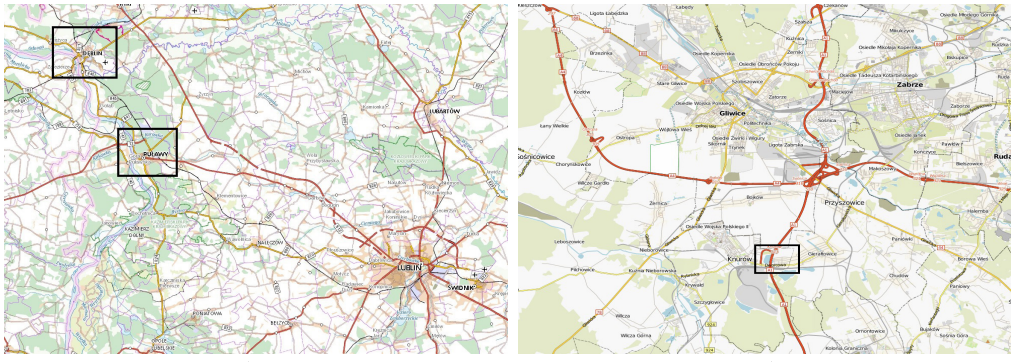

a) b)

Fig. 1. Location of measurement grounds a) Lubelskie Voivodeship, b) Śląskie Voivodeship

single-module expansion joints, one double-module expansion joint, one finger expansion joint, and one block expansion joint. Four test areas were selected, the first was located along the DK12 national road in Puławy, the second along Marszałka Piłsudskiego Street in Puławy, the third along 15 Pułku Piechoty Street in Dęblin, and the fourth along the A1 Highway in Knurów. Figures 1a and 1b present the detailed location of the testing grounds.

With regard to the standard approach concerning road noise, there is no detailed information available on testing and admissible values for the phenomenon of road impulse noise. The admissible values for traffic noise in the environment were presented in the Regulation of the Minister of Environment from 1st October 2012, Dz.U. Journal of Laws, item 1109. It contains a table listing the admissible levels of environmental noise caused by each group of noise sources. For roads and railways, these values depend on the type of terrain and range from 65 dB for daytime to 56 dB for night time. They do not include the sound pressure level of impulse sources. The impulse correction to the results of impulse parameter measurements can be found in the Regulation of the Minister of the Environment of 30th October 2014, Dz.U. Journal of Laws, item 1542, Appendix no. 8. For the measurement of the equivalent sound level, this correction depends on the type of sound, i.e. whether the sound is highly impulsive, whether the impulse sound has high energy or whether it is a typical impulse sound. These values range from 3 dB to 12 dB, demonstrating that this correction has a significant impact on the final value of the measurement, taking into account the value of the equivalent sound level given in the Dz.U. item 1109.

4. *In situ* measurement and results

After a detailed analysis of the tested sections, ten measurement points, marked PPH-(1-10), were selected:

- PPH-1, PPH-2 – Knurów Highway A1,
- PPH-3, PPH-4 and PPH-5 – DK 12 Puławy-Zwoleń,
- PPH-6, PPH-7 and PPH-8 – Marszałka Piłsudskiego Street in Puławy,
- PPH-9 and PPH-10 – 15 Pułku Piechoty Street in Dęblin.

An example of the measurement point location is shown in Fig. 2.

Fig. 2. Location of measurement points PPH-(3-8)

4.1. Methodology of measurement – Puławy and Dęblin

In order to perform noise tests on bridge expansion joints, a study program was first developed which included information on the method of their execution, a list of the measurement equipment used and the organisation of the measurement area [11]. At each measurement point, it was assumed that the microphone of the sound level meter would be mounted 30 cm above the surface of the expansion joint along its axis, on the edge of the road (Fig. 3a). In addition, one measurement point, called the 'base point', was added in each test (Fig. 3b). The base point was located between two expansion joints, at their mid-span. This approach allowed comparison of the sound level from the same source, i.e. a vehicle moving at the same speed, in the same cross section, but without an expansion joint. Over the course of the study, the speeds of passing vehicles were measured, as well as their intensity, along with vehicle classification. In this way, it was possible to read out the noise generated by a single passing vehicle and to perform a comparative analysis of the expansion joint. All surveys were preceded by a field observation and pilot measurements. The measurement equipment which was used for the duration of the study consisted of class 1 sound level meters with the necessary accessories. All meters had the same measurement parameters, i.e. measurement in 1/3 octave bands, FAST constant and correction filter A.

Fig. 3. a) Microphone location above the dilatation b) Microphone location at the base point

An example of how the microphones are arranged relative to each other is shown in Fig. 4. The distance between the base points and the dilatation fluctuated within the range of 30 m.

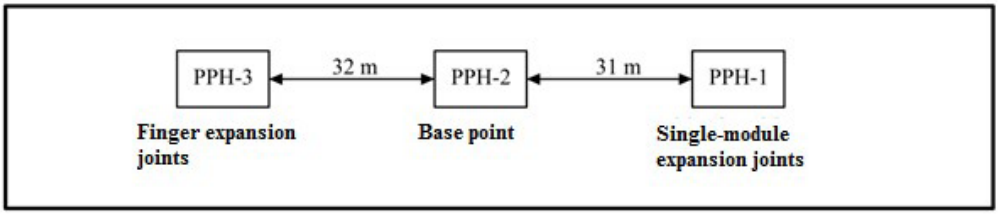

Fig. 4. Scheme of distribution of measurement points on a bridge along the DK12 route Puławy–Zwoleń

4.2. Measurement methodology – Knurów

Noise measurements from the impact of expansion joints used in the WA-470 site on the A1 highway in the town of Knurów were conducted twice: in 2013 [9] and 2018 [13]. In order to perform this, the method of direct measurements within a period of 24 hours was used in accordance with the procedure described in the regulation presented in [15]. These were taken at six points located in the vicinity of the A1 highway in the area immediately adjacent to the bridge structure. The location of the measurement points is shown below in Figs. 5 and 6.

Meteorological conditions were observed and the traffic intensity and speed of vehicles driving on the highway were measured while simultaneously measuring the sound level. Sound level measurements were performed with class 1 precision sound meters, FAST time constant and 'A' weighted characteristics. In 2013, at two points (PDH-2 and PDH-4), the sound level was additionally measured using 1/3 octave filters in order to determine the frequency characteristics of the noise source (identification of the frequency range for sound generated by cars passing over expansion joints used in the site). In 2013, noise measurements at PDH-6, PDH-7 and PDH-8 points were taken within a duration of 30 minutes to obtain data for calibration of the calculation model with which the acoustic modelling was subsequently performed. The results of these measurements are presented in detail in publication [16], and they were not described in more detail as a part of this article.

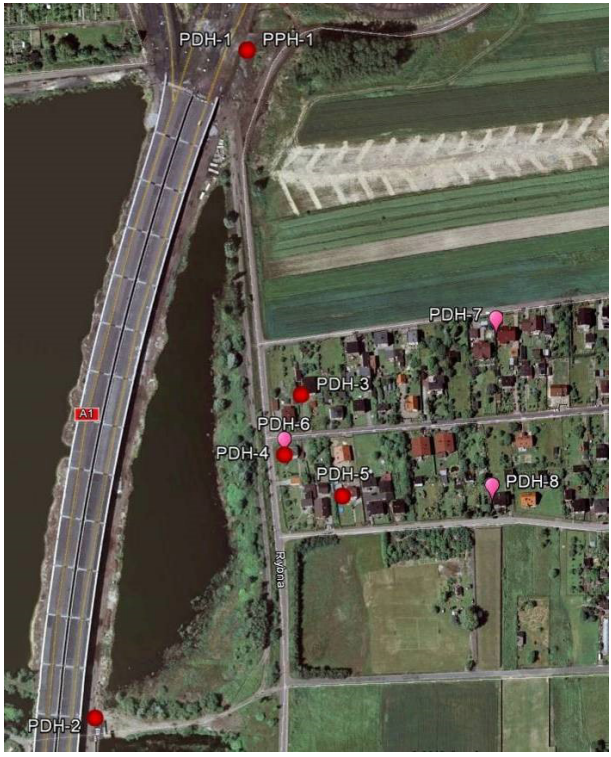

Fig. 5. Location of measurement points in the vicinity of the WA-470 site in Knurów in 2013

Fig. 6. Location of measurement points in the vicinity of the WA-470 site in Knurów in 2018

Additionally, in order to check whether the level of noise generated during vehicle movement over the expansion joints is the same for each expansion joint, measurements of noise directly at the wheel of a car moving over the structure were taken in 2013. The measured values of the noise level allowed determining the differences in the noise emission generated during the operation of specific expansion joints.

4.3. Description of performed tests

The study was performed using two approaches which differed in their methods of execution. The first approach concerned measurements in Puławy and Dęblin, the second approach was applied in Knurów on the A1 highway. During the measurement of the sound level (equivalent sound level L_{Aeq}), the speed of the moving vehicle was tested simultaneously with the division into light and heavy vehicles, and the intensity of the moving vehicles was measured, with the division into vehicle type, comprising motorcycles, passenger vehicles, vans, rigid lorries, articulated lorries and buses. The measurements were performed at 15-minute intervals. For each interval, individual groups of vehicles were counted, categorising them into light vehicles and heavy vehicles. Heavy vehicles included rigid lorries, articulated lorries, buses and motorcycles. On this basis, it was possible to calculate the percentage share of heavy vehicles in the traffic flow. Similarly, the speed of moving vehicles was also

measured with their division into light vehicles and heavy vehicles. The results obtained for the individual testing sites are described below.

- John Paul II Bridge in Puławy along the national road DK12

Measurements of traffic intensity revealed that passenger vehicles comprised the largest share of vehicle traffic. The share of heavy-duty vehicles was 34.2%. A total of 401 vehicles passed during the 60-minute evaluation. No tractors or bicycles were recorded driving through the site. The average speed of the light vehicles was 76.2 km/h and for heavy vehicles, it was 74.2 km/h. The value of the equivalent sound level for a 15-minute interval was read from each gauge. Figure 7 shows the diagram of traffic intensity in individual time intervals, along with the corresponding value of the equivalent sound level for the single-module expansion joint, the finger joint and the baseline.

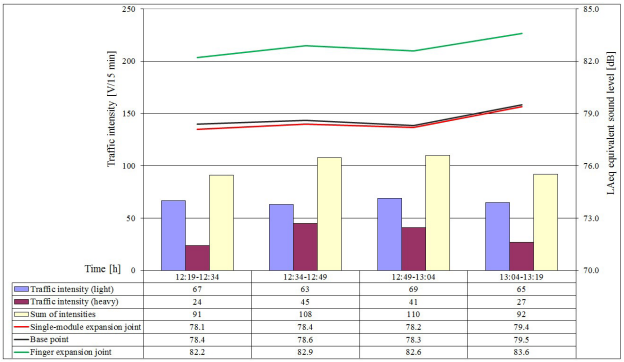

Time [h]	12:19-12:34	12:34-12:49	12:49-13:04	13:04-13:19
Traffic intensity (light)	67	63	69	65
Traffic intensity (heavy)	24	45	41	27
Sum of intensities	91	108	110	92
Single-module expansion joint	78.1	78.4	78.2	79.4
Base point	78.4	78.6	78.3	79.5
Finger expansion joint	82.2	82.9	82.6	83.6

Fig. 7. Diagram of traffic intensity together with sound level L_{Aeq} in specific time intervals on the John Paul II bridge as a part of the DK12 route: Puławy–Zwoleń

The John Paul II Bridge was a very important test ground in terms of expansion joint types that were used on the bridge and on the overpass in front of the bridge. Testing at this location made it possible to measure the intensity of sound from the same stream of traffic, moving at the same speeds, passing through two types of expansion joints. Analysing the results presented in Fig. 7, it could be concluded that a single-module expansion joint is quieter than the baseline, which is considered as a reference point. This situation results from the fact that at the measuring point located at the single-module expansion joint, there was an acceleration lane, where vehicles were driving at a distance of 3.5 m further from the meter's microphone than for other measuring points. This had a significant impact on the obtained results.

As previously mentioned in this publication, noise from expansion joints are of an impulse nature. A single pulse of a sound level significantly higher than the average value of the equivalent sound level for the considered time interval (15 minutes) does not significantly increase the average noise level, as interpreted in accordance with the applicable regulations. The authors of the article attempted to identify a frequency band in which impulse noise coming from expansion joint has a higher energy than the reference level – which is the noise generated from the surface of the road rather than from the joint. The aim of this approach

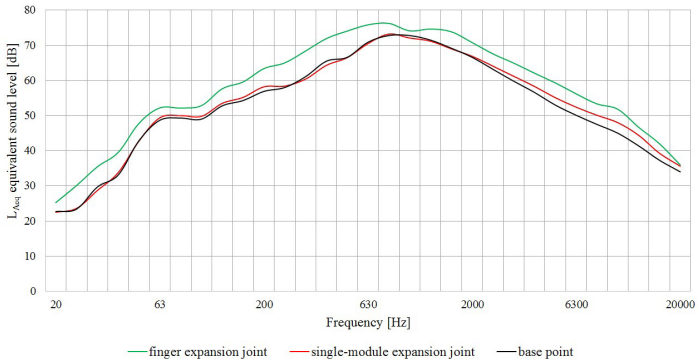

Fig. 8. Comparative analysis of noisiness of finger and single-module expansion joint in the full frequency band compared to the baseline for the study period of 30–45 minutes – John Paul II Bridge in Puławy

was to determine whether the analysed sound level is in the band that could be perceived by the human ear. For this purpose, diagrams were created for each 15-minute measurement, showing the equivalent sound level versus the frequency value, presenting both the expansion joint types, and the baseline (reference level). A sample graph is shown in Fig. 8.

When interpreting the results, one should take note of the expansion joint width as this is a very important parameter. In the case of the finger joint, it was around 75 cm, and for a single-module joint, it was around 7 cm.

- Bridge on Marszałka Piłsudskiego Street in Puławy

In the case of the bridge on Marszałka Piłsudskiego Street, the traffic situation differed significantly in comparison to the John Paul II Bridge. More than 97.1% of vehicles passing through the analysed section of the road were passenger vehicles. During the 60-minute test, a total of 621 vehicles passed; this equated to more than 50% more than on the DK12 national road. This is the result of the structure's location – the entrance to the city centre. As was the case with the John Paul II Bridge, no tractors were recorded passing here. The average speeds

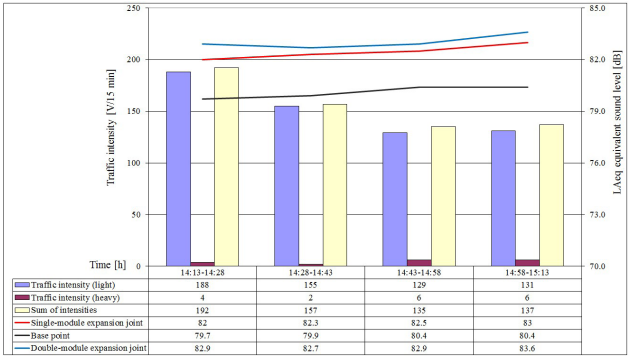

Fig. 9. Diagram of traffic intensity together with sound level L_{Aeq} in specific time intervals on the bridge on Marszałka Piłsudskiego Street in Puławy

of light vehicles were around 48.8 km/h and for heavy vehicles, around 39 km/h. Figure 9 (below) shows traffic intensity during individual time intervals, along with the corresponding value of the equivalent sound level for the single-module expansion joint, the double-module expansion joint, and the baseline.

In this case, analyses were performed across the full frequency band in order to determine the characteristic frequency band for the impulse noise. An example graph for the analysed situation is presented in Fig. 10.

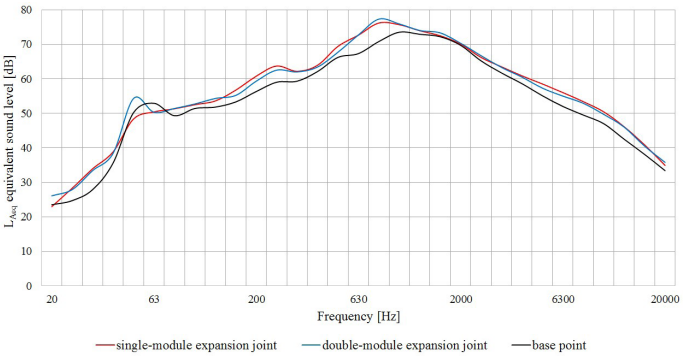

Fig. 10. Comparative analysis of noise of the double-module and single-module expansion joint across the full frequency band compared to the baseline for the study period of 15–30 min – bridge on Marszałka Piłsudskiego Street

The width of the double-module expansion joint was around 12 cm and the width of the single-module expansion joint was around 7 cm.

- Bridge at 15 Pułku Piechoty Street in Dęblin

In the analysed case, the block expansion joint was subjected to noise tests. In the cross section of national road No. 48, passenger vehicles had the largest share of vehicle traffic. Heavy vehicles accounted for only 2.1% of all road vehicles moving on this road. A total of 290 vehicles passed over the analysed section during the 30-minute period of observation.

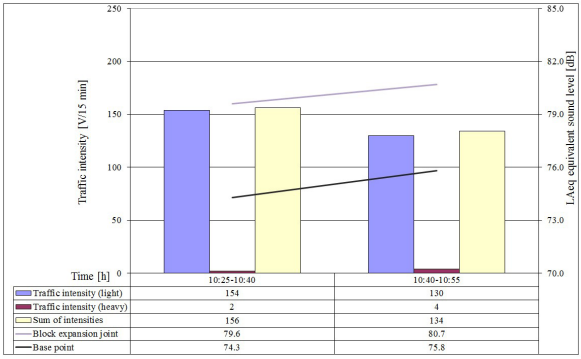

Fig. 11. Diagram of traffic intensity together with sound level L_{Aeq} in specific time intervals on the bridge at 15 Pułku Piechoty Street in Dęblin

No tractors or bicycles were recorded during this period. The average speed of light vehicles was 58 km/h and for heavy vehicles, it was 57 km/h. Figure 11 below shows a graph of traffic intensities in relation to the values of equivalent sound levels for the different time intervals. The width of the block expansion joint was 20 cm.

Figure 12 below presents a comparative analysis of block expansion joint noise in relation to the baseline across the full frequency band for the study period of 0–15 min.

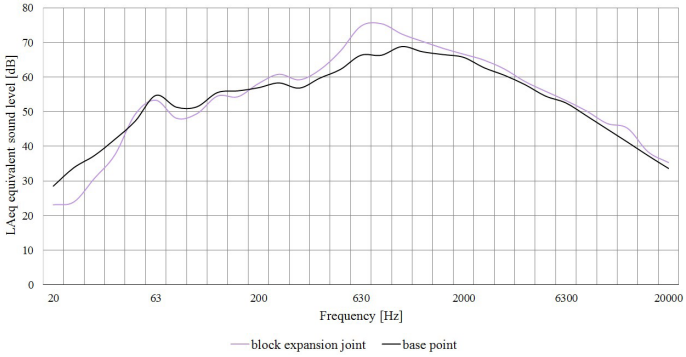

Fig. 12. Comparative analysis of block expansion joint noise compared to baseline across the full frequency band for the study period of 0–15 min – bridge at 15 Pułku Piechoty Street in Dęblin

- Bridge on the A1 highway – Knurów

24-hour noise measurements in the vicinity of the WA-470 site on the A1 highway were performed in 2013 [16] at 6 points. Due to the duration of measurements (24 hours) and the measurement method (direct method) in accordance with the regulation in [15], it was possible to refer directly to the levels of permissible environmental noise [14], which was the main objective of this study. The regulations also characterise the acoustic climate prevailing in the areas adjacent to the analysed site. Table 1 below shows the measurement results.

Table 1. Results of the 24-hour sound level measurements taken in 2013 [16]

Measurement point no.	Sound level (A)	
	Daytime	Night time
PPH-1	74.0	68.6
PDH-1	70.1	65.1
PDH-2	65.8	61.1
PDH-3	60.2	55.5
PDH-4	61.2	56.6
PDH-5	57.8	54.0

Measurements of noise directly at the wheel of a car moving on a highway structure enabled determining the differences in noise emission generated during the operation of particular expansion joints. The obtained average results for individual expansion joints ranged from

106.6 dB to 108.4 dB. It can therefore be concluded that each of the expansion joints had a similar acoustic effect. Additionally, as part of study [16], noise measurements were taken at 1/3 octave frequency divisions. The results of these measurements are presented below in Fig. 13.

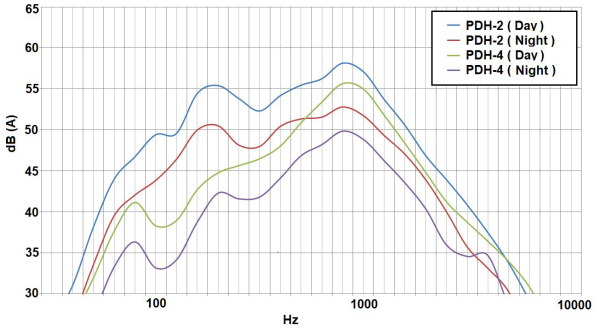

Fig. 13. Summary of frequency characteristics in 1/3 octave centre bands at PDH-2 and PDH-4 sites divided into daytime and night time [16]

In 2018, noise measurements were taken at nine points located in the vicinity of the WA-470 overpass in Knurów [11]. Each of these were measured during four consecutive periods of the day. This allowed additional observation of the noise level variability. These results are presented in Table 2 below.

Table 2. Results of 24-hour sound level measurements taken in 2018 [13]

Measurement point no.	**Sound level (A)**	
	Daytime	Night time
PPH-1	73.9	68.8
	74.3	69.3
	74.0	68.5
	74.5	69.0
PPH-2	69.5	63.7
	69.1	64.5
	69.9	64.3
	70.0	64.7
PDH-1	62.5	55.9
	56.7	54.5
	55.0	52.4
	57.9	53.8

PDH-2	62.5	56.0
	60.0	57.2
	59.9	56.7
	60.2	57.8
PDH-3	62.6	55.8
	60.2	57.0
	59.6	56.1
	59.8	57.2
PDH-4	63.3	56.0
	60.8	56.4
	64.4	59.3
	61.7	58.9
PDH-5	60.0	56.1
	54.7	53.7
	50.4	49.4
	55.3	52.8
PDH-6	59.3	55.6
	52.2	51.0
	49.4	44.2
	54.1	51.2
PDH-7	59.6	50.7
	56.2	54.7
	61.1	56.7
	59.6	57.8

Acoustic modelling was also performed as a part of both studies [13, 16]. The French calculation method 'NMPB-Routes – 96 (SETRA-CERTU-LCPC-CSTB)' was used in noise analysis, as described in 'Arrêté du 5 mai 1995 relatif au bruit des infrastructures routières, Journal Officiel du 10 mai 1995, art. 6' and the French standard 'XPS 31-133'. The view of the geometric part of the calculation model is shown below in Fig. 14. It should be emphasised that in both cases, the noise from car movement over the expansion joint devices was additionally modelled, as presented in Fig. 15. Due to the fact that typical acoustic models do not allow direct representation of this type of noise, in both cases linear sources of industrial noise were used as these best reflected the acoustic impact originating from the expansion joint. The results of the acoustic calculations are presented in Fig. 16 (2013 [16]) and Fig. 17 (2018 [13]).

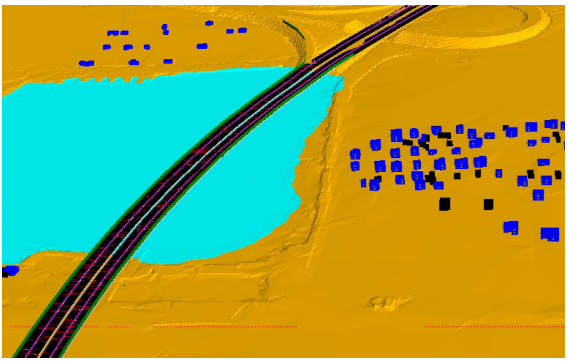

Fig. 14. View of the calculation model (terrain) used in the studies [13, 16]

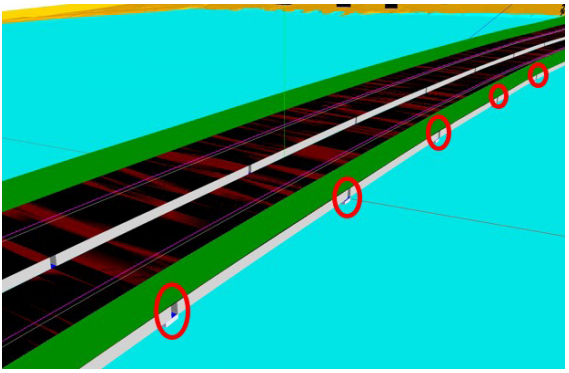

Fig. 15. View of the reflection in the calculation model concerning the acoustic impact of marked expansion joints [13, 16]

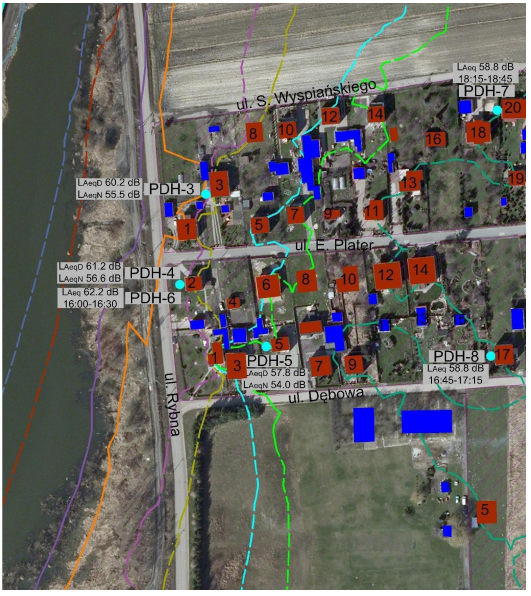

Fig. 16. Results of acoustic calculations performed in 2013 [16]

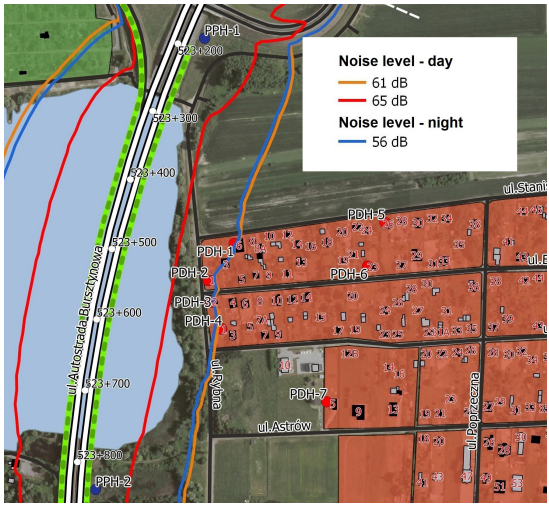

Fig. 17. Results of acoustic calculations performed in 2018 [13]

Specific analysis of measurement and acoustic calculation results is presented in section 5 of the article.

5. Discussion and conclusions

When analysing the results of the expansion joint tests, it is concluded that in each case it is possible to observe a significant difference in relation to the base point in the level of noise generated by the expansion joint in the frequency band of 500–1250 Hz. Noise generated when passing through the expansion joint increases the sound level in this band, which falls within the range of the audible band for humans and can result in a negative impact on humans and the environment. Examples of results indicating this effect are shown in Fig. 18.

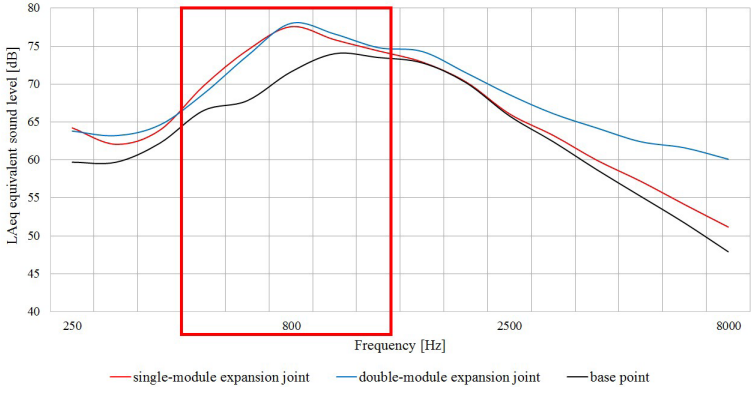

Fig. 18. Analysis in frequency bands for single and double-module expansion joint with reference to the baseline on the bridge on Marszałka Piłsudskiego Street in Puławy

Differences in sound levels are summarised in Fig. 19, in reference to the measured values of the equivalent sound level depending on the baselines for each analysed case. The list does not include point PPH-3 located on the single-module expansion joint on the John Paul II Bridge in Puławy because the measured values of the equivalent sound level are lower due to the greater distance from the noise source than other points.

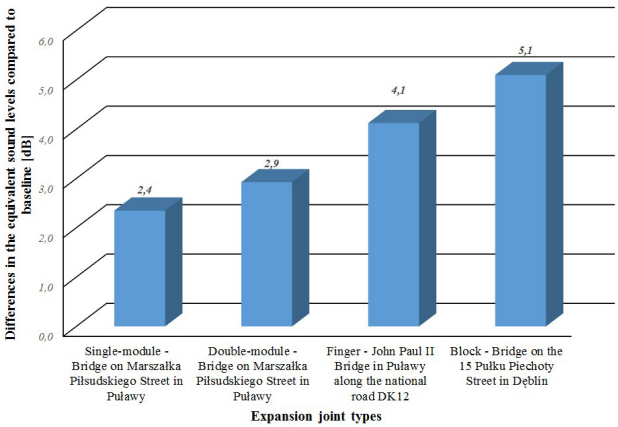

Fig. 19. Differences in the equivalent sound levels for each analysed expansion joint compared to corresponding baselines

Based on the above diagram, it can be concluded that the single-module and double-module expansion joints are the quietest. However, when analysing the obtained values of sound generated when passing over the expansion joint, one should also take note of the technical condition of the expansion joint and its width. Both parameters significantly influence the obtained results. The width of a finger joint is more than 6 times the width of a double-module joint and the sound level difference is only 1.2 dB; therefore, it can be concluded that a finger joint has good acoustic parameters. Nevertheless, based on the performed test, it can be concluded that the block expansion joint is the loudest.

In the area adjacent to the WA-470 site on the A1 highway, the dominant acoustic impact is the noise originating from the passage of vehicles over the expansion joint devices. The nature of this interaction has the characteristics of impulse sound (short duration, high amplitude of noise level), although it is not a typical impulse sound. Because of this, it is much more burdensome for the inhabitants of this area than the typical road noise which is additionally reduced by the noise barriers used on the bridge structure.

It should be noted that the noise levels measured in both 2013 and 2018 are slightly above the limit values at night, mainly at points closer to the analysed overpass. During the daytime, however, there are no instances of exceeding environmental noise limits. The results of measurements performed at the so-called reference points were not compared with the environmental noise limit values due to the fact that they were located in areas not subject to acoustic protection. They were used primarily to observe the parameters of the noise source and to calibrate the calculation model.

When analysing the results of noise measurements, it is necessary to take into account the nature of the acoustic impact that occurs in the studied area and the degree to which it constitutes a nuisance for the residents. Although environmental noise levels are exceeded by small values (less than 3.5 dB) compared to other areas located in the vicinity of main roads in Poland, the nuisance to residents resulting from the impact of vehicle traffic is high. This is due to the participation of impulse sounds originating from expansion joint devices that are additionally amplified by the steel structure of the building and its location above the strong sound-reflecting plane (water surface). Impulse sound, due to its short duration, does not cause a significant increase in the average value of the equivalent sound level, yet is very burdensome for residents, especially at night, under favourable conditions of acoustic propagation. It also certainly causes sleep disruption to people living in the closest vicinity of the highway [3].

When analysing the results of acoustic calculations presented in Figs. 16 and 17, the conclusions drawn from the analysis of noise measurement results should be confirmed. Buildings located closest to the bridge structure are within the range of noise impact that is slightly greater than acceptable. Nevertheless, the residents feel that it is very troublesome, which, as mentioned above, is related to the impulse nature of the sound generated by expansion joint devices. This is confirmed by the results of a survey conducted with residents.

Residents' responses to only one of several questions are presented within this article. This question is: "Is the noise from the overpass on the A1 highway a nuisance?".

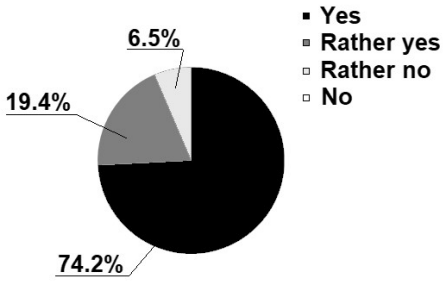

Fig. 20. Summary of residents' answers to the question: "Is the noise from the overpass on the A1 highway a nuisance?"

Residents' responses to the above question confirmed the conclusion formulated on the basis of measurement and calculation results. The majority of residents answered 'yes' and answers 'no' and 'depends on the situation' did not appear at all.

On the analysed WA-470 bridge, a part of the A1 highway, acoustic screens were used to protect residential buildings against the 'typical' impact of noise from vehicle traffic. It should be stressed, however, that the main cause of acoustic nuisance in the studied area is not this type of noise, but noise of an impulse nature, generated by the movement of cars over expansion joint devices, which are not shielded in any way. The effectiveness of the applied acoustic screens is evidenced by the fact that, despite a significant increase in traffic over the last few years, the noise level did not increase significantly. This can be observed by

comparing the results of traffic volume measurements and acoustic calculations performed in 2013 and 2018 [13, 16]. Over the last 5 years, the intensity of vehicle traffic has increased by almost 25,000 vehicles per day, and the state of the acoustic climate in the areas adjacent to the analysed overpass did not deteriorate significantly. This can particularly be seen in the comparison of noise measurement results at a point which was located in the same place in 2013 (No. PDH-4) and in 2018 (No. PDH-3). In 2013, a value of 61.2 dB was measured during the daytime and 56.6 dB was measured at night. In 2018, a value of 60.9 dB was measured at daytime and 56.7 dB was measured at night. The remaining measurement results cannot be directly compared because the measuring points were located in different places.

The lack of deterioration of the acoustic condition results from the fact that the acoustic screens used to effectively protect residential areas against the impact of 'typical' road noise and the increase in traffic volume did not have a significant effect upon the acoustic conditions prevailing in the analysed area. However, both in 2013 and 2018, there was significant nuisance present associated with expansion joints which are not protected in any way by the applied acoustic screens, as mentioned above. It is therefore necessary to take measures to mitigate this impact.

In order to achieve mitigation of the impact of expansion joints many types of actions have been considered that may reduce noise that they generate. Such actions may also include the replacement of expansion joint devices, but these are very expensive, and the effect that can be achieved may not provide the expected noise reduction; another option is the use of acoustic screens (which has not been described in detail in this article). The focus, however, is on reducing the noise spread from underneath the structure as this is the most disturbing for the residents. Insulating casing used on the bottom of the structure underneath the expansion joints was suggested in order to achieve this reduction. Acoustic calculations have also been performed which demonstrate the effect of noise reduction after using these casings. It has been concluded that the application of this type of protection will result in the reduction of the equivalent sound level compared to the current state. Due to the fact that these calculations were only performed on the basis of casing manufacturers' catalogue data and did not result from "*in situ*" tests, their results are burdened with a high degree of uncertainty. Because of this, they are not presented in this article.

The tests were performed as part of the RID I/76 'Protection against road noise' research project.

References

[1] Batko W., Przysucha B., *Statistical Analysis of the Equivalent Noise Level*, Archives of Acoustic 2014, Vol. 39, No. 2, 195–198.

[2] Beczek P., Maciejczyk J., Rymsza B., *Pomiar poziomu hałasu generowanego przez urządzenia dylatacyjne*, Materiały Budowlane 2013, No. 8, 34–36.

[3] Bohatkiewicz J., *Modelowanie i ocena rozwiązań chroniących przed hałasem drogowym*, Politechnika Lubelska Wydział Budownictwa i Architektury, Lublin 2017.

[4] Ancich E.J., Brown S.C., *Engineering methods of noise control for modular bridge expansion joints*, Acoustics Australia Vol. 32 December, 2004, No. 3.
[5] Foglar M., Goringer J., *Influence of the structural arrangement of bridges on the noise induced by traffic.* Engineering Structures 56, 2013, 642–655.
[6] Matsumoto Y., Yamaguchi H., Tomida N., Kato T., Uno S., Hiromoto Y., et al., *Experimental investigation of noise generated by modular expansion joint and its control*, Journal of the Japan Society of Civil Engineers Division A 2007, 63(1).
[7] Młyński R., *Hałas impulsowy. Stosowanie ochronników słuchu, Centralny Instytut Ochrony Pracy – Państwowy Instytut Badawczy*, Warszawa 2013.
[8] Ravshanovich K.A., Yamaguchi H., Matsumoto Y., Tomida N. Unob S., *Mechanism of noise generation from a modular expansion joint under vehicle passage*, Engineering Structures Volume 29, Issue 9, September 2007, 2206–2218.
[9] Spuler T., Moor G., O'Suilleabhain C., *Expansion joints with low noise emission*, Tailor Made Concrete Structures – Walraven & Stoelhorst (eds.), London 2008.
[10] Steenberge M.J.M.M., *Dynamic response of expansion joints to traffic loading*, Engineering Structures, 26, 2004, 1677–1690.
[11] *Podręcznik dobrych praktyk wykonywania opracowań środowiskowych dla dróg krajowych*, J. Bohatkiewicz, J. Adamczyk, M. Tracz, A. Kokowski et al. (eds.), Kraków 2008.
[12] PN-N-01307:1994 Hałas. Dopuszczalne wartości parametrów hałasu w środowisku pracy – Wymagania dotyczące wykonywania pomiarów.
[13] *Przegląd ekologiczny w zakresie hałasu przenikającego do środowiska z wiaduktu WA-470 zlokalizowanego w ciągu autostrady A1 w rejonie Farskiej Pola w Knurowie*, J. Bohatkiewicz, S. Biernacki, M. Hałucha et al. (eds.), na zlecenie Generalnej Dyrekcji Dróg Krajowych i Autostrad, Kraków 2018.
[14] Rozporządzenie Ministra Środowiska z dnia 14 czerwca 2007 roku w sprawie dopuszczalnych poziomów hałasu w środowisku (Dz.U. 2014, poz. 112).
[15] Rozporządzenie Ministra Środowiska z dnia 16 czerwca 2011 r. w sprawie wymagań w zakresie prowadzenia pomiarów poziomów substancji lub energii w środowisku przez zarządzającego drogą, linią kolejową, linią tramwajową, lotniskiem lub portem (Dz.U. 2011 nr 140, poz. 824).
[16] *Wielowariantowa koncepcja zabezpieczenia przed hałasem generowanym w związku z eksploatacją obiektu WA-470 zlokalizowanego w ciągu autostrady A1 w rejonie Farskie Pola w Knurowie*, J. Bohatkiewicz, S. Biernacki, M. Hałucha et al. (eds.), *Pomiary hałasu w środowisku*, na zlecenie Generalnej Dyrekcji Dróg Krajowych i Autostrad, Kraków 2013.

If you want to quote this article, its proper bibliographic entry is as follow: Bohatkiewicz J., Jukowski M., Dębiński M., Hałucha M., *Study of noise originating from selected bridge expansion*, Technical Transactions, Vol. 7/2019, pp. 33–52.

TECHNICAL TRANSACTIONS 7/2019
CIVIL ENGINEERING
DOI: 10.4467/2353737XCT.19.071.10722
SUBMISSION OF THE FINAL VERSION: 31/05/2019

Grzegorz Bosak orcid.org/0000-0003-2127-3799
gbosak@pk.edu.pl
Department of Structural Mechanics, Faculty of Civil Engineering, Cracow University of Technology

Using PIV for measuring wind velocity fields in front of and behind bulkheads made from nets of different solidity ratios

Pomiar systemem PIV pola prędkości wiatru przed i za przegrodą wykonaną z siatki o różnym współczynniku wypełnienia

Abstract

This article presents description and results of an investigation using PIV for measuring wind velocity fields in front of and behind bulkheads made from nets of different solidity ratios. The basic aim of the work is to determine the characteristic features of the wind velocity field on the windward and leeward sides of nets of different solidity ratios and to present an example of the usage of a PIV system in tests in an aerodynamic tunnel. The tests were performed in a mini aerodynamic tunnel especially prepared to test the PIV system. In the work, the regulations of measurement by means of a PIV system are presented, the main elements of the system are characterised and the main advantages and difficulties of realising measurements using this type of technique are described.

Keywords: wind tunnel tests, PIV system, wind velocity field, solidity ratio, permeable wind curtain

Streszczenie

Artykuł przedstawia opis i wyniki pomiarów systemem PIV pola prędkości wiatru przed i za przegrodą wykonanej z siatki o różnym współczynniku wypełnienia. Podstawowym celem pracy jest określenie charakterystycznych cech pola prędkości wiatru po stronie nawietrznej i zawietrznej siatek o różnych współczynnikach wypełnienia oraz przedstawienie przykładowego wykorzystania systemu PIV w badaniach w tunelu aerodynamicznym. Badania przeprowadzono w mini tunelu aerodynamicznym przygotowanym specjalnie do testowania systemu PIV. W pracy ponadto przedstawiono zasady pomiaru systemem PIV, scharakteryzowano główne elementy sytemu oraz opisano podstawowe zalety i trudności realizacji pomiarów tego typu techniką.

Słowa kluczowe: badania w tunelu aerodynamicznym, PIV system, pole prędkości wiatru, współczynnik wypełnienia, przewiewne zasłony

1. Introduction

One of the basic problems concerning wind engineering using test models in aerodynamic tunnels is checking the air flow structure. Measurements of this type are used to: determine the wind-environmental comfort of passers-by in urbanised areas; investigate the propagation of pollutants; identify the flow structure of unusually shaped constructions or constructions in conditions of aerodynamic interference; identify the structure of reference fields; identify complex flow structures in cases of the occurrence of aerodynamic phenomena. Wind velocity measurements are most often performed using thermo-anemometers, or vane or cup anemometers. Measurements of this type are conducted, in most cases, at a small number of points, these devices introduce disturbances to the measurement area and the obtained velocity values in the points of the measurement area are usually given in the form of mean values.

Other measurement techniques are used in cases where there is a requirement to measure instantaneous wind velocity fields and there is a need to determine the velocity vector in many points of space at a given moment of time. One of these other measurement techniques is a method of optical, non-invasive measurement of the wind velocity field using PIV (particle image velocimetry) methodology.

This paper presents the principle of measuring by means of a PIV system. The main elements of the PIV system at the Laboratory of Wind Engineering at Cracow University of Technology are described. The paper also presents an example of work performed using this system. The study presents a description and results of PIV measurements of a wind velocity field in front of and behind a bulkhead made from nets of different solidity ratios. Solidity ratio η is defined as the ratio of the effective area of a net material, normal to the wind direction, divided by the area enclosed by the boundary of the whole net normal to the wind direction. Five net cases were considered. Measurements were made in flat areas both in front of and behind the net in which one-way flow was observed.

2. Description of the experiment

The measurements were conducted in a MTT250 mini aerodynamic tunnel, especially built for PIV applications by the author of this study and described in point 4. The measurement configuration in the tunnel space is shown in Fig. 1. On the measuring stand, the analysed nets were spread in the form of a rigid flat plastic square meshed net, the solidity ratio of which was $\eta = 0.25$. The net itself was analysed as a mesh with a solidity ratio of 0.25. Six cases were considered: N0 – no net, flow uniformity in the measurement fields was analysed; N25 – rigid mesh in the form of a net with a solidity ratio of 0.25; N50 – net with a solidity ratio of 0.5; N60 – solidity ration of 0.6; N75 – 0.75; N90 – 0.9. All analysed nets were square meshed and made of plastic. The nets were maintained in a flat geometric form due to them being spread on rigid frames during the experiment.

The square area of the 150 mm x 150 mm stand was set perpendicularly to the incoming air stream. The PIV system measured the air velocity in a flat vertical field of 250 mm x 250

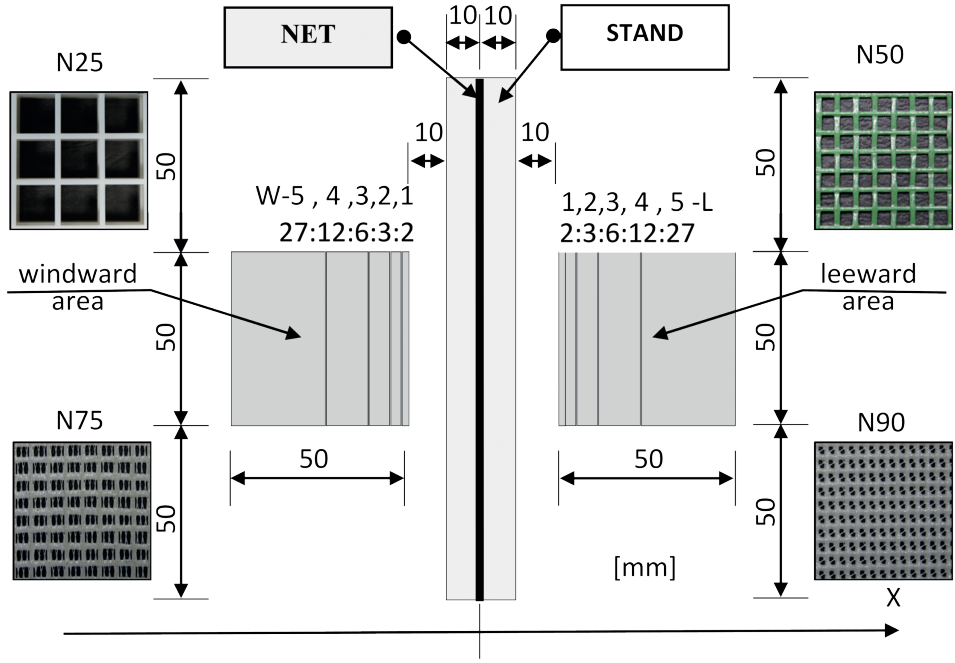

Fig. 1. Measurement configuration with photos of the example nets

mm, which included both the windward and leeward area with respect to the mesh partition. Further velocity analysis was performed in the windward and leeward fields of 50 mm x 50 mm placed at the same distances from the net in comparable positions in relation to the measurement stand as shown in Fig. 1. In these fields, one-way flow was observed with small values of vertical components. Nets with values of the solidity ratio η higher than 0.9 had the features of solid partitions, which meant that in the measurement fields, flows with significant vertical components (along the Y axis) were observed; therefore, this type of net was omitted in the present study. The windward field 'W' and the leeward field 'L' were divided into 5 rectangular sub-areas W1 to W5 and L1 to L5 with side dimensions parallel to the X axis equal to: 2, 3, 6, 12, 27 mm, respectively, as shown in Fig. 1. The measurements were performed at a sampling frequency of 500 Hz for a period of 1 s. The reference velocity during the experiment was 7 m/s, the flow turbulence was characterised by a turbulence intensity factor of 8%. Following the performing of measurements, the mean velocity field was determined on the basis of 500 instantaneous velocity field values obtained from the PIV system (time averaging). The average velocity value was then determined for each of the sub-areas (W1–W5 and L1–L5) using spatial averaging. The sub-areas were arbitrarily adopted on the basis of the wind velocity field structure analysis in the windward and leeward areas; the condition of the symmetry division of the areas was introduced in relation to the net plane. Analysis of individual measurement cases was performed on the basis of ten average air velocity values determined for individual sub-areas W1–W5 (5 values) and L1–L5 (5 values).

3. Principle of PIV system measurement

The PIV (particle image velocimetry) system provides an optical, non-invasive measurement of the fluid velocity field. The Laboratory of Wind Engineering at Cracow University of Technology is equipped with the HS (high speed) version of the LaVision system for measuring flat wind velocity fields (2D version). This type of system makes it possible to measure the field of wind velocity on a plane with a high level of flow turbulence. The basic condition for the measurement possibilities of this type of system is the lack or relatively small value of the component of the wind velocity perpendicular to the measurement plane [1–3]. The advantages of the system are non-invasive measurements occurring simultaneously across the whole measurement area with the presence of a high level of turbulence, which makes it possible to track variable wind velocity fields.

Figure 2 presents the principle of measurement by means of a 2D PIV system [4]. An air stream flow with atomized, fine molecules of the fluid called seeding is illuminated by a pulsed laser with a light of a specific wavelength in the visible range. The atomisation of these liquid particles (seeding) is performed thanks to a special device called a seeding generator. Monochrome laser light is reflected by the seeding particles and recorded using a fast camera equipped with a polarising filter that transmits light with a wavelength equal to the wavelength of the laser beam. A camera sensor of a specific resolution registers the particle system in the form of configuration of clear points at the moment of taking a picture. In HS systems, a double-frame mode is used, in which pictures are taken in pairs at times t and $t+dt$, where dt is an arbitrarily assumed time of the time shift. In the case of recording high flow rates, the time dt is very short and measured in microseconds (μs-10^{-6} s). The pairs of two consecutive frames in dt time are recorded with the selected frequency which is the frame rate. The limit values of the sampling frequency of the signal and dt time are dependent and limited by the parameters of the measuring equipment. The measurement process is the recording of a sequence of good quality images with an appropriate level of seeding density

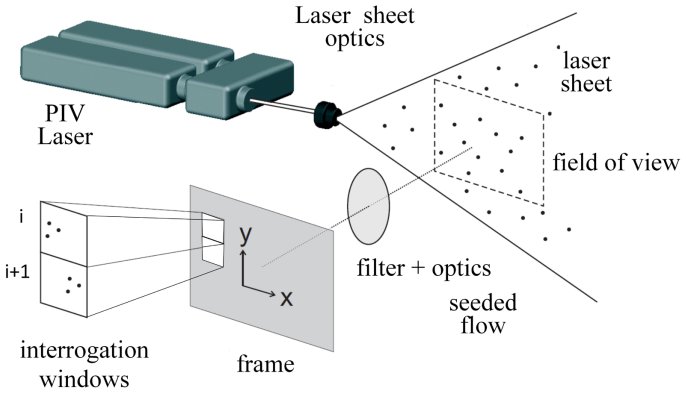

Fig. 2. Scheme of PIV2D system measurement configuration [4]

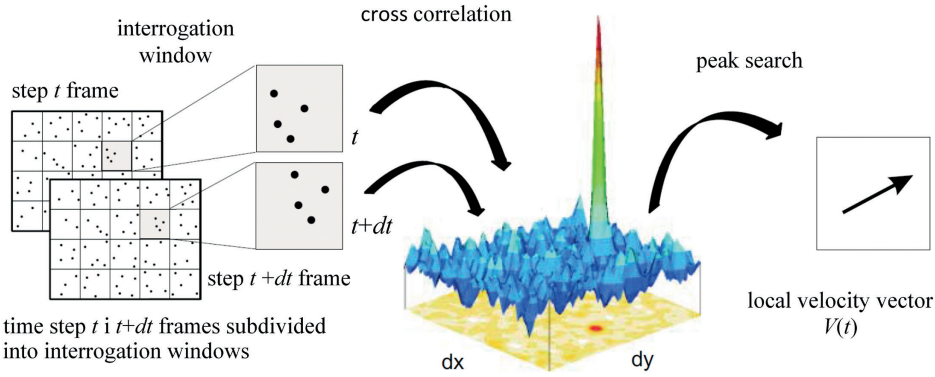

Fig. 3. Scheme of velocity vector calculations by using a cross correlation function in a double frame recording mode [4]

and correctly selected in relation to the wind velocity field structure, the signal sampling frequencies and the *dt* shift time.

During the experiments, the density of particle seeding was around 300 particles/cm^2 and the shift time parameter value *dt* was approximately 200 μs.

The calculation process based on the sequence of images of velocity vectors in a given measurement field is made by determining the cross correlation of frames differing in execution time by *dt* (see Fig. 3).

The calculation is performed by dividing the images from the moment *t* and *t*+*dt* into interrogation windows of a specific size, measured in relation to the pixels of the camera sensor. A basic requirement of the measurement is that the system of seeding particles in a given interrogation window at time of *t* and *t*+*dt* does not differ from each other significantly. Of course, the particle system changes its location in the interrogation window. If a number of particles leaves the given interrogation window, the distances and the arrangement of particles change slightly. Nevertheless, if the time *dt* is correctly matched to the stream flow structure, in the cross correlation product of the data image of the two interrogation windows in moments *t* and *t*+*dt*, a clear maximum of the cross correlation function is observed. The location of this maximum indicates the translational translocation of the interrogation window in a given plane, and using the known time of shifting *dt*, the desired value of velocity can be calculated. Thus, the movement of each interrogation window is of a translational nature described by one velocity vector. In the simplest form, when there is no possibility to overlap interrogation windows on each other, the field of wind velocity in a given area is described by the number of vectors equal to the number of interrogation windows into which images with resolution equal to the resolution of the camera were divided. It should be emphasised that the structure of the frame division into the interrogation windows during the calculations is of fundamental importance in the process of determining the correct wind velocity field [5].

4. Research stand

The measurements were made using the LaVision HS PIV 2D system and were performed in a MTT 250 PIV mini wind tunnel built by the author of this study. The mini tunnel with an open circuit had cylindrical inlet and outlet channels of 400 mm in diameter. The cube--shaped measuring space had interior dimensions of 500 mm. The square measuring field of 250 mm by 250 mm was located in the vertical plane, and its geometric centre overlapped the geometric centre of the measurement space. The measuring space section was equipped with laser-sight glasses and cameras, so that there are no distortions of the laser plane and the image recorded by the camera. A horizontal rotary table for mounting models, in such a way as to enable manipulation of their vertical position, was placed in the measurement space. An openwork screen was installed in the intake duct, ordering the air stream at the inlet into the space of the tunnel measurement section. The air circulation is generated by the suction of the fan located at the end of the outlet duct. The average air velocity in the measuring area of the tunnel is regulated by the rotation of an inverter-controlled fan and can reach a maximum value of 10 m/s. The average value of the turbulence intensity factor for the reference field of the measurement field (measuring area without the model) is 8%. The system's camera can take 1280 photos per second with at full resolution (2016 pixels x 2016 pixels). This means that in the double frame mode, the maximum sampling frequency of the signal can be 640 Hz. A pulsed laser with two laser heads generates a laser beam with a wavelength of 527 nm (green laser) with regulated single-pulse energy of up to 30 mJ (class IV laser). The laser head

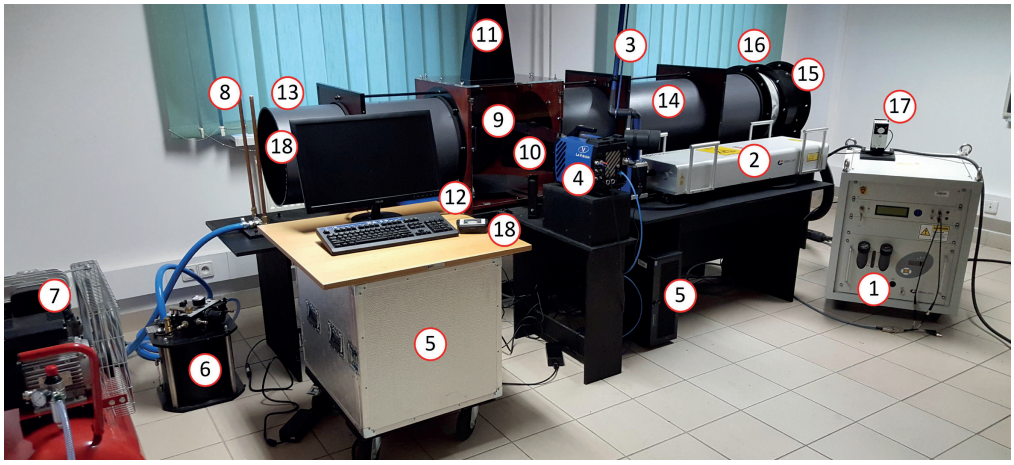

Fig. 4. Main elements of MTT 250 PIV mini tunnel and HS PIV 2D LaVision system: 1) power supply and laser cooling system unit, 2) LDY304PIV laser head, 3) optic system with laser beam guiding arm, 4) ImagerProHS4M fast camera, 5) computer system, 6) PIVPart45 seeding generator, 7) compressor-supplied seeding generator, 8) seeding distributor at the tunnel inlet, 9) working section of the tunnel, 10) window for photographing tunnel working section 11) laser beam inlet to the tunnel working section, 12) LaVision HSC v.2 high-speed controller, 13) inlet tunnel tube, 14) outlet tunnel tube, 15) fan placed on the anti-vibration elements, 16) anti-vibration connection, 17) inverter controlling fan rotation, 18) openwork screen (inside of the inlet tube)

is cooled with deionised water of specified parameters. The whole system is supported by LaVision's DaVis 8.4 software. Figure 4 presents the main elements of the mini tunnel and the PIV system of the Laboratory of Wind Engineering at Cracow University of Technology.

5. Results of the performed tests

The results of the PIV system measurement were averaged over time (see Section 2), obtaining the fields of average wind velocity presented for individual net cases in Fig. 5. Case N0 presents the measurement in the absence of a net. Case N25 is the measurement situation for the stand and the rigid net frame with the 0.25 solidity ratio. The next four cases are situations where the nets of the following solidity ratios are distributed: N50- $\eta = 0.5$, N60- $\eta = 0.6$, N75- $\eta = 0.75$, N90- $\eta = 0.9$.

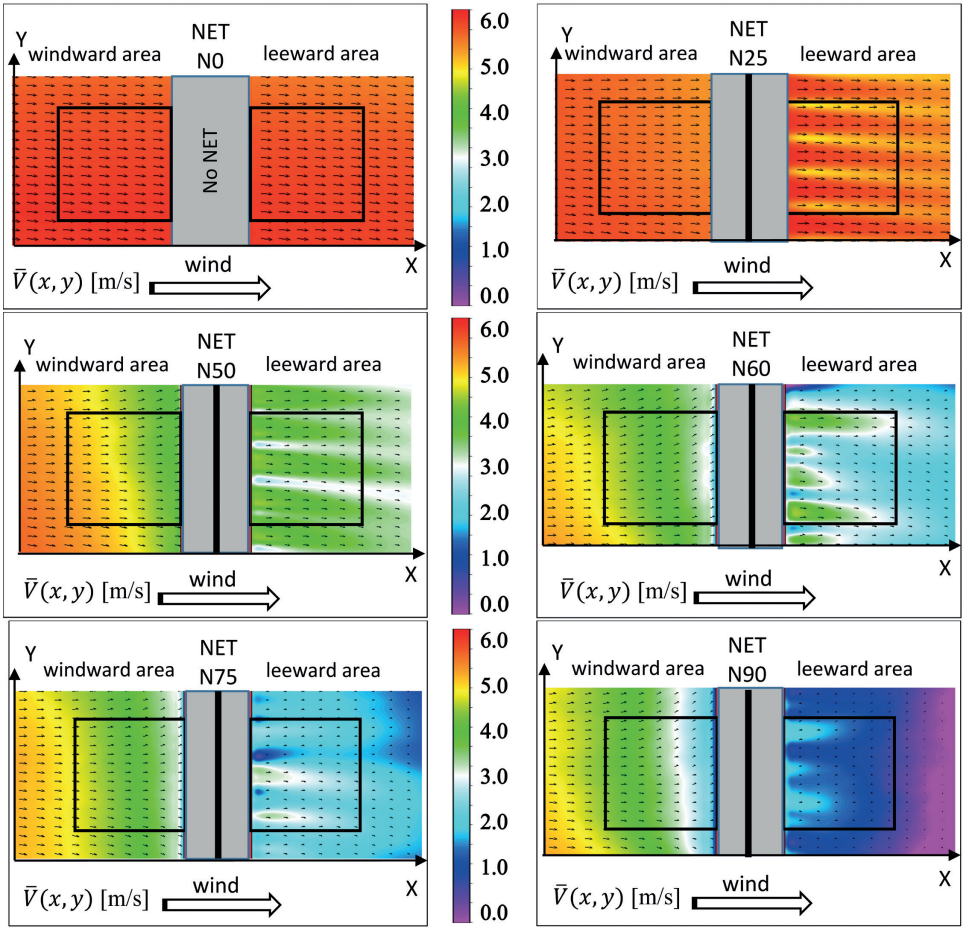

Fig. 5. Maps of mean (time averaged) wind velocity over windward W and leeward L fields obtained in the analysed measurement configurations

The coefficients of average wind velocity values were then determined for individual sub--areas (W1–W5, L1–L5) in accordance with formula (1):

$$C_v = \frac{\bar{V}}{V_{ref}} \tag{1}$$

where: $\bar{V}$ - mean velocity value in particular subarea, *Vref* – reference velocity.

The results are presented in Fig. 6.

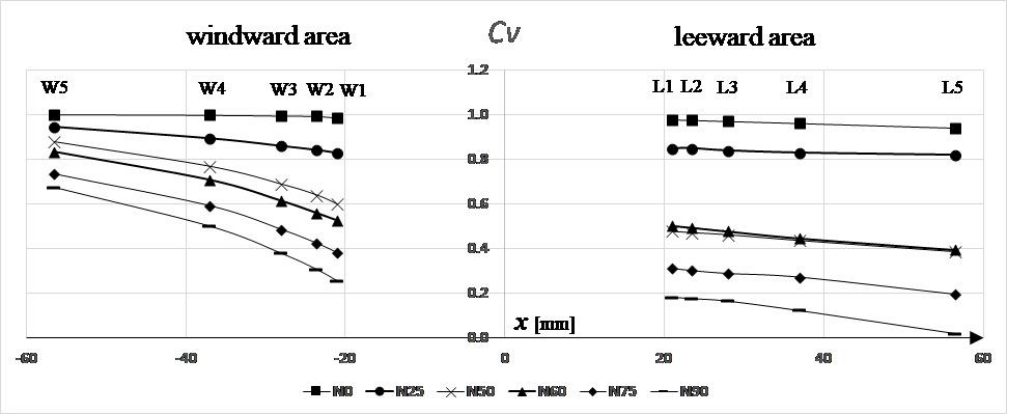

Fig. 6. Mean (time & spatial averaged) wind velocity distributions over windward and leeward subareas in the analysed measurement configurations

As a measure of the air velocity coefficient size change in the windward field Δ*VW* and leeward field Δ*VL*, the velocity coefficient difference in the extreme sub-areas of the given field was considered in accordance with formulas (2). The difference in the air velocity coefficient on both sides of the Δ*VN* baffle was calculated according to formula (3).

$$\Delta V_W = C_V(W1) - C_V(W5),\ \Delta V_L = C_V(L5) - C_V(L1) \tag{2}$$

$$\Delta V_N = C_V(L1) - C_V(W1) \tag{3}$$

Next, the quotient Δ*VL*/Δ*VW* was calculated. The above-defined values for individual meshes of different solidity ratio η, calculated using the results of measurements, are presented in Fig. 7.

Analysis of the results shows that:

- the decrease in the velocity coefficients in the windward field Δ*VW* and the leeward Δ*VL* field is directly proportional to the mesh solidity ratio η; the windward field is characterised by greater dynamics of the velocity drop than the leeward field;
- the velocity coefficient change on both sides of the Δ*VN* net is directly proportional to the mesh solidity ratio η;

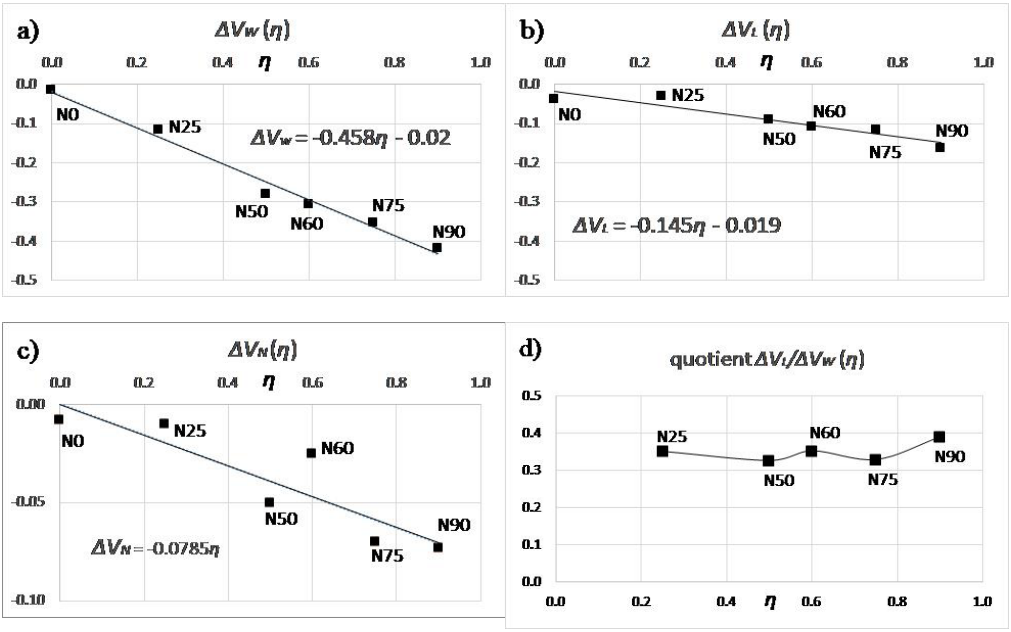

Fig. 7. Values of: a) ΔVW, b) ΔVL, c) ΔVN, d) $\Delta VL\ /\Delta VW$ in the analysed measurement configurations

- in the analysed wind zone configuration, the quotient $\Delta VL/\Delta VW$ is approximately 0.35;
- due to the small dimensions of the measurement areas and the near proximity of the measurement areas to the nets, the values of the analysed quantities can be considered as limited values (with $\Delta x \to 0$).

6. Conclusions

This paper has presented an example of the application of the PIV system for measuring the wind velocity field. As a result of the conducted experiments, the characteristic features of the wind field on the windward and leeward sides of meshes with different solidity ratios were determined. In practice, this kind of analysis could be used in the investigation of solutions for new utility buildings. It is now common to use technology in which ventilation systems are assembled in the form of permeable wind curtains on the side walls of halls and buildings that are mainly used as storehouses, warehouses, driers, cattle sheds, pigsties and stables. Such a solution assures a continuous air exchange inside the object; moreover, it protects against sun exposure and insects, as well as limiting dust getting in from outside. Returning to measurements, due to the flow structure and the small dimensions of the measurement areas, the use of the PIV system for performing non-invasive measurements in the entire analysed area was justified and led to uninterrupted results from measurement equipment. Due to the measurement methodology, the PIV system is a tool that enables high visualisation of the flow

structure. Obtaining the air velocity values across a large number of points enables the precise analysis of the vector field structure of the velocity. In the case of variant and serial works, the system enables the rapid assessment of changes in the flow structure [3]. As with any measuring technique, it has its advantages, but it can also have a number of problems, difficulties and limitations. Clearly, the advantages of the system are as follows: the instantaneous measurement of wind velocity fields at many points; the fact that there are virtually no disturbances in the flow structure; the efficiency of flow visualisation; the ability to rapidly track changing flow structures; the obtaining of effective and fast measurement in serial variant tests. The main disadvantages of the use of this system are related, as in any optical systems, to the limited visual accessibility of the area of interest. During the PIV system measurements: the need to expose the measurement area to laser light and the need for camera registration of the points in the analysed area are the basic limits of the technics. In addition, some complex flow structures, such as areas with very large differences in velocity, and turbulences within small spatial cells lead to serious measurement difficulties. A significant consideration regarding the possibility of using the system is its high purchase price, significant operating costs, the requirement for highly qualified and experienced technicians.

References

[1] Adrian R., Westerweel J., *Particle Image Velocimetry*, Cambridge University Press, New York 2011.

[2] Adrian R.J., *Twenty years of particle image velocimetry*, Exp Fluids 39, 2005, 159–169.

[3] Bin L., Shan-Qun Ch., *Experimental study of flow past obstacles by PIV*, Procedia Engineering 126, 2015, 537–541.

[4] LaVision, *PIV Manual*, Göttingen, 2016.

[5] Wieneke B., Pfeiffer K., *Adaptive PIV with variable interrogation window size and shape*, 15th Int Symp on Applications of Laser Techniques to Fluid Mechanics, Lisbon 2010.

If you want to quote this article, its proper bibliographic entry is as follow: Bosak G., *Using piv for measuring wind velocity fields in front of and behind bulkheads made from nets of different solidity ratios*, Technical Transactions, Vol. 7/2019, pp. 53–62.

TECHNICAL TRANSACTIONS 7/2019
CIVIL ENGINEERING
DOI: 10.4467/2353737XCT.19.072.10723
SUBMISSION OF THE FINAL VERSION: 3/06/2019

Łukasz Flaga orcid.org/0000-0001-9650-4913
lukasz.flaga@interia.pl
Aleksander Pistol orcid.org/0000-0002-6282-4596
aleksander.pistol@gmail.com
Piotr Krajewski orcid.org/0000-0002-2635-7273
piotrekrajewski@gmail.com
Andrzej Flaga orcid.org/0000-0003-1759-4872
liwpk@windlab.pl
Institute of Structural Mechanics, Cracow University of Technology

Model tests of dynamic action on the atmospheric boundary layer – linear configuration of ventilation towers on a rough terrain

Badania modelowe dynamicznego oddziaływania na warstwę przyziemną atmosfery – konfiguracja liniowa wież wentylacyjnych na chropowatym terenie

Abstract

This paper describes model tests conducted at the Wind Engineering Laboratory of Cracow University of Technology as the first stage of studies on dynamic action on the atmospheric boundary layer in order to reduce the effects of air pollution and smog. It focuses on the cooperation between a series of ventilation towers placed one by one (or row by row) in order to generate a continuous airstream with sufficient velocity to aid the natural ventilation of urban areas. The tests were conducted for three different terrain categories with varying roughness. Also tested were different wind speeds, different spacing between the towers and different configurations of the towers in each row. As a preliminary set of tests, this enabled verification of the feasibility of the solution and its effectiveness on a rough terrain that simulates urban areas.

Keywords: wind engineering, smog reduction, environmental engineering, urban ventilation, terrain roughness

Streszczenie

Niniejszy artykuł opisuje badania modelowe przeprowadzone w Laboratorium Inżynierii Wiatrowej Politechniki Krakowskiej w ramach pierwszego etapu studium dynamicznego oddziaływania na warstwę przyziemną atmosfery w celu redukcji zanieczyszczenia powietrza i smogu. Praca skupia się na współpracy kilku wież wentylacyjnych ustawionych jedna za drugą (lub rząd za rzędem) w celu utworzenia ciągłej strugi powietrza o dostatecznej prędkości, by wspomóc naturalną wentylację obszarów zurbanizowanych. Badania przeprowadzono dla trzech różnych kategorii chropowatości terenu. Ponadto sprawdzono wpływ różnych prędkości strugi, różnych odległości pomiędzy wieżami i różnych wzajemnych konfiguracji wież w każdym rzędzie. Przeprowadzone badania wstępne pozwoliły na weryfikację wykonalności tego rozwiązania oraz jego wydajności na chropowatym terenie odpowiadającym obszarom zurbanizowanym.

Słowa kluczowe: inżynieria wiatrowa, redukcja smogu, inżynieria środowiska, przewietrzanie miast, chropowatość terenu

1. Introduction

The problem of smog and excessive air pollution is faced by many modern cities. Thus far, the countermeasures for this problem have been limited to restrictions of car traffic, the modernisation of coal-fuelled heating systems and active air purifiers, which have a very localised impact range. The idea of these studies is to apply large ventilation towers (shown in Fig. 1) for creating artificial airstreams within cities. Groups of such devices would form part of a large-scale ventilation system. Its objective would be to ensure the uninterrupted operation of natural ventilation arteries of the cities, even during windless weather (see Fig. 2). This should effectively improve the urban air quality by supporting the natural system of air exchange and regeneration. In order to obtain maximum efficiency of the system, some investigations and tests need to be performed to define both the most vital points of the urban layout requiring support by such system and the range of the most economic configuration of the system elements.

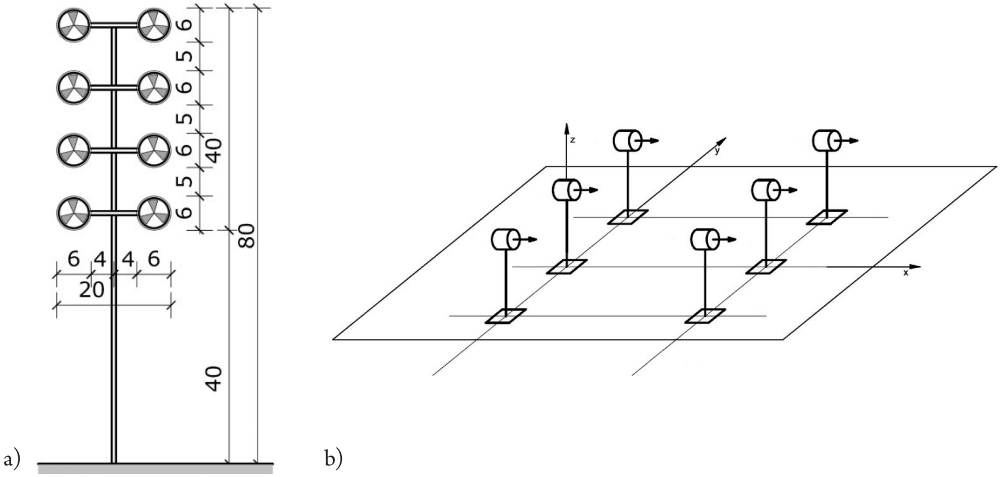

Fig. 1. Scheme of the proposed ventilation tower (a) with 10 large fans (all dimensions in [m]) and configuration of system elements for creating artificial airstreams (b)

This large-scale ventilation system would be put to use during windless periods when pollution is accumulated in the air. If proven to work (i.e. proven to create a continuous airstream of desirable wind speed) at the scale of the model and on rough terrain, the solution should be tested at a larger scale before implementation in real life. Furthermore, subsequent stages of preliminary tests will focus on the manner of expelling the polluted air from the atmospheric boundary layer and the cooperation between the ventilation towers and the exhaust system.

The literature review will cover the study of dynamic action on the atmospheric boundary layer. The authors aim to investigate whether it is possible to force the movement of air mass on such a large scale. The study will also include an analysis of the effectiveness of dynamic action on the atmospheric boundary layer. To emphasise the pioneering nature of this type of research, it is worthwhile to analyse the current state of knowledge in the field of urban

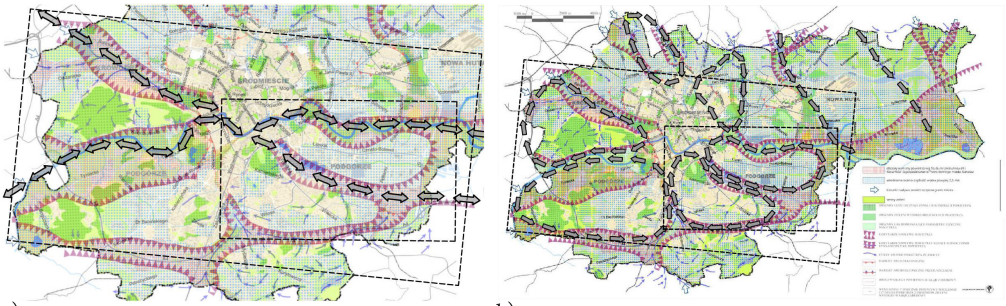

a) b)

Fig. 2. Concept sketch of additional air streams mechanically generated on the example of an air exchange and regeneration system for Cracow [1]: a) horizontal air streams in parallel configuration of stream generation points; b) horizontal vortex air streams in circulating configurations of stream generation points

ventilation as well as the forced movement of air masses. Thus, the following are some of the relevant studies that have been conducted and described so far:

- **studies of natural ventilation channels in urban areas**: CFD simulations of air pollution dispersion in urban areas [2, 3], wind tunnel tests of wind conditions in urban areas [4], comparisons of CFD results with wind tunnel measurements [3], influence of the terrain (buildings, roughness, etc.) on natural ventilation channels [5–8];
- **influence of wind conditions** on the transport of air pollution outside urban areas as well as on the change of urban microclimatic conditions [9];
- **study on the phenomenon of forced air movement on a small scale** (home ventilation) [10, 11];
- **study of natural vertical air movement**: the impact of cities' thermal conditions on their ventilation [12-14];
- **study of forced vertical air movement**: increasing the efficiency of small-scale ventilation by creating a tornado-like artificial vortex [15]; patent for a cooling tower with forced ventilation and natural draft [16] or cooling tower discharging of polluted air after breaking through the inversion layer [17, 18]; study of the process for reducing smog by the chimney inversion/injector effect – sucking warmer and cleaner air from the higher layers towards the ground via pipelines [19];
- **aerodynamic interference test**: mainly aerodynamic interference study of buildings [20]; investigation of generated air-stream interference in only the vertical direction and on a small scale [21];
- **similarity criteria for the phenomenon of dynamic action on the atmospheric boundary layer**: only own works discussed in the pre-test section.

Summing up the above literature review, it is evident that there are many gaps in the state of knowledge concerning the phenomenon of dynamic action on atmospheric boundary layer. However, paper [22] suggests using an air-exchange and regeneration system as a global active measure against bad aero-sanitary conditions in urban areas. Thus far, such a system has

been neither created nor applied. What is more, it has not been investigated whether it would be physically possible to create such a system or whether it be economically justified.

No one has ever thoroughly investigated the mechanical movements of air masses on such a large scale. Moreover, the effectiveness of such a dynamic action is not known. Additionally, there has so far been little information about the aerodynamic interference of the generated air streams. This phenomenon is particularly important since, as a result of air-stream interference, the efficiency of the system may be dramatically improved or hampered. Therefore, the objectives of the study were: the development of a practical model of air flow in urban areas along with elaborating basic similarity criteria for the analysed issue; the preparation of a work station for the measurement of an air-flow velocity field generated by ventilation towers in chosen variants of parallel configuration; the conducting of model tests to measure the air-flow velocity field in the proximity of ventilation towers in parallel configuration with different fan--rotation speeds, the number and location of the fans; smoke visualisation of the phenomena.

2. Testing methods

2.1. Similarity criteria

The first stage of tests concerned the dimension analysis required for this research. It was decided that most of the tests would be conducted on scale models. Model tests reflect reality with a satisfactory level of accuracy if the basic relations in the analysed phenomenon are preserved. Thus, the first key step in the initial test was to define these relations (i.e. similarity criteria) which must be fulfilled during the investigations. The following elements of the system were analysed, from the most basic to the most complex sets:

2.1.1. Single ventilation tower with similar multiple parallel fans

As first, a ventilation tower equipped with similar multiple parallel fans was studied [23]. Its concept scheme showing the relevant parameters is shown in Fig. 3.

The x-component of the mean air-stream velocity at point P (x_p, y_p, z_p) marked as V_{xP} is a function dependent on the following factors: geometric parameters of a ventilation tower (h_B, d, h, h_D, c, b); geometric parameters of a single fan $(d_w, l_w, \ldots) = (g_w)$; mean outlet air velocity (v_w); coordinates of point P: (x_p, y_p, z_p); physical characteristics of air (ρ - mass density, μ - dynamic viscosity, $\nu = \frac{\mu}{\rho}$ - kinematic viscosity); terrain roughness parameters (k_{rt} – mean height of the surface irregularity – assuming quite uniformly rough terrain).

Based on all the above parameters, the undermentioned functional relationship can be stated:

$$V_{xP} = F\left[h_B, d, h, h_D, c, b; (g_w); (x_p, y_p, z_p); v_w, \rho, \mu; k_{rt}\right]. \quad (1)$$

Assuming the dimensional base of the problem as (ρ, vw, h) and using the Π (Buckingham) theorem that concerns the dimensional analysis, the following dimensionless function is defined:

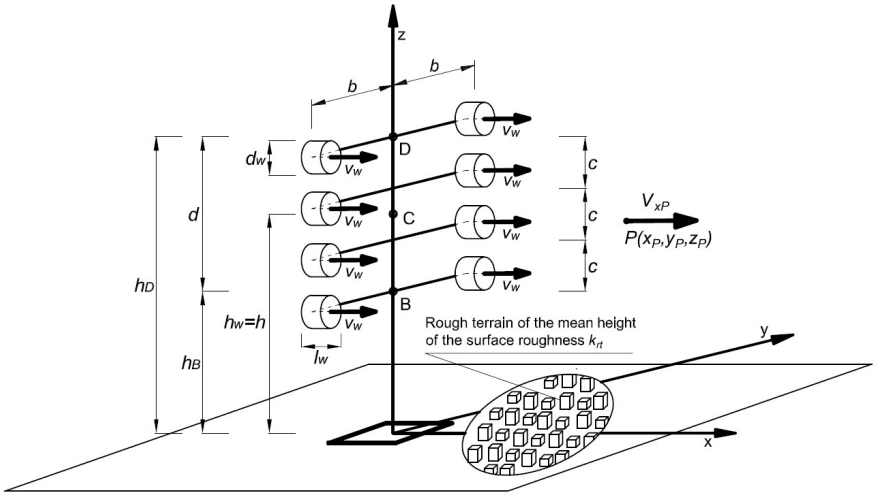

Fig. 3. Sketch of ventilation tower equipped with eight fans; each fan generates an air stream of mean outlet velocity v_w

$$\breve{V} = \frac{V_{xP}}{v_w} = \breve{F}[\frac{h_B}{h}, \frac{d}{h}, \frac{h}{h}, \frac{h_D}{h}, \frac{c}{h}, \frac{b}{h}; (\breve{g}_w); \left(\frac{x_P}{h}, \frac{y_P}{h}, \frac{z_P}{h}\right); \mathrm{Re}^*; \breve{k}_{rt}] \tag{2}$$

where $\mathrm{Re}^* = \frac{v_w h \rho}{\mu} = \frac{v_w h}{\nu}$ is a Reynolds number, $\breve{k}_{rt} = \frac{k_{rt}}{h}$ is the dimensionless roughness of the surface.

From the above relations, it follows that at given dimensionless geometric parameters of the ventilation tower and fans, the dimensionless velocity $\breve{V}$ depends on: dimensionless coordinates of point P $\left(\frac{x_P}{h}, \frac{y_P}{h}, \frac{z_P}{h}\right)$, Reynolds number Re and dimensionless roughness of the surface $\breve{k}_{rt}$. The easiest method of achieving the individual values of the function $\breve{F}$ is by conducting a series of model tests.

2.1.2. Single ventilation tower with one substitutive fan

The stream generation point can be modelled in a simpler way than a single ventilation tower with one substitutive fan (Fig. 4) generating an air stream of with mass flow rate Q_w equal to the sum of mass flow rates Σq_w of eight (or, in the general, n_w) fans mounted on the ventilation tower presented in Fig. 3.

In this case:

$$Q_w = \rho A_w V_w = \rho \frac{\pi D_w^2}{4} V_w, q_w = \rho a_w v_w = \rho \frac{\pi d_w^2}{4} v_w, Q_w = n_w q_w = 8 q_w \tag{3-5}$$

where A_w is the area of the substitutive fan, a_w is the area of each single fan and V_w is the mean outlet velocity of the substitutive fan. Therefore:

$$A_w V_w = 8 a_w v_w \text{ or } D_w^2 V_w = 8 d_w^2 v_w \tag{6}$$

$$V_w = 8\frac{a_w}{A_w} v_w \text{ or } V_w = 8\left(\frac{d_w}{D_w}\right)^2 v_w \tag{7}$$

Assuming $V_w = v_w$, we obtain: $A_w = 8a_w$ or $D_w = \sqrt{8}d_w$. The dimensionless functional relationship for the ventilation tower with one substitutive fan can be defined as follows:

$$\breve{V}^* = \frac{V_{xP}{}^*}{V_w} = \breve{F}^*\left[\frac{D}{H}; \left(\breve{G}_w\right); \left(\frac{x_P}{H}, \frac{y_P}{H}, \frac{z_P}{H}\right); \mathrm{Re}; \breve{k}_{rt}\right] \tag{8}$$

where: $\mathrm{Re} = \frac{V_w H}{\nu}$.

For comparable parameters of both functions $\breve{F}$ and $\breve{F}^*$, it can be stated that $\breve{V}^* = \breve{V}$. For further considerations of similarity criteria for different setups of stream generation points, it was assumed that they were modelled as ventilation towers with individual substitutive fans.

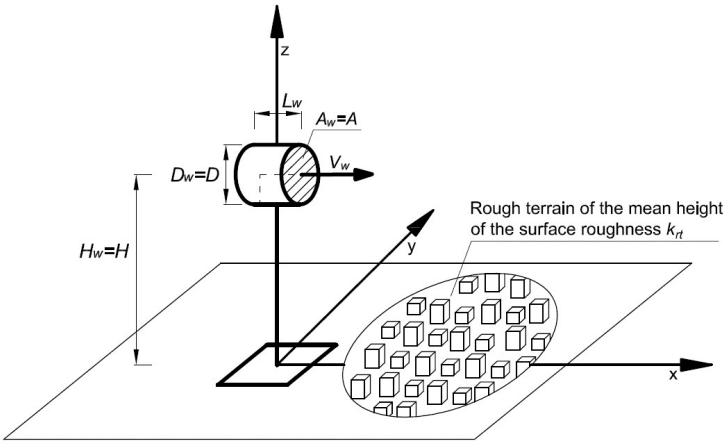

Fig. 4. Sketch of single ventilation tower with one substitutive fan

2.1.3. Array of substitutive ventilation towers

Let us now consider a general case for a system of multiple substitutive ventilation towers located at the nodes of a regular mesh where towers are located side-by-side in rows in the y-direction and one-by-one in lines in the x-direction as shown in Fig. 5. Additional parameters that apply here are: distances between rows *L*; distances between the lines *B*; the number of rows n_y; the number of lines n_x.

By conducting the above dimensional analysis, the resulting functional relationship is [23]:

$$\breve{V}^{**} = \frac{V_{xP}{}^{**}}{V_w} = \breve{F}^{**}\left[\frac{D}{H}, \frac{L}{H}, \frac{B}{H}; \left(\breve{G}_w\right); \left(\frac{x_P}{H}, \frac{y_P}{H}, \frac{z_P}{H}\right); \mathrm{Re}; \breve{k}_{rt}\right]. \tag{9}$$

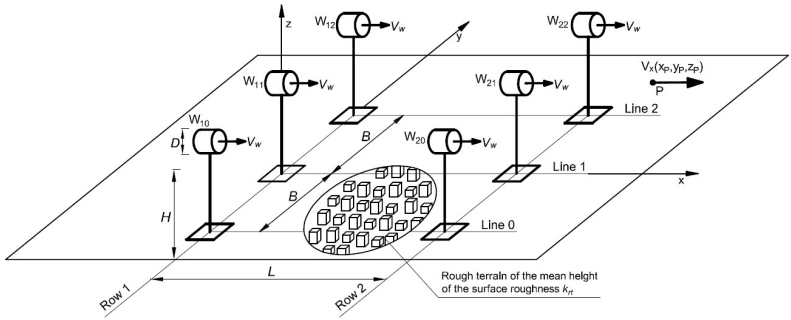

Fig. 5. Six substitutive ventilation towers on a meshed system of two rows and three lines

Based on the considerations given above, one can observe that the air velocity in the elaborated problem is related to the Reynolds number and the distance from the fans. Other geometric parameters are constant. Therefore, the conclusions are as follows: tests results obtained with a scale model are reliable; conditions required to create and maintain airstreams at full scale are the same as for the scale model.

2.2. Test models

Aerodynamic models of the ventilation tower were created separately at scales of 1:100 and 1:833. The 1:100 model accurately reflected both height and width (see Fig. 6.b) and also the number of fans. The fan elements of the ventilation towers were modelled with CPU fans of 60 x 60 mm in size. The results obtained in Series I for the 1:100 scale model were satisfactory and were therefore treated as a reference for the results obtained during further tests conducted on a smaller scale (1:833) for Series II – V [24].

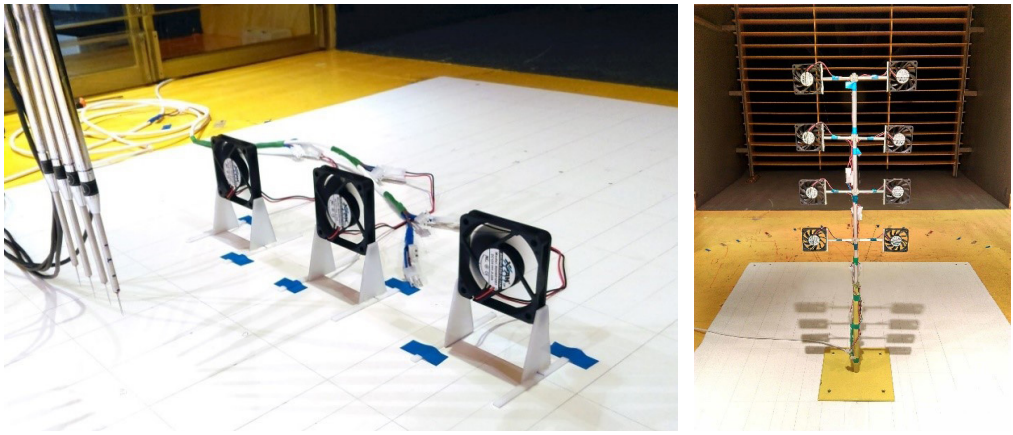

a) b)

Fig. 6. Models of ventilation towers used in model tests: set of 3 fans – substitutive ventilation towers, at 1:833 scale (a) and single ventilation tower, 1:100 scale (b)

The 1:833 scale was adopted as the most suitable scale for further tests due to the dimensions of the wind tunnel working section, the overall conditions required to generate a continuous airstream by consecutive rows of ventilation towers and available devices (CPU fans) projecting ventilation towers, which are crucial elements of the ventilation system. Each ventilation tower was modelled with the same 60 x 60 mm CPU fan that was used for the 1:100 model scale (see Fig. 6.a). However, such a strategy resulted in different proportions between the height and width of the fans recreating the ventilation towers for the 1:833 scale model and full scale ventilation towers (80 x 20 m). At this scale, only the vertical size was correctly represented (characteristic dimension adopted for further considerations is D – diameter of fan). Each fan was mounted on a simple construction in order to keep its elevation at the correct level for the chosen modelling scale (see Figs. 8.a & 8.b).

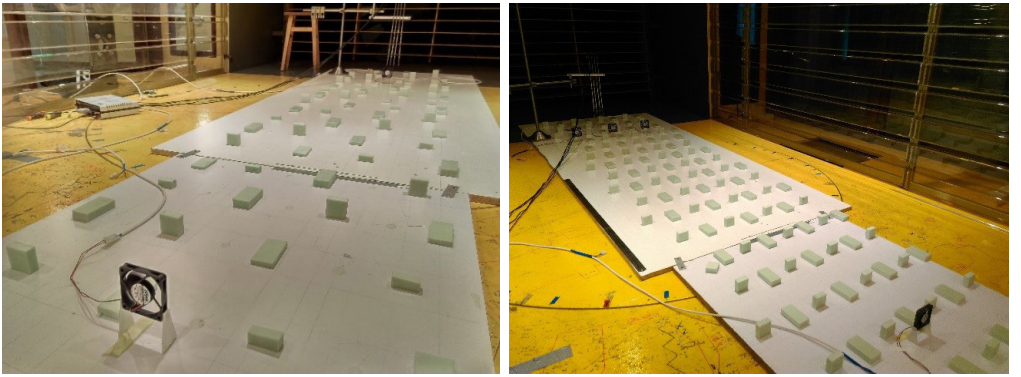

Fig. 7. Styrofoam blocks glued to the board in a pattern recreating terrain roughness for the scale model for categories III (forests and suburban areas) (a) and IV (downtown urban areas) (b) according to [25]

The models were tested in the aerodynamic tunnel of Wind Engineering Laboratory of Cracow University of Technology. The base for the models was made from a smooth wooden board. For Series VII and VIII of the tests, terrain roughness was recreated in the model scale for Categories III (forests and suburban areas) and IV (dense city-centre urban areas) in accordance with [25] (see Fig. 7). This was achieved through the application of rigid Styrofoam blocks glued to the board in a pattern that corresponds with the guidelines of the standard and based on the literature study [6, 20, 26].

2.3. Tests and measuring devices

The wind tunnel tests were conducted by measuring wind speed generated by the fans along the x-axis (see Figs. 9-11). For Series I, tests were conducted at three different heights in order to investigate the three-dimensional distribution of wind speed at each distance from the fans (as shown in Fig. 8.c). For Series II-VIII, tests were conducted at only one height, which was the centre of the fan. Each measurement was performed on four probes. For Series I, measurements were taken at a distance of 0.6 x/H (+/-50 cm) in the nearest vicinity of the

fans, and then at increasing distances of every 1.2 x/H (100 cm) from the fans (see Table 1). For the rest of the test series, measurement were taken in front of the fans at distances of every 1.5-3 x/H (10 cm) in in close proximity to the fans' and then increasing to every 4.6 x/H (30 cm) from the fans (see Table 1). For Series IV, V and VI, multiple tests were performed at each distance along each line and at the midpoint between them in order to cover all the desired points (as shown in Figs. 8.a & Fig. 8.b).

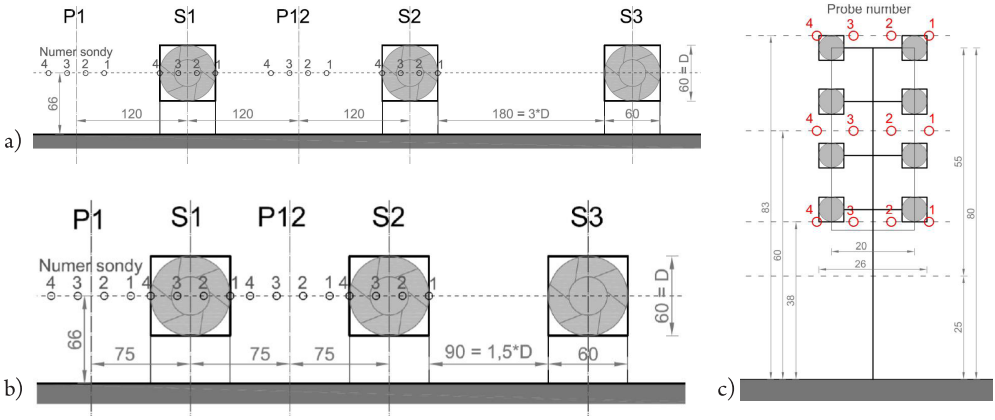

Fig. 8. Scheme of fan configuration and measurement points for: a row of 3 fans spaced at distances of 3 D (180 mm) (a), a row of 3 fans spaced at distances of 1,5 D (90 mm) (b) and a single ventilation tower at a scale of 1:100 (c)

The airstream continuity was investigated by testing the interference of two consecutive fans (or rows of fans). Between the consecutive fans, it was essential to make sure that there would be no point at which the wind speed dropped to the level of background fluctuations or below.

The velocity of the generated air stream was measured using ATU 2001 monofilament hot-wire anemometers. The air stream was generated with CPU fans produced by Xfan, model: RDH6010S1, with a nominal voltage of 12 V, 0.22 A. They were supplied by a stabilised DC power supply. The level of generated wind speed was controlled by adjusting the voltage provided to the fans.

3. Experiment implementation and model tests results

The air stream velocity and continuity investigations were conducted in eight different series as presented in Table 1 [24]. Additional two series were conducted to evaluate the influence of terrain roughness Categories III and IV. It was decided that the series of model tests would differ in the number of rows and lines in which the fans were arranged. The distances between fan rows resulting in the generation of the air stream (in order to maintain the air-flow velocity at a specified level) were identified empirically during preliminary model tests.

Table 1. Details of model test series

Series no.	Description
Series I	Single ventilation tower at a scale of 1:100, nominal voltage of 13.6 V
	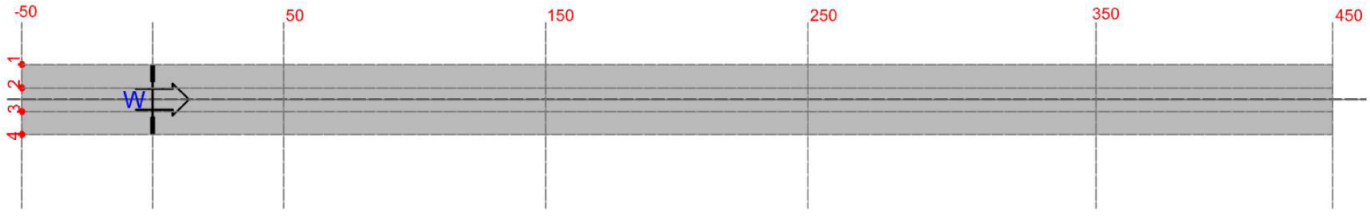
Series II	Single fan at varying wind speed generated with nominal voltages of 5.6 V, 7.7 V, 9.5 V, 11.4 V, 13.6 V
	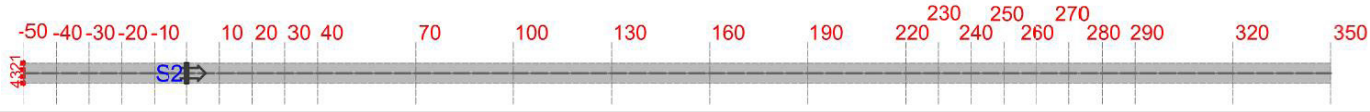
Series III	Two fans placed one by one at a distance of 37.9 x/H (250 cm) and 42.4 x/H (280 cm), nominal voltage of 13.6 V
	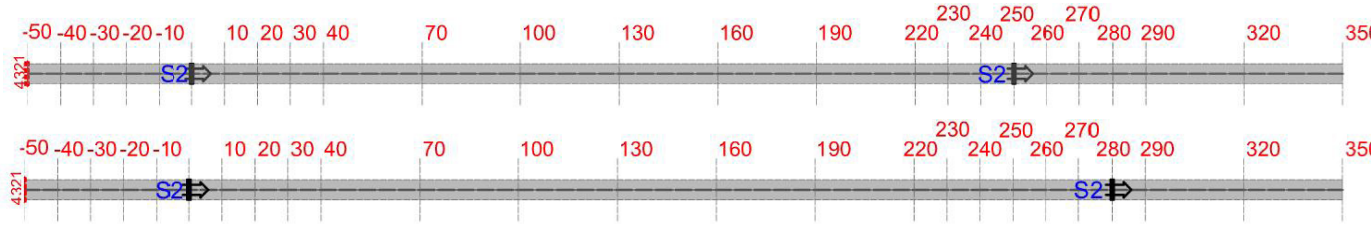
Series IV	A row of 3 fans spaced at distances of 1.5 D (90 mm), nominal voltage of 13.6 V
	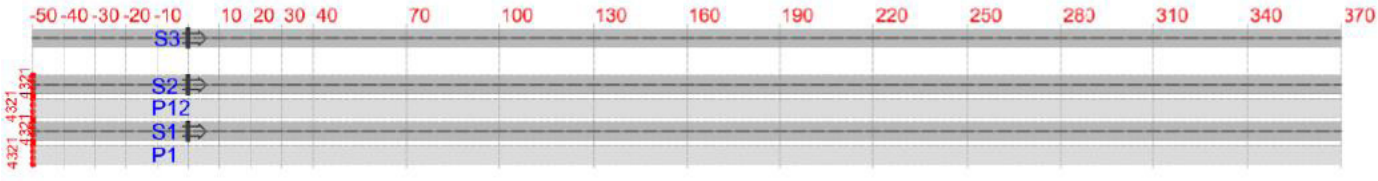

Series V	A row of 3 fans spaced at distances of 3 D (180 mm), nominal voltage of 13.6 V

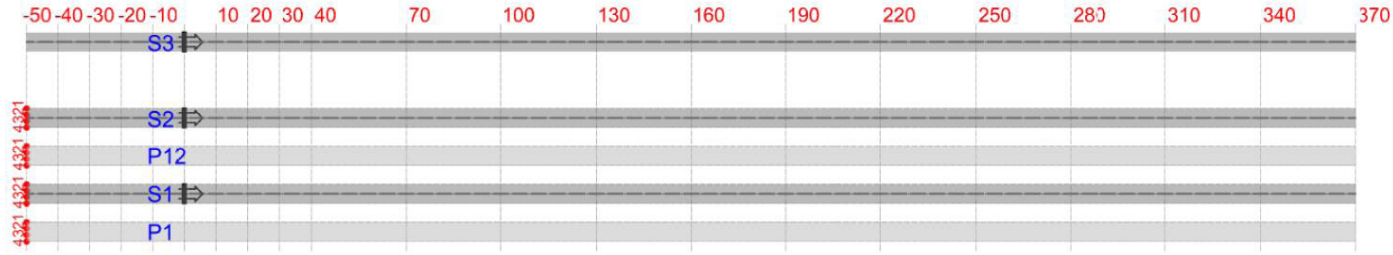

Series VI	Two rows of 3 fans spaced at distances of 3 D (180 mm), distance between rows: 56 x/H (370 cm), nominal voltage of 13.6 V

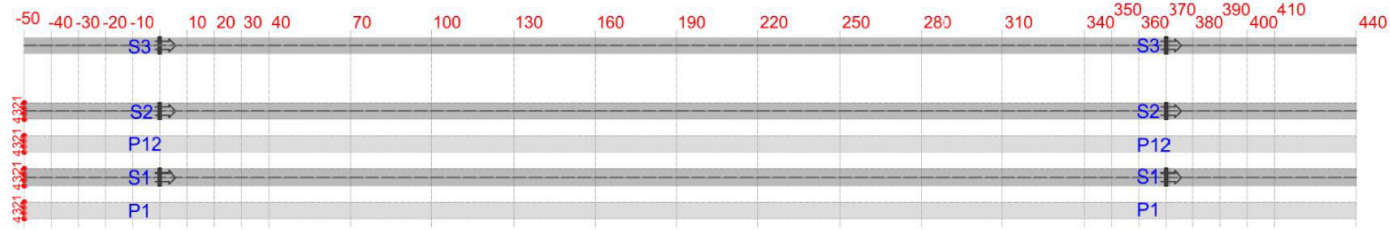

Series VII	Single fan on category III and IV terrain roughness at varying wind speed generated with nominal voltages of 4.0 V, 5.6 V, 9.5 V, 13.6 V

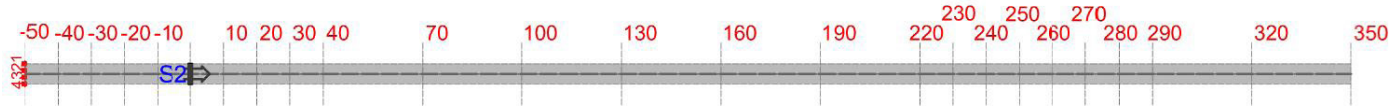

Series VIII	Two fans placed one by one at a distance of 37.9 x/H (250 cm) on Category III and IV terrain roughness, nominal voltage of 13.6 V

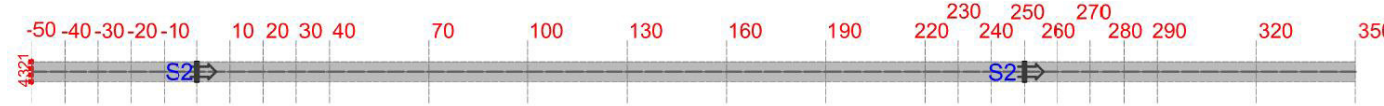

The relative wind velocity distribution is presented in Fig. 9 as a result of tests Series II. It can be observed that at a distance of more than 4.6 x/H (30 cm at the 1:833 experiment scale), the relative wind velocity is maintained on a similar level for every tested rotation speed. This means that the Reynolds number is not a significant factor influencing the results in small scale experiments for the measured range of velocity, as was concluded from the dimensional analysis.

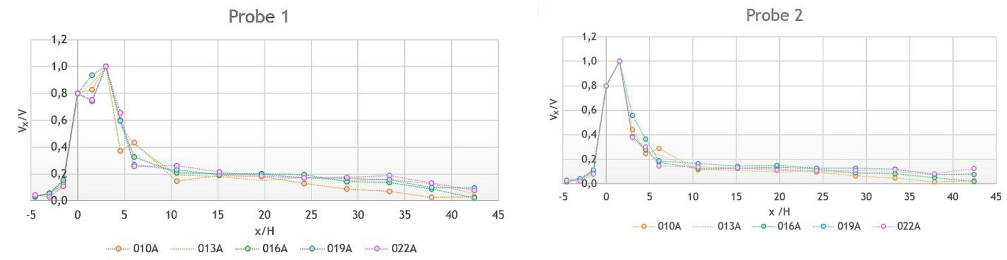

a) b)

Fig. 9. Model tests results – Series II, comparison of air velocity for different voltages provided to the fans obtained from probe 1 (a) and probe 2 (b)

The range of air suction in front of the fan is limited to no more than 1.5-3 x/H distance (10-20 cm at the scale of the experiment) (see Fig. 9). Thus, it is economically reasonable to place the second row of fans at a distance where the air stream is fading away (see Fig. 10). For this particular study case, the distance was 42.4 x/H (280 cm in experiment scale). Placing the rows of fans closer to each other has an insignificant influence on increasing the air-flow velocity, thus there is no reason for it. However, due to the potential reduction of relative wind velocity caused by adding terrain roughness, a 37.9 x/H (250 cm) distance to the second row of fans was assumed at the initial stage of tests and it was consequently implemented through all series.

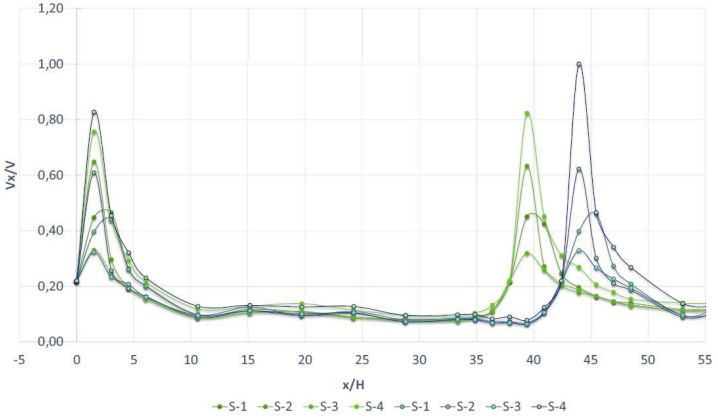

Fig. 10. Model tests results – series III: two fans placed one by one at a distance of 37.9 x/H (250 cm) and 42.4 x/H (280 cm), nominal voltage of 13.6 V

The spread of fans in a single row was evaluated at both 1.5 *D* (Series III) and 3 *D* (Series IV). The air flow velocity at the end of the stream (i.e. at a distance of 56 x/H = 370 cm at the experiment scale) reached similar values for both cases, although at the spacing of 3 *D*, the total width of the stream, so also the area of action of the fans, was two times larger than at 1.5 *D* with the same number of fans (see Fig. 11). Therefore, it was decided to increase the spread of the fans on the ventilation tower to 3 *D* and continue the tests with this spacing.

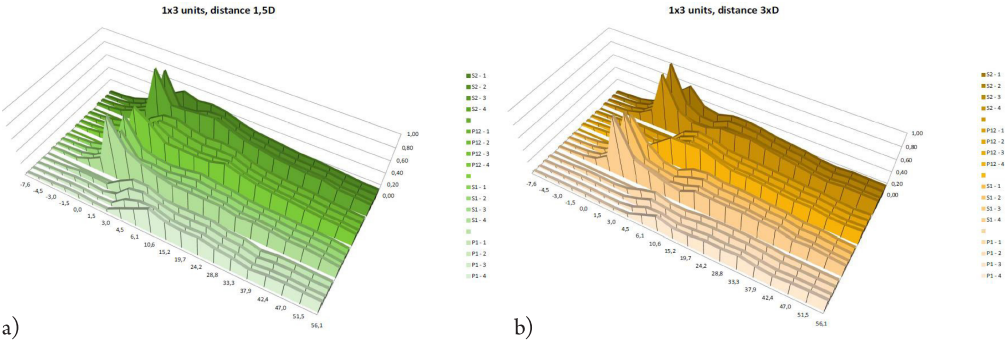

a) b)

Fig. 11. Model tests results – Series IV & V: a row of 3 fans spaced at distances of 1.5 *D* (90 mm) (a) and Series IV: a row of 3 fans spaced at distances of 3 *D* (180 mm) (b)

The wide stream generated with 3 fans spaced at distances of 3 *D* can be successfully maintained by adding another row of fans at a distance of 56 x/H (370 cm) (see Fig. 12). No significant differences of air flow velocity were observed in close proximity in front of the 2nd row (i.e. 51.5-54.6 x/H = 340-360 cm); thus, it was concluded that the location of the 2nd row was correct. Increasing the distance further could result in decreasing the air-flow velocity or even interrupting the continuity of the stream.

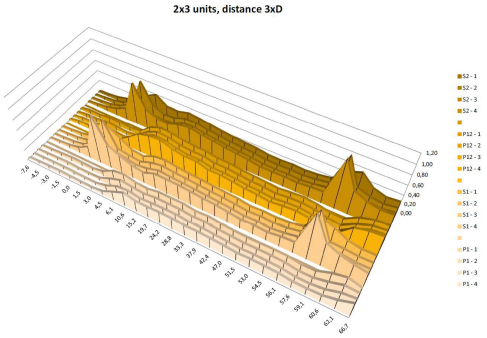

Fig. 12. Model tests results – Series VI: two rows of 3 fans spaced at distances of 3 *D* (180 mm), distance between rows: 56 x/H = 370 cm at the scale of the experiment, nominal voltage of 13.6 V

The relative wind velocity distribution at three different heights for the 1:100 scale model is presented in Fig. 13 as results of Series I (compare to Fig. 8.c). Despite the change of the number of fans from 1 to 8 and the change of scale from 1:833 to 1:100, the flow pattern of

the airstream was similar to the other series. This confirms the thesis that in the model tests, a group of fans operating close to each other can be replaced by a single fan of a larger size.

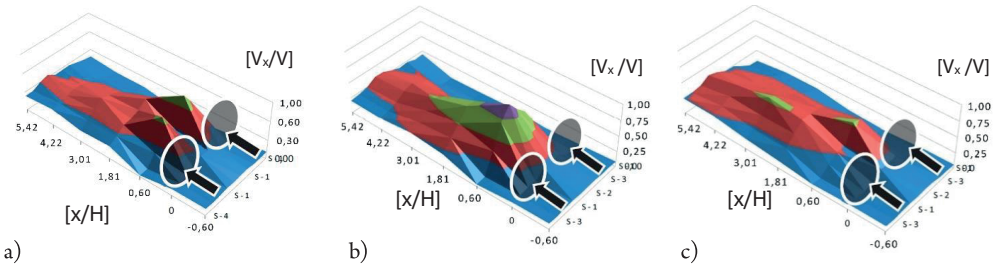

a) b) c)

Fig. 13. Model tests results – Series I: relative wind velocity distribution at level 1 = 38 cm (a), level 2 = 60 cm (b) & level 3 = 83 cm (c) for a single ventilation tower at a scale of 1:100, nominal voltage of 13.6 V

A comparison of the results obtained for different nominal voltages of a single fan for terrain categories III & IV is presented in Fig. 14 [27]. The shape of the airstream obtained for Category III of terrain roughness is similar to the shape of the airstream obtained for category 0. One can observe differences in the shape of airstream obtained for terrain Category IV in comparison to other categories. The values of wind speed decreases more rapidly as the distance from the fans increases.

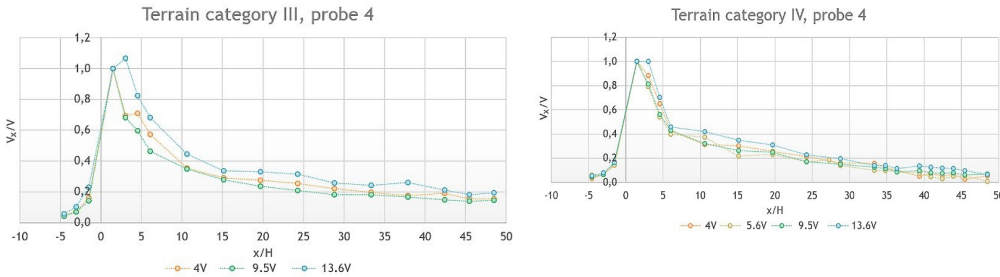

a) b)

Fig. 14. Model tests results – Series VII, comparison of air velocity for a single fan for different voltage provided to the fan for Category III (a) and IV (b) terrain roughness

The last stage of the analysis presents a comparison of a single fan with two row of fans in the context of different terrain roughness criteria (see Fig. 15.a and 15b) [27]. Analysis shows differences in the shapes of airstreams for terrain categories 0, III & IV. In the case of a single fan, the increase of terrain roughness results in a decreasing airstream velocity. However, a local increase of airstream velocity can be observed for a case of two row of fans for terrain categories III & IV (compare to category 0). This is most likely due to local flow restriction/resistance. In order to determine the local effect of flow restriction/resistance in detail, it is required to conduct more studies, in particular, smoke visualisation research.

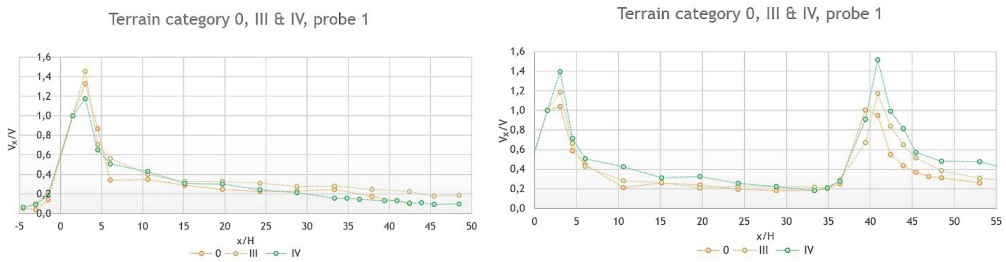

a) b)

Fig. 15. Model tests results – Series VII & VIII, comparison of air velocity for a single fan (a) and two consecutive fans placed one by one at a distance of 42.4 x/H (b) on Category III and IV terrain roughness, nominal voltage of 13.6 V

4. Results analysis and conclusions

By comparing relative velocity of airstream at a distance further than 4.6 x/H (30 cm) from the fan outlet (which is where the influence of turbulence resulting from fan rotation decreases) for different voltage supplied to the fans, it can be observed that there are no significant differences between them. This means that the influence of the Reynolds number on the phenomenon is negligible for the measured range of velocities, thus the model scale tests may translate to full scale scenarios.

Despite the change in the number of fans from 1 to 8 and the change of the scale from 1:833 to 1:100, the flow patterns of the air streams were similar. This confirms the thesis that in model tests, a group of fans cooperating close to each other can be replaced by a single fan at the smaller scale (i.e. 1:833) as was suggested by the experiments.

The range of air suction behind the fan is limited to only 1.5-3 x/H (10-20 cm). Thus, it is economically reasonable to place another fan in the place where the stream from the preceding fan fades away. This distance was established at 42.4 x/H (280 cm) in the case of one row of fans.

Placing 3 fans in a row increased the distance at which the generated airstream maintained its continuity to 56 x/H (370 cm). Comparing the spacing between fans at 1.5 D (90 mm) and 3 D (180 mm), the latter produced similar wind speeds, but covered a larger area. Thus, the spacing of 3 D (180 mm) between fans in each row was established as the default for further tests.

Adding terrain roughness to the tests only slightly diminished the wind speed of the airstream. It was determined that they kept the same continuity as with the smooth surface, which means they might be used in urban areas in the real world, where the generated airstream would be affected by the buildings [9].

This work was funded by an internal grant from the Faculty of Civil Engineering of Cracow University of Technology.

References

[1] Błażejczyk K., *System wymiany i regeneracji powietrza jako czynnik poprawy warunków aerosanitarnych i bioklimatycznych w mieście*, Eds: Degórska B., Bańcik M., *Środowisko przyrodnicze Krakowa: zasoby - ochrona - kształtowanie*, IGiGP UJ, UMK, WGiK PW, Kraków 2013, 187–190.

[2] Chu A.K.M., Kwok R.C.W., Yu K.N., *Study of pollution dispersion in urban areas using Computational Fluid Dynamics (CFD) and Geographic Information System (GIS)*, Environmental Modelling & Software, 20, 2005, 273–277.

[3] Wingstedt E.M.M., Osnes A.N, Akerwik E., Eriksson D., Pettersson Reif B.A., *Large-eddy simulation of dense gas dispersion over a simplified urban area*, Atmospheric Environment 152, 2017, 605–616.

[4] Carpentieri M., Robins EnFlo A.G., *Wind tunnel experiments of flow and dispersion in a real urban area*, The 7th International Conference on Urban Climate, 29 June – 3 July, Yokohama 2009.

[5] Buccolieri R., Sandberg M., Di Sabatino S., *City breathability and its link to pollutant concentration distribution within urban-like geometries*, Atmospheric Environment 44, 2010, 1894–1903.

[6] Ramponi R., Blocken B., de Coo L.B., Janssen W. D., *CFD simulation of outdoor ventilation of generic urban configurations with different urban densities and equal and unequal street widths*, Building and Environment 92, 2015, 152–166.

[7] Oke T.R., *Boundary layer climates*, Methuen, New York 1978.

[8] Sorbjan Z., *Turbulence and diffusion in the lower atmosphere*, PWN, Warszawa 1983.

[9] Hang J., Sandberg M., Li Y., *Effect of urban morphology on wind condition in idealized city models*, Atmospheric Environment 43, 2009, 869–878.

[10] Jiang Y., Alexander D., Jenkins H., Arthur R., Chen Q., *Natural ventilation in buildings, measurement in a wind tunnel and numerical simulation with large–eddy simulation*, Journal of Wind Engineering and Industrial Aerodynamics 91, 2003, 331–353.

[11] Omrani S., Garcia–Hansen V., Capra B., Drogemuller R., *Natural ventilation in multi–storey buildings, Design process and review of evaluation tools*, Building and Environment 116, 2017, 182–194.

[12] Yang L., Qian F., Song D.X., Zheng K.J., *Research on Urban Heat–island Effect*, Procedia Engineering 169, 2016, 11–18.

[13] Yang L., Li Y., *Thermal conditions and ventilation in an ideal city model of Hong Kong*, Energy and Buildings 43, 2011, 1139–1148.

[14] Lewińska J., *Klimat miasta. Vademecum urbanisty*, Instytut Gospodarki Przestrzennej i Komunalnej, Oddział w Krakowie, 1991.

[15] Cao Z., Wang Y., Duan M., Zhu H., *Study of the vortex principle for improving the efficiency of an exhaust ventilation system*, Energy and Buildings 142, 2017, 39–48.

[16] US 4164256 A, Cooling tower with forced ventilation and natural draft.

[17] US 5425413 A, Method to hinder the formation and to break–up overhead atmospheric inversions, enhance ground level air circulation and improve urban air quality.

[18] Spurr G., *The penetration of atmospheric inversions by hot plumes*, Journal of Meteorology, Vol. 16, 30–37, 1959.
[19] DE 3503138 A1, *Process for reducing smog by the chimney inversion/injector effect*.
[20] Blackman K., Perret L., Savory E., Piquet T., *Field and wind tunnel modelling of an idealized street canyon flow*, Atmospheric Environment 106, 2015, 139–153.
[21] Zhai Z.J., Brannon B., *Performance comparison of destratification fans for large spaces*, Procedia Engineering 146, 2016, 40–46.
[22] CN 203620447 U, Device for preventing pollution of air suspended particles in urban industrial district.
[23] Flaga A., *Kryteria podobieństwa modelowego dla równoległego układu wież wentylacyjnych*, Research Report, Wind Engineering Laboratory, Cracow University of Technology, Kraków 2017.
[24] Flaga A., Flaga Ł., Krajewski P., Pistol A., *Badania wstępne możliwości dynamicznego oddziaływania na warstwę przyziemną. Etap I – Pomiar pola prędkości przepływu i zasięgu strumienia powietrza generowanego przez modele wentylatorów/wież wentylacyjnych w różnych wariantach ich konfiguracji*, Research Report, Wind Engineering Laboratory, Cracow University of Technology, Kraków 2017.
[25] PN–EN 1991–1–4. Eurokod 1. Oddziaływania na konstrukcje. Część 1–4, Oddziaływania ogólne – Oddziaływania wiatru [in Polish].
[26] Flaga A., *Inżynieria wiatrowa. Podstawy i zastosowania*, Arkady, Warszawa 2008.
[27] Flaga A., Flaga Ł., Krajewski P., Pistol A., *Badania wstępne możliwości dynamicznego oddziaływania na warstwę przyziemną. Etap III – Badania w tunelu aerodynamicznym wybranych zagadnień z Etapów I i II przy uwzględnieniu wpływu chropowatości podłoża, zabudowy miejskiej)*, Research Report, Wind Engineering Laboratory, Cracow University of Technology, Kraków 2017.

TECHNICAL TRANSACTIONS 7/2019
CIVIL ENGINEERING
DOI: 10.4467/2353737XCT.19.073.10724
SUBMISSION OF THE FINAL VERSION: 14/06/2019

Iver Frimannslund
iver.frimannslund@nmbu.no
Thomas K. Thiis orcid.org/0000-0002-0552-356X
Department of Mathematical Sciences and Technology, Norwegian University of Life Sciences, Norway

A FEASIBILITY STUDY OF PHOTOVOLTAIC SNOW MITIGATION SYSTEMS FOR FLAT ROOFS

STUDIUM WYKONALNOŚCI FOTOWOLTAICZNYCH SYSTEMÓW OGRANICZANIA ŚNIEGU DLA DACHÓW PŁASKICH

Abstract

A new photovoltaic system combining electrical power production with snow mitigation intends to reduce the snow load on flat roofs. Applying electrical power to PV modules causes heat production on the module surface, allowing the ablation of snow. This study combines measurements and theoretical analysis to investigate which conditions are favourable for snow load reduction and discusses the system's feasibility to perform a controlled snow load reduction in a heavy snow load scenario for buildings with flat roofs. Both melting and sublimating of snow are investigated as means to reduce the load. The results show that the potential for load reduction is highly dependent upon weather conditions and snowpack characteristics during system operation. The refreezing of meltwater and water saturation of snow are identified as phenomena potentially preventing sufficient load reduction in cold conditions. Due to such temperature sensitivity, the system is likely to be more suitable for warm climates occasionally experiencing heavy snow loads than for climates with long and cold winters.

Keywords: snow, PV systems, load reduction, roofs, reliability, climate robustness

Streszczenie

Nowy system fotowoltaiczny łączący produkcję energii elektrycznej z ograniczaniem śniegu ma na celu zmniejszenie obciążenia śniegiem na dachy płaskie. Zastosowanie energii elektrycznej w modułach fotowoltaicznych powoduje wytwarzanie ciepła na powierzchni modułu, umożliwiając ablację śniegu. Niniejsze badanie łączy pomiary i analizę teoretyczną w celu zbadania, które warunki sprzyjają zmniejszeniu obciążenia śniegiem i omawia możliwości systemu w zakresie kontrolowanej redukcji obciążenia śniegiem w scenariuszu dużego obciążenia śniegiem dla budynków z płaskimi dachami. Zarówno topienie, jak i sublimacja śniegu są badane jako sposób na zmniejszenie obciążenia. Wyniki pokazują, że potencjał zmniejszenia obciążenia zależy w dużym stopniu od warunków pogodowych i charakterystyki śniegu podczas pracy systemu. Ponowne zamoczenie wody morskiej i nasycenie wody śniegiem są identyfikowane jako zjawiska potencjalnie uniemożliwiające wystarczające zmniejszenie obciążenia w niskich temperaturach. Ze względu na taką wrażliwość na temperaturę system może być bardziej odpowiedni do ciepłych klimatów, czasami doświadczając większych obciążeń śniegiem niż w klimatach o długich i zimnych zimach.

Słowa kluczowe: śnieg, systemy PV, redukcja obciążenia, dachy, niezawodność, odporność na klimat

1. Introduction

Due to climate change and the continuous updating of design standards, parts of the existing building stock are not well adapted to the environment in terms of reliability. Increased knowledge of the environmental loads imposed on buildings is the driving force for updating standards to better represent the actual loads occurring. The development of standards has led to many existing buildings being regarded as under-designed in the current design regulations. The temporal change of the ground snow load in Norway is an example which illustrates how increased knowledge influences our design standards. Meløysund et al. [17] describes how the ground snow load has developed from a general load with little variation, to a load varying with the local topography and the local climate. This is exemplified through the development of the ground snow load in Norway, which has evolved from being 1.5 kN/m^2 for the whole country in 1949 to ranging from 1.5–9.0 kN/m^2 in the current national annex [23]. The differentiation of the snow load results in many existing buildings being regarded as under-designed in the current regulations. Meløysund [16] states that 4.5 % of the total bulk of buildings in Norway may have too low a capacity according to current regulations.

In addition to the under-design of the existing building stock, a change in the environmental loads is expected due to climate change [3, 14, 21, 24, 25]. The global trend of climate change is that we will have increased winter temperature and winter precipitation. The increase in temperature will determine whether the precipitation falls as rain or snow, and will influence the change in the snow load [21]. For this reason, the snow cover in climates with mild winters should be more sensitive to an increase in temperature than climates with colder winters [15]. However, it is the case that even if the increased temperature leads to more precipitation falling as rain, it will not necessarily lead to a reduction of the snow load. This is due to the effect of snow absorbing the rain and increasing the load as a consequence [25]. Although it is predicted as a global trend that snow cover will reduce [11], several studies show that snowfall is expected to increase in cold areas [13, 22]. Croce [3] states that the sensitivity of snow cover to precipitation and temperature is highly related to topographic features such as the elevation aspect and terrain shading. On this basis, it is reasonable to assume that the change in snow load should be estimated on a regional scale. A report on the expected change in the characteristic ground snow load for Norway in the period 2071-2100 predicts that the snow load will be reduced for most municipalities, but thirty-four municipalities expect a significant increase in the load [14]. The authors of the report recommend that the characteristic snow load for the thirty-four municipalities should be increased.

The historical updating of standards due to increased knowledge of environmental loads together with the expected change in climate signifies a future discrepancy. Buildings are designed with a long life cycle of 50-100 years and are likely to experience a different environmental impact than what they are designed for.

If a building is under-designed with respect to snow load, there are certain measures which could be performed in order to increase the reliability of the structure. Structural health monitoring (SHM) can be performed at an early stage to determine the state of the

building and provide a basis for further improvements [4]. Retrofitting through upgrading the structural capacity of the building is a permanent measure, but often proves costly for the building owners. Manually removing snow off the roof is a measure which can be performed in the case of heavy snow loads, but relies on knowledge of the snow load on the roof and on having the available labour to remove the snow at the right time. Shovelling snow off roofs is also highly correlated with accidents [2, 12].

Buildings that are under-designed with respect to snow load are often prevented from having PV systems on the roof surface due to the additional weight. Roofs are especially suitable for having PV systems in urban environments due to them being large flat surfaces with high solar irradiation, favourable wind conditions and accessible for maintenance. Roof surfaces are often unutilised, even in densely populated areas.

2. Photovoltaic snow mitigation systems

Photovoltaic snow mitigation systems combine electrical power production with snow removal. If PV-cells are subjected to forward bias, heat is produced due to the electric resistance in the cells. The heat development on the surface of the PV-cell enables the ablation of snow and presents a new application for PV-systems. The photovoltaic snow mitigation system can serve the following three possible purposes:

- as a measure for under-designed roofs to increase snow load robustness,
- releasing roof area for PV-purposes previously indisposed due to limited load capacity,
- increasing yield of PV-systems through melting snow when the typical seasonal snowpack is present.

This study focuses on the first two purposes described above. The latter purpose has previously been briefly researched by Frimannslund [7] and more thoroughly by Aarseth et al. [1].

If the intent of the system is to reduce snow loads on flat roofs; the snow should be kept on the modules. Snow load reduction on flat roofs relies on melting the snowpack from the bottom up, and requires modules with a low angle tilt due to the sliding of snow. For increasing yield through removing snow from the modules, a tilt could be beneficial because sliding snow off the modules requires less energy than melting the entire snowpack.

Applying heat to the bottom of the snowpack will gradually increase the temperature of the snow towards 0°C. A thick snowpack reduces heat loss to the ambient environment, enabling a steady increase in temperature and a gradual melting process on the module surface. For load reduction to be effective, meltwater must be transported off the roof.

Sublimation, the instant transition from solid to vapour, can serve as another means of load reduction when melting is difficult. Sublimation occurs naturally in snow when there is a higher partial pressure of water vapour in the snowpack than in the air. The difference creates a gradient in specific humidity, causing transportation of mass from the snowpack to the air. The natural process of sublimation in the snow can simply be amplified by applying power to the modules when the conditions are right. A formula calculating latent heat flux due to sublimation illustrates the factors influencing the process:

$$Q_{BF} = \rho L_s C_E u_a \left(q_s - q_a\right) \quad (1)$$

where is the air density, is the latent heat of sublimation, is a transfer coefficient of latent heat, is the wind speed, is the specific humidity of the snow and is the specific humidity of the air. In order to induce the sublimation of snow on the PV-surface, the temperature should be close to, but never above, 0°C. Sublimation also occurs above freezing; however, this results in additional melting and necessary transportation of the meltwater. By keeping the temperature of the module close to zero, the partial pressure of water vapour in the snow increases, creating a vapour gradient and transportation of mass from the snow to the air. Sublimating snow is nevertheless far more energy consuming than melting snow. The energy required for sublimating snow at 0°C is equal to the combined energy it takes to melt and vaporise snow at 0°C [19]. The amount of energy required to induce a phase change in water is given by the latent heat constants presented in Table 1.

Table 1. Latent heat constant for phase changes in water [19, 27]

Phase change	Temperature	Latent heat constant [kJ/kg]
fusion	0°C	333.5
vaporisation	100°C	2257.0
sublimation	0°C	2830.0

The latent heat constant for sublimation is approximately 8.5 times higher than the latent heat constant for fusion. This means that it takes 8.5 times as much energy to sublimate water as it takes to melt it at 0 °C. Another way to put it is that you will have 8.5 times less ablation when sublimating compared to melting for the same energy input.

Applying forward bias to PV modules is a common way of checking the quality of the modules for defects in the manufacturing process. This is achieved with a limited electrical effect and is possible for any module regardless of the manufacturer. However, the degradation effects of applying forward bias to PV-modules over a long term is poorly documented.

In order to apply forward bias to PV-systems, rectifiers converting AC-current from the grid to DC-current are necessary. Alternatively, DC-current can be applied directly from batteries. PV modules are commonly designed with bypass diodes to only let the current pass one way, due to the unwanted effect of reverse bias. DC current must therefore be applied in the same direction as when producing power. Rectifiers are in principle the only additional component a normal PV-system needs to induce heat production on the module surface and use it for snow mitigation purposes.

In order for the photovoltaic snow mitigation system to become a widespread solution for under-designed roofs, it must be included in the framework of the international standards for structural design. The ISO standard for the determination of snow loads on roofs [10] provides a framework for reducing the design snow load based on a reliable control device or method able to reduce the snow load. The framework is presented in Annex F, entitled *Snow loads on roof with snow control*. To be able to reduce the designed snow load, the respective system's abilities for reducing the snow load for a given evaluation period must be documented.

3. Material and methods

3.1. Site description

Photovoltaic snow mitigation systems are a relatively recent invention and only a few buildings are equipped with such systems. One of the first buildings with a photovoltaic snow mitigation system installed on a flat roof was a warehouse building in Oslo, Norway. The system was designed by Innos AS and is called Weight Watcher [8]. The roof with the installed PV system is shown in Fig. 1. The system monitors the snow load imposed on modules through load sensors installed on the module rack. When the load reaches a certain limit, power is applied to the PV system and melting is initiated. The system was used for tests in this study, including a snow load reduction test and an aerial thermography of the system being applied forward bias.

The roof has a surface of approximately 1980 m^2 and is designed for a characteristic snow load of 1.5 kN/m^2. The PV system on the roof consists of 720 modules, orientated 66°/246° (East-North-East, West-South-West), each row facing the opposite direction of the previous row. The modules are tilted at an angle of 10°.

A customised drainage system is installed on the roof, designed for transporting meltwater off the roof surface. The drainage system is made of gutters between the rows of modules as

Fig. 1. The Weight Watcher system installed at the warehouse

illustrated in Fig. 1. Each gutter drains water from two rows and is heated in order to prevent the refreezing of meltwater. The gutters lead to the edge of the roof where water is disposed through scuppers.

3.2. Aerial thermography of a photovoltaic snow mitigation system

Thermography of the PV-system applied forward bias at the warehouse in Oslo was performed using a customised unmanned aerial vehicle with an infrared camera. The intent was to document the temperature distribution across the system and the location of possible hot spots and defects. The thermography was performed without an existing snow cover on the roof. Two maps were made showing the temperatures on the roof when half of the PV-system has forward bias applied. The maps were made by taking many single overlapping infrared images of the roof from heights of 50 and 30 meters. An infrared 3D-model was made by combining individual, infrared images using photogrammetric software for drone-based mapping [20]. The 3D model was then projected into the horizontal plane, creating 2D maps. The maps were calibrated for emissivity and atmospheric radiation [7, pp. 60-61] using FLIR Tools [6]. Calibration points were created on the roof surface, which was necessary to characterise individual modules on the uniform PV-system and to create the infrared 3D model.

3.3. Load reduction test of a full-scale photovoltaic snow mitigation system

A load reduction test of the full-scale facility at the warehouse was performed in February 2017. The objective was to test the performance of the snow mitigation system and to investigate the drainage system. The average snow depth on the day of testing was approximately 5 cm, which was too low to create a continuous snow cover across the modules, thus leaving the panels exposed to the wind. Due to the thin snowpack, the test cannot be said to be a true load reduction test. Load reduction is not usually necessary for snow loads less than the design snow load, which equals 75 cm of snow with an average density of 200 kg/m^3 for the warehouse roof. The test was performed not to reduce the load itself, but with the intent of documenting the physical process occurring when melting snow with PV-modules. The weather conditions on the day of the testing was partly cloudy with a temperature of -7 °C and an average wind speed of 6 m/s. The wind blew perpendicular to the rows of modules, from East-North-East. Three strings of modules were applied power for a duration of 2:00 hours. Temperature and humidity levels on the module surface and in the ambient environment were logged through the test.

3.4. Case study with single modules

In addition to testing the photovoltaic snow mitigation system at the warehouse in Oslo, a case study investigating different possible snow load reduction scenarios was performed. The purpose was to investigate the snow metamorphism occurring on the modules when applying forward bias of different intensities under varying climatic conditions. With three PV-modules, two rectifiers and the required cables, a system was setup in Nordmarka, Norway.

Fig. 2. Setup for the case study – the module to the left is a reference module, while the two to the right are active modules connected to rectifiers able to apply forward bias

Three different snow load reduction scenarios were performed:

- melting old, wet snow in ambient temperatures above freezing,
- melting fresh snow in cold conditions,
- sublimating snow in cold conditions.

The two melting cases were performed with a relatively high effect of 268.8 W/m^2 for the first case, and 762.5 W/m^2 for the second case. Both cases were conducted over the course of 3.5 hours each. Here, snow was shovelled onto the modules. The sublimation case was performed after a fresh snowfall of 14 cm. This case was conducted over a time span of 58 hours with an average effect of 29.8 W/m^2. The average air temperature was -9.3°C and the average humidity was 86.3%. The temperature of the modules was adjusted to be as close to zero as possible, without ever exceeding this limit. For all cases, temperature and humidity was logged in the top and bottom of the snowpack for both the unheated reference module and for the active modules. Ambient temperature and humidity was also logged. Load reduction was calculated using depth and density measurements both before and after applying forward bias.

4. Results

4.1. Aerial thermography of a photovoltaic snow mitigation system

The temperature maps were produced using aerial thermography of the photovoltaic snow mitigation system being applied forward bias. The thermography was conducted at the warehouse in Oslo when no snow was present. The first map provides an overview of the system with its surroundings.

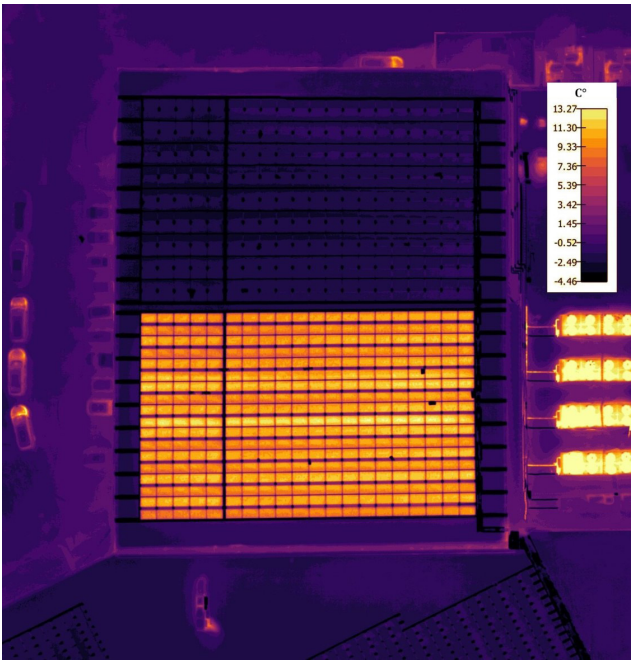

Fig. 3. Temperature map of the photovoltaic snow mitigation system; half of the system has forward bias applied

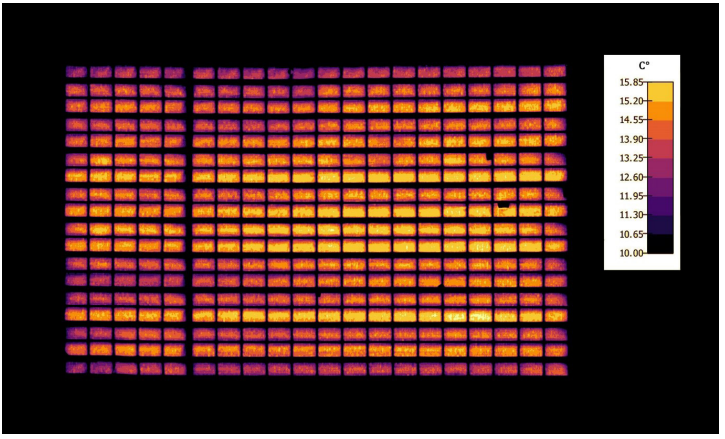

Fig. 4. Temperature map highlighting detail of the photovoltaic snow mitigation system with forward bias applied

The temperature map is created from 79 single images taken from a height of 50 m. The temperature scale is set to a wide range which includes the temperature of the surroundings. The map comprises surrounding objects such as recently used cars, smaller buildings at ground level, and the cooling system that is clearly running to the right on the map. The black dots at the modules are calibration points as described in Section 3.2.

The second map excludes the surroundings and amplifies the details of the modules emitting heat.

The temperature map is created from 68 single images taken from a height of 30 m above the roof. The temperature scale is set to a narrow range, amplifying the details and excluding the surroundings. In addition to the small temperature differences on the modules, there appears to be a pattern of equal temperatures in the strings of modules. Modules on the same string have similar temperatures, from one end to the other. The highest measured temperature on the PV-system was 15.85°C, while the temperature of the air was approximately -4.7°C [18].

4.2. Load reduction test of a full-scale photovoltaic snow mitigation system

Shortly after applying forward bias to the three strings, the temperature increased on the module surface. For the East-North-East rows facing the wind, the snow melted on the module surface only to be refrozen on the rim of the frame. An ice cap was created over the module, as shown in Fig. 5. Underneath the ice cap, there was liquid water, encapsulated by the module and the ice. The meltwater did not reach the heated gutters directly beneath the modules, and there was no significant load reduction. The refreezing of meltwater did not occur for the rows facing West-South-West, which were sheltered from the wind.

Fig. 5. An ice cap formed on the lower edge of the modules that were facing the wind. The heated gutter can be seen under the module, stretching towards the edge of the roof

4.3. Case study with single modules

The first case involved melting old wet snow in ambient temperatures above freezing. When forward bias was applied to the modules, the snow melted on the module surface and created a small layer of water-saturated snow on the module surface. The water drained

efficiently despite the module not having a significant tilt. In the second case, the layer of snow on the modules was from a recent snowfall and had the light, fine structure that fresh snow often has. The temperature was below 0°C when the experiment was conducted. In this case, snow melted on the module surface and a significant amount of meltwater was sucked into the capillary pores of the dry snow. At the end of this test, a 5-cm-thick layer of slush was observed at the bottom of the module as shown in Fig. 6.

Fig. 6. A 5 cm slush layer was observed at the bottom of the snowpack at the end of the second melting test

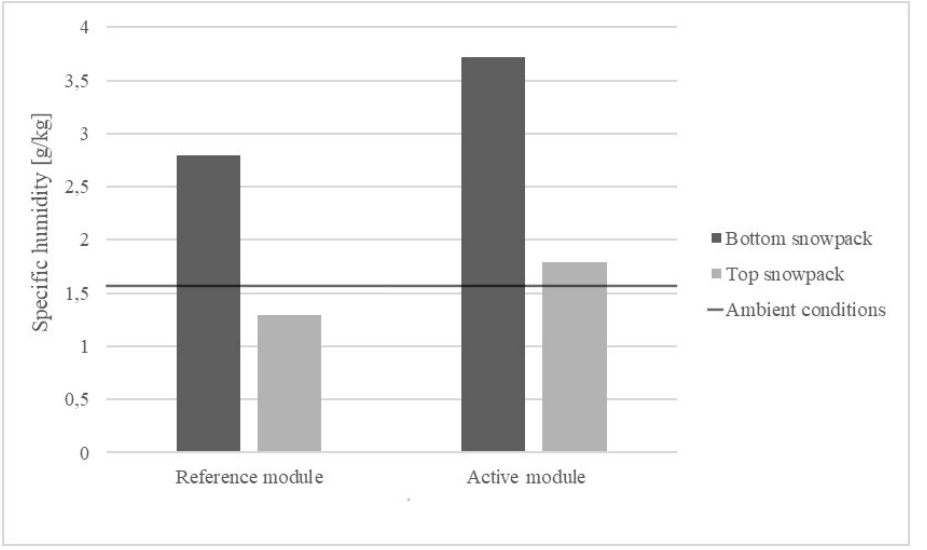

Fig. 7. Graph showing the average logged specific humidity of the reference and active module at the top and bottom of the snowpack in relation to the ambient conditions

The third case involved sublimating snow in cold conditions. At the end of the test, a clear dent in the snowpack was visible on the active modules, indicating a change in the snowpack. The temperature and humidity loggers document the change in specific humidity for the active and reference modules providing information indicative of the change in mass. Figure 7 illustrates the average specific humidity at the top and bottom of the snowpack based on the logged temperature and humidity.

The temperature and humidity loggers shows an increase in temperature on the module surface towards 0°C when forward bias is applied, and a corresponding increase in humidity in the snowpack. The partial pressure of vapour was highest at the bottom of the snowpack where heat was applied, and decreased towards the top of the snowpack. The partial pressure of water vapour for the modules applied forward bias was generally higher at the top of the snowpack than in the air, implying the transport of moisture from the snowpack to the air. For the reference module, the partial pressure of water vapour was higher for the air than the top of the snowpack, indicating condensation. This corresponds with measured changes in weight where the active module lost weight and the reference module gained a small amount of weight. The weight reduction was calculated by comparing the density and the snow depth measurements before and after the test. The average weight reduction for the active module was measured at 0.86 kg/m^2 per day. The total energy applied to the modules was 2299.2 kJ per kg of sublimated snow. At the end of the experiment, an ice sheet was uncovered on the surface of the active modules, although the loggers show that temperatures did not exceed zero. The ice sheet was thin and porous and covered the entire module surface.

5. Discussion

The results from the experiments highlight the importance and possible difficulties of transporting meltwater away from the roof due the risk of refreezing and water saturation of the snow. This is illustrated in the load reduction test at the warehouse, which resulted in meltwater freezing directly at the module. The refreezing of meltwater obviously contributes to insufficient load reduction, but it can also cause an unfavourable redistribution of load if water accumulates on the roof surface before refreezing.

However, the test at the warehouse is not entirely representative of a real snow load reduction scenario. Melting with the intent of reducing the snow load is only required for larger snow depths imposing a high load. The insulating effect of snow will increase the temperature on the module surface and will also provide shelter from the wind. Melting snow in cold conditions is therefore likely to be more easily performed for thick than for thin snowpacks.

The case study with single modules showed that the snow's capacity for being saturated with water is highly dependent on the microstructure of the snow, and is an important factor for the drainage conditions on the roof. The snow's ability to suck up meltwater on the module and roof surface inhibits the drainage of water and the subsequent load reduction. A slush layer on the module or roof surface will continue to delay the drainage until the snow is fully saturated and cannot hold more water. The case study showed that if the snow is fresh and

dry, it has a larger buffer capacity for holding water than older and more grainy snow. Draining meltwater from old and grainy snow, typically present in spring, is therefore likely to be less problematic than for snow with a fine microstructure that is typical of mid-winter conditions. Water saturation of the snow also increases the consequence for freezing of meltwater if the weather conditions change. If such a slush layer was to freeze, it could result in an ice sheet on the roof surface, further preventing drainage.

Poorly insulated roofs are subject to significant heat loss through the roof surface, increasing the temperature under a thick snowpack, favourable for drainage with respect to the refreezing of meltwater and the water saturation of snow. For roofs with significant insulation, heated gutters are recommended to improve the drainage conditions. Either way, a heat supply preventing the refreezing of meltwater in an unobstructed pitched flow path is crucial for the transportation of meltwater away from the roof when melting snow in cold conditions.

A phenomenon involving the formation of snow bridges over the PV-modules as melting is initiated was not observed in the load reduction tests, but it is a common occurrence in applications involving the melting of snow with heat cables in, for example, gutters and drains. If snow is melted from the PV-surface and the snow cover above does not collapse as the snow is melted away, a cavity can form between the PV-surface and the snow, forming a bridge of snow over the modules. The formation of such snow bridges can be reinforced by evaporating water from the roof or PV-surface condensation and freezing onto the snow. A cavity might also result in enhanced air infiltration, increasing the risk of freezing melt water. Such a phenomenon is dependent upon snowpack characteristics, weather conditions and the density of PV-modules on the roof surface.

As cold conditions can cause phenomena preventing the drainage of melt water; as revealed in the load reduction tests, the system is likely to be more suitable for warm climates occasionally experiencing heavy snow loads than for climates with long and cold winters.

The test of load reduction through sublimation indicates the potential for drainage free snow mitigation. Sublimation is conducive under cold and windy conditions, which is typically when melting is unfavourable. An amount of 0.86 kg/m^2 per day was sublimated in the case study with single modules. Although this is not much compared to the loads posing danger to roofs, the method can be improved with further knowledge of the phenomena and better control of the system, potentially resulting in more effective load reduction. Sublimation occurs naturally in snow and applying low magnitude forward bias to modules can simply amplify the sublimation if the conditions are right. This enables load reduction through cooperation with the ambient forces of nature. The amount of energy used for sublimation in the case study was calculated to be 19% lower than the latent heat of sublimation presented in Table 1, indicating a contribution of the ambient conditions. The ice sheet uncovered at the end of the experiment raises the question of whether induced sublimation on PV-modules is possible in the long term. The ice sheet indicates some sort of snow metamorphism which may prevent further load reduction. The sublimated snowpack was of a relatively shallow depth, contributing to a steep vapour pressure gradient between the snow and the air. A thicker snowpack results in a more gentle gradient and it is possible that the snow will be sublimated on the module surface only to be deposited further up in

the snowpack, never reaching the outside air. The question of whether it is possible to reduce the load by induced sublimation for thicker snow packs with photovoltaic snow mitigation systems has been poorly documented and should be further researched.

The results from the aerial thermography of the PV system with forward bias applied show that the relative temperature differences between modules and strings are of low magnitude. Temperature differences between string and modules do occur, but the relative temperature differences do not indicate any deficiencies in the system. Although highly dependent on the resolution of the map, typical infrared patterns from defects [9, 26] cannot be observed in the pictures, indicating a well-functioning system.

Reducing the snow load on under-designed roofs by applying electrical power to PV systems raises the question of how much energy is required to keep the roof safe, and whether the system is a sustainable and cost efficient solution to increase snow load robustness. The amount of energy required to keep the roof safe depends on the amount of energy used in a single load reduction, and how often it is necessary to reduce the load. The frequency of load reduction depends on what the building is designed for, hence the magnitude of under-design. The magnitude of the snow load imposed on buildings varies from one year to another, making load reduction unnecessary every year. This is one of the reasons why it is not necessary, with respect to safety, to melt the snow away as it accumulates. The long--term energy balance of reducing load and producing energy is little researched and should be investigated further. The potential for increasing the yield of PV systems through melting snow during the seasonal snowpack should be taken into account in this evaluation.

Photovoltaic snow mitigation systems are designed with the intent of reducing the snow load on flat roofs, but installing PV systems on roofs changes how snow accumulates and is distributed on the roof surface. In the design standards, different roof shapes have different shape factors determining the distribution of snow on the roof due to wind erosion and the sliding of snow [10]. A shape factor for PV systems on flat roofs is nevertheless still premature for most design standards. Research indicates that PV systems influence the friction velocity on the roof important for snow erosion, depending on the angle, height and distance between the rows of the panels [5]. The layout of the system, in combination with the prevailing wind direction on the site, can potentially result in an inhomogeneous snow load distribution compared to flat roofs without PV systems. In addition to this, having PV systems on flat roofs results in a bulk of snow laying on the module surface rather than on the surface of the roof itself. This decreases the effect of melting snow due to heat loss through the roof and increases the snow load compared to roofs without PV systems. This is especially significant for poorly insulated roofs. How PV systems change the distribution and magnitude of snow loads on flat roofs should be taken into account when assessing PV snow mitigation systems as a measure of increasing robustness to snow loads. Hopefully, future design standards will provide accurate calculation methods for how PV systems affect the snow load on roofs.

As mentioned in Section 2, Annex F in ISO 4355 presents a framework enabling a reduction in the design snow load for a reliable control device or method which slide or melt snow [10]. In order for the design snow load to be reduced, documentation guaranteeing load reduction must be provided. Such documentation is highly dependent

on the climate where load reduction is performed. The results from this study uncover phenomena important for snow load reduction that are applicable to similar climates. However, areas with very long and cold winters might experience additional problems that are not documented in this study. In general, it is necessary to conduct further studies of load reduction under varying climatic conditions before it can be used as a geographically widespread solution for snow load reduction.

Implementing a photovoltaic snow mitigation system on an under-designed roof and being dependent on a controlled snow load reduction severely influences the reliability of the roof. Building reliability is calculated to satisfy a predefined reliability level in the design standard, corresponding to the consequence of building failure. The variables used for dimensioning the structural components (e.g. resistance variables, permanent actions and climatic loads) have a certain statistical probability for occurring. When a PV snow mitigation system is installed on a roof, the dead load on the roof increases and the dependence of the controlled snow load reduction is added. The snow mitigation system itself has a certain probability for providing sufficient load reduction in a heavy snow load scenario, which must be taken into account in the reliability calculation. The probability of sufficiently reducing the load depends on the temporal efficiency of load reduction, and possible events interrupting the reduction (technical malfunctions, power outages, climatic conditions). Such risk factors must be identified and implemented in a reliability model for the structural safety of the building before the system can become a widespread solution for under-designed roofs.

6. Conclusion

The state of the existing building stock and the expected change in the future climate calls for new measures for under-designed roofs. Photovoltaic snow mitigation systems combine power production with snow removal by applying forward bias to the system. The results from this study show that reducing the snow load on flat roofs with photovoltaic snow mitigation systems is possible. The feasibility of load reduction is, however, highly dependent on the climatic conditions during system operation. The possible refreezing of meltwater and water saturation of snow are possible outcomes which can prevent sufficient load reduction and possibly result in an unfavourable load distribution. Melting in ambient temperatures above freezing is less problematic with respect to drainage of meltwater and it is naturally less energy consuming than melting in cold conditions. Melting a thicker snowpack in cold conditions is yet to be tested on a full-scale PV system. Reducing the snow load in ambient temperatures above freezing is therefore likely to be effective, while melting in cold conditions provides more risk due to the possible refreezing of meltwater and the water saturation of snow. For this reason, the system is likely to be more suitable for warm climates occasionally experiencing heavy snow loads, than for climates with long and cold winters. Tests of load reduction through sublimation indicates a potential new strategy for snow removal when conditions are cold and windy, typically unfavourable for melting. It is, however, unknown whether load reduction through induced sublimation is possible for thicker snow packs and

if it will function in the long term due to the metamorphism of snow at the bottom of the snowpack. The load reduction tests nonetheless highlight the importance of cooperating with the weather conditions to perform sufficient and energy-efficient snow removal. Before the photovoltaic snow mitigation system can become a widespread solution for under-designed roofs, it is crucial to investigate the long-term effect of applying forward bias to PV modules and provide documentation for the system's load reduction capabilities to be used in structural design standards. In addition to this, the long-term energy balance of reducing snow loads and producing energy should be researched in order to determine the system's sustainability as a measure to increase snow load robustness.

Our appreciation to Tommy Strömberg at Innos AS for welcoming us to research the Weight-Watcher system and for providing equipment for scientific measurements.

References

[1] Aarseth B.B., Øgaard M.B., Zhu J., Strömberg T., Tsanakas J.A., Selj J.H., Marstein E.S., *Mitigating Snow on Rooftop PV Systems for Higher Energy Yield and Safer Roofs*, presented at EU PVSEC 2018: 35th European Photovoltaic Solar Energy Conference and Exhibition, Brusells 2018.

[2] Bylund P.-O., Johansson J., Albertsson P., *Injuries sustained during snow removal from roofs resulting in hospital care*, International journal of injury control and safety promotion, Vol. 23, 2016, 105–109.

[3] Croce P., Formichi P., Landi F., Mercogliano P., Bucchignani E., Dosio A., Dimova S., *The snow load in Europe and the climate change*, Climate Risk Management, Vol. 20, 2018, 138–154.

[4] Diamantidis D., Sykora M., Lenzi D., *Optimising Monitoring: Standards, Reliability Basis and Application to Assessment of Roof Snow Load Risks*, Structural Engineering International, Vol 28(3), 2018, 269–279.

[5] Ferreira A., Thiis T.A., Freire N., *Experimental and computational study on the surface friction coefficient on a flat roof with solar panels*, Proceedings of the 14th International Conference on Wind Engineering, Vol. 12, 2015.

[6] FLIR, http://www.flir.eu/home (accessed: 01.02.2017).

[7] Frimannslund I., *Measurements and analysis of snow load reduction on flat roofs using a photovoltaic system in heating mode*, in *Department of Mathematical Sciences and Technology*, Norwegian University of Life Sciences, 2017, p. 157.

[8] Innos AS, www.innos.no (accessed: 18.10.18).

[9] International Electrotechnical Commission, IEC 62446. Grid connected photovoltaic systems – Minimum requirements for system documentation, commissioning tests and inspection, 2009.

[10] International Organization for Standarization, ISO 4355 Bases for design of structures, Determination of snow loads on roofs, 2013.

[11] IPCC, *Climate Change 2013: The Physical Science Basis. Report by WG1AR5*, 2013.
[12] Kamimura S., *Risk analysis on snow-related casualty cases in Niigata Prefecture, Japan*, presented at Snow Engineering V: Proceedings of the Fifth International Conference on Snow Engineering, 5–8 July, Davos, Switzerland, 2004, CRC Press.
[13] Krasting J.P., Broccoli A.J., Dixon K.W., Lanzante J.R., *Future Changes in Northern Hemisphere Snowfall*, Journal of Climate, Vol 26(20), 2013, 7813–7828.
[14] Kvande T., Tajet H.T.T., Hygen H.O., *Klima- og sårbarhetsanalyse for bygninger i Norge – Snølast og våt vinternedbør*, SINTEF Byggforsk, 2013, p. 44.
[15] Lemke P., Ren J., Alley R.B., Allison I., Carrasco J., Flato G., Fujii Y., Kaser G., Mote P., Thomas R.H., et al., *Observations: Changes in Snow, Ice and Frozen Ground*, 2007, 337–383.
[16] Meløysund V., *Prediction of local snow loads on roofs*, in *Department of Structural Engineering*, Norwegian University of Science and Technology, Trondheim 2010, p. 42.
[17] Meløysund V., Karl V.H., Bernt L., Lisø K.R., *Economical effects of differentiated roof snow loads*, [in:] *Proc. of the 6th International Conference on Snow Engineering*, Engineering Conference International, New York 2008.
[18] Meteorologisk Institutt, www.eklima.no (accessed: 24.10.18).
[19] Oke T.R., *Boundary layer climates*, Second edition, Routledge, London 1987, p. 460.
[20] Pix4D, https://pix4d.com (accessed: 30.10.2016).
[21] Räisänen J., *Warmer climate: less or more snow?*, Climate Dynamics, Vol. 30(2), 2008, 307–319.
[22] Räisänen J., Eklund J., *21st Century changes in snow climate in Northern Europe: a high-resolution view from ENSEMBLES regional climate models*, Climate Dynamics, Vol. 38(11), 2012, 2575–2591.
[23] Standard Norge, NS-EN 1991-1-3:2003+NA:2008.
[24] Steenberg R.D.J.M., Geurts C.P.W., Bentum C.A., *Climate change and its impact on structural safety*, Heron, Vol. 54(1), 2009, 3–35.
[25] Strasser U., *Snow loads in a changing climate: new risks?*, Natural hazards and Earth System Science, Vol. 8(1), 2008, 1–8.
[26] Testo, *Practical Guide, Solar Panel Thermography*, New Jersey 2014, p. 19.
[27] Tipler P.A., Mosca G., *Physics For Scientists and Engineers*, 6th ed. W.H. Freeman and Company, New York 2008.

If you want to quote this article, its proper bibliographic entry is as follow: Frimannslund I., Thiis T. K., *A feasibility study of photovoltaic snow mitigation systems for flat roofs*, Technical Transactions, Vol. 7/2019, pp. 85–100.

TECHNICAL TRANSACTIONS 7/2019
CIVIL ENGINEERING
DOI: 10.4467/2353737XCT.19.074.10725
SUBMISSION OF THE FINAL VERSION: 4/06/2019

Alicja Kowalska-Koczwara orcid.org/0000-0001-8088-7729
akowalska@pk.edu.pl
Krzysztof Stypuła orcid.org/0000-0001-8679-526X
kstypula@pk.edu.pl
Institute of Structural Mechanics, Cracow University of Technology

New Polish guidelines regarding human exposure to vibrations in buildings

Nowe polskie wytyczne dotyczące narażenia ludzi na wibracje w budynkach

Abstract

Following global trends, Polish regulations on human exposure to vibration in buildings were changed and new Polish guidelines were published in June 2017. In accordance with international trends, two methods of assessment have been added to the regulations: basic RMS method and ad-ditional VDV method. For more clarity of RMS method, the human vibration perceptivity ratio (HVPR) was introduced to new Polish regulations. In the appendix to the Polish standard, the vi-bration dose value (VDV) method is presented. The third important change in the new version of the Polish standard is measurement equipment that should be used for human perception evaluation. New regulations have precisely described what kind of equipment should be used for low-frequency recording and a new measurement disc for the human perception of vibration on floors has been introduced to the Polish standard.

Keywords: human exposure to vibration, standard regulations, RMS method, VDV, measurements

Streszczenie

Podążając za światowymi trendami, polskie przepisy dotyczące narażenia ludzi na wibracje w budynkach zostały zmienione, a nowe polskie wytyczne zostały opublikowane w czerwcu 2017 r. Zgodnie z międzynarodowymi trendami w przepisach ujęto dwie metody ewaluacji: podstawową metodę RMS i dodatkową metodę VDV. Dla większej przejrzystości metody RMS do nowych polskich przepisów wprowadzono Wskaźnik Odczuwalności Drgań przez Ludzi (WODL). W załączniku do polskiej normy przedstawiono metodę dawki drgań (VDV). Trzecią ważną zmianą w nowej wersji polskiej normy jest sprzęt pomiarowy, który należy wykorzystać w pomiarach oceny odczuwalności drgań człowieka. Nowe przepisy precyzyjnie opisały, jakiego rodzaju sprzęt powinien być używany do rejestracji niskich częstotliwości, do polskiej normy wprowadzono także nowy dysk pomiarowy służący do pomiaru wpływu drgań na ludzi w budynkach.

Słowa kluczowe: narażenie ludzi na drgania, przepisy normowe, metoda RMS, VDV, pomiary

1. Introduction

There are many sources of vibration in the vicinity of buildings in urban areas that can have an influence on building structure but can also be annoying for residents. In the diagnosis and design of the building, such influences should be taken into account. In urban areas, traffic vibrations from roadways [15], tramways [11], railways [13] are the basic excitation. In high-rise buildings located in the urban areas of many countries, wind-induced vibrations could have a significant influence on the structures [10]. In the Silesian region of Poland, mining excitation also occurs [20]. Irrespective of the source of excitation, vibrations in buildings could be annoying for residents. International standards relating to the human response to building vibrations include limits on the levels of ground-born vibrations transmitted through subsoil to buildings. All of the reviewed national standards base the limits for acceptable vibration on indoor vibration levels. This means that vibration measurements must be performed inside the building in the room in which occupants are. Conducting in-situ measurements can be problematic due to the requirement to gain the consent of owners to access the property. Most national standards are stated in terms of either the average or the maximum passive vibration level; rarely are adjustments included to account for the number and duration of vibration events. One exception is British Standard [4], which states a criterion based on total vibration exposure. In the newest version of British Standard [3], the total time of exposure is also be taken into account. In the nineteen-eighties, when the most recognisable and widely used ISO [6, 7] standards were published, some new trends in the context of human exposure to vibration in buildings were investigated. The frequency range in which the evaluation of human exposure to vibration is mostly considered in national standards is in the range of 1 to 80 Hz. In Japan, where many very tall pencil-like buildings with small transverse dimensions are often found, the evaluation of human exposure to vibrations starts at frequencies below 1 Hz, [1]. Additionally, one ISO standard, [8], considers frequencies from 0.1 to 1 Hz. National and international standards differ from each other in the weighting curves which are used to determine the threshold of human perception of vibration. Weighting functions were determined according to laboratory tests. In the provisions of ISO [6] and British [3] standards, there are small differences in weighting functions in the vertical direction (z). They differ in frequencies below 5 Hz and in frequencies higher than 25 Hz. For the most unpleasant frequencies for the human body (5–25 Hz), the weighting functions are the same in both standards. The most problematic is the ISO [7] standard in which the combined weighting function (*Wm*) is applied when the position of the human body during the measurement is unknown. The differences between the three weighting functions present in the [6, 7 and 3] standards are shown in Fig. 1.

In [12] authors took four weighting functions (*Wb*, *Wk*, *Wg*, and *Wm*) into account in their *VDV* analysis. The *Wg* function is the weighting curve for the horizontal directions. The *Wb* and *Wk* were found to be more applicable than *Wg* and *Wm* with regard to explaining the perception of floor vibration.

Duration of vibration is the main problem in standards because in most of them, the duration of vibration is not clearly described. Of course, in each of the considered standards, there is

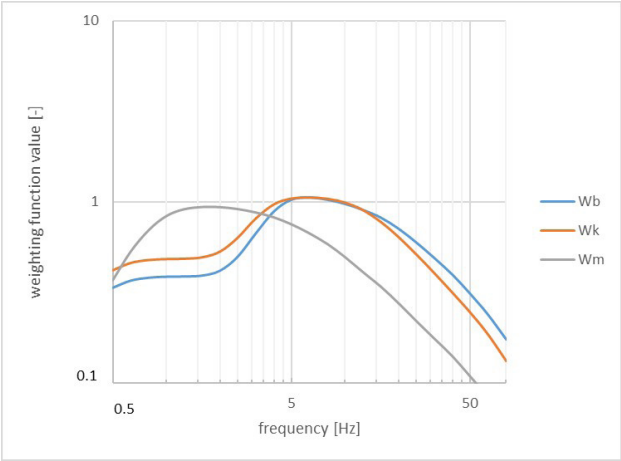

Fig. 1. Comparison between weighting functions

exposure time (daytime: 6.00–22.00, night: 22.00–6.00; with the exception of the British standard in which the day starts at 7.00 and ends at 23.00) but this is not equal to the duration of vibration. ISO [7] says of the duration of measurement that it "should be sufficient to ensure reasonable statistical precision". This definition is very wide and imprecise despite the duration of vibration having a significant influence on the result of signal analysis. In the German standard [5], measurement analysis is performed in 30-second cycles which are then averaged. Generally speaking, a minimum of 30 seconds of recorded signal should be considered in data analysis in order to evaluate human exposure to vibration according to the *RMS* procedure.

Another aspect of the evaluation of human exposure to vibrations in buildings is the measurement equipment used and the localisation of measurement points. According to ISO [7] vibration transmitted to the human body should be measured on the surface between body and that surface. This regulation is imprecise; however, in the notes of the ISO standard [6] it is written that vibrations transmitted to the body should be measured in the centre of rigid surfaces (usually within 10 cm of this area). The location of the measurement point is defined as the point of entry to the body in the standard [3]. For external excitation, such as transport-induced vibrations, one or two measurement points should be located in the central part of the floor within one-third and two-thirds of the width/length of the floor, according to [3]. Measurement equipment should consist of appropriate sensors, amplifiers and, in recent years, digital recording technology. Requirements mostly concern sensors, which should be sensitive for low-frequency signals, unlike the case for acoustic purposes. Requirements for measurement equipment are described in the newest version of [9].

The criteria used with regard to human exposure to vibration in buildings depends on the evaluation method. There are four main methods in which the following parameters are considered:

- acceleration (velocity) of vibration corrected across the whole frequency range,
- spectrum (frequency structure) of the effective value (*RMS*) of acceleration (velocity) of vibration in 1/3 octave band,

- vibration dose value (*VDV*),
- maximum transient vibration value (*MTVV*).

ISO standard [6] defines the *RMS* method as a basic method of evaluation but notes that in some cases, additional methods should be used. As additional methods, ISO defines the *MTVV* method and the *VDV* method. These two methods, especially *VDV*, are recommended as additional methods in high crest factor situations. The *RMS* method averages acceleration values in the duration time:

$$a_w = \left[\frac{1}{T} \int_0^T a_w^2(t) dt \right]^{\frac{1}{2}} \tag{1}$$

where: $aw(t)$ – is the weighted acceleration as a function of time [m/s^2]; T – is the duration of measurement [s].

MTVV method also averages acceleration values but is more sensitive for occasional shocks and transient vibration by using a short integration time constant:

$$a_w(t_0) = \left[\frac{1}{\tau} \int_{t_0-\tau}^{t_0} a_w^2(t) dt \right]^{\frac{1}{2}} \tag{2}$$

$$MTVV = \max[a_w(t_0)] \tag{3}$$

where: τ – is the integration time (for running averaging, is recommended to use $\tau = 1$ s); t_0 – is the time of observation (instantaneous time).

The *VDV* method is the best for peaks in recorded signals because it uses the fourth power instead of the second power, as is used in *RMS* and *MTVV*:

$$VDV = \left[\int_0^T a_w^4(t) dt \right]^{\frac{1}{4}} \tag{4}$$

The corrected value is determined by measuring the vibration at the point at which it is transmitted to the person using the correction by means of a correction filter. This is a simple method which provides data relating to exceedance of comfort but does not include information regarding the frequency in which this exceedance appeared.

From the nineteen-eighties, not only have national and international standards changed, there has also been a lot of research conducted on human exposure to vibration. In [19] authors investigated the influence of the mode shape of motion on the human perception of vibration. During the experiment, horizontal vibrations in various shapes were induced. Vibrations were induced in clearly unidirectional directions (X or Y), and in circular and elliptical directions, all of different, very low frequencies. The participants of the experiment should identify the shapes of vibrations. The participants identified vibration evidently in one direction and vibration moving in a circular line. In the case of vibrations of elliptical motion, this identification was not so good. In [9] was also investigated the perception of harmonic

vibration and vibration of a random character. It was revealed that in the frequency range of 0.3 to 0.6 Hz, harmonic vibration is felt at a lower vibration amplitude than vibration of a random character. This means that the actual line of the vibration sensation threshold of harmonic vibrations in the considered frequency range lies lower than that of the corresponding line of random vibration.

The newest version of the Polish standard [17] was produced on the basis of an international literature review and in accordance with other international standards on that subject.

2. New Polish regulations – evaluation methods

In the newest version of the Polish standard [17], three evaluation methods are considered:

- *RMS* method of acceleration/velocity in 1/3 octave bands,
- acceleration/velocity corrected in the whole frequency range,
- vibration dose value.

The *RMS* method is considered to be a basic evaluation method and *VDV* is treated as an additional method and is described in Appendix A; this should be used as a probability of adverse comments.

The *RMS* method did not change from the old 1988 version [16] to the newest version [17] and is very close to [7]. The only differences are related to the accuracy of the acceleration values in the middle frequencies in the 1/3 octave bands which are used to determine the human perception threshold. The values of the corrected factor 'n' which are used to determine comfort levels during the daytime and night-time for different types of room (residential, office, workshops, hospitals etc.) and different types of vibrations (steady state and continuous) are the same as in [16] and in [6]. However, in [17], the new WODL ratio (in English, the human vibration perceptivity ratio) is proposed. It illustrates the percentage of exceedance of the perception threshold of vibration. This is the maximum ratio of the acceleration *RMS* value obtained from the analysis to the acceleration *RMS* value equivalent to the threshold for human perception of vibration (in the same 1/3 octave band) chosen from each 1/3 octave band. The advantage of such a coefficient is that the result of the analysis from the frequency band is not independent because the WODL clearly shows how many times the threshold for human vibration has been exceeded.

$$WODL = \max\left(\frac{a_{RMS}}{a_z}\right) \tag{5}$$

where:

aRMS – acceleration *RMS* value obtained from analysis,

az – acceleration *RMS* value equivalent to the threshold for the perception of vibration in a z-direction in the same 1/3 octave band as in *aRMS*.

The *VDV* method is the new method in [17]. This method is clearly described in [3] in which the table of levels of probability of adverse comments is shown. The methodology for determining the *VDV* value in [17] is the same like presented in standards [3] and [6]. It is

worth noting that in [6], comfort levels are not given for this evaluation method. With regard to comfort levels, the Polish standard provides the standards shown in Table 1.

Table 1. Levels of probability of adverse comments from occupants

Type of room	Time of day	Low probability of adverse comments	Adverse comments possible
		$[m/s^{1.75}]$	$[m/s^{1.75}]$
hospitals, operating theatres, precise laboratories	day and night	0.10	0.20
residential	day	0.20	0.40
	night	0.13	0.26
office	day and night	0.40	0.80
workshops	day and night	0.80	1.60

The corrected value methodology and assessment is the same as in earlier version of [16] and it is mostly used for quick diagnosis because there is no information about the frequency in which the comfort level is exceeded.

3. New Polish regulations – measurements

With regard to measurements concerning accelerations and velocities of vibrations, according to the new version of the Polish standard, measurements should be performed in the room in which occupants perceive vibrations. Measurement sensors should be placed at the points at which vibrations are transmitted to the body. Measurements should be performed in conditions in which the vibrations that are perceived by occupants have the most harmful influence. The measurement should be taken at a specific measuring point on the floor. Unless there are overriding reasons, by default, the location of the measurement point should be the geometric centre of the room. Exceptions could be when the floor is of an irregular structure or when the floor has additional structural elements which stiffen the floor structure; this is why the assistance of building engineer is required.

The basic measurement method is the recording of vibrations in the time domain at selected measuring points in the frequency range from 1 to 120 Hz. A frequency of 120 Hz is required for low-pass filtering. A filter with damping characteristics should be chosen to allow frequencies below 80 Hz to pass for evaluation.

It is recommended to use a measurement disc for measuring vibrations that are perceptible to humans; this should be placed at the measurement point. Sensors for measuring vibration parameters in three perpendicular directions should be securely fastened to the disc. Such a disc

Fig. 2. Old version of measuring disc

should be supported at three points and should have diameter of 30 cm and a mass of at least 30 kg. Additional mass should be used to reach the minimum recommended weight. Similar discs were used by the Laboratory of Structural Distortion and Vibration of the Institute of Structural Mechanics before the new version of [17] was published; this is shown in Fig. 2.

Due to the number of measuring channels and the known direction of vibrations, vertical vibrations of the floor were most often measured (Fig. 1). After analysing the results of vibration measurements, it turned out that in some cases, the mass of the disk itself - a few kilograms, was insufficient and some problems appeared. Based on experience, the disk was loading using 10 kg weights. Initially, two weights were used, and ultimately there were three on each of the measuring discs (Fig. 3).

The advantage of the measurement disk over other methods was the ability to measure vibrations in a non-invasive and non-destructive manner, which is very important in residential houses.

Fig. 3. Old version of measuring disc with three additional weights

The optimal location for weights was debatable and some problems with vibrations of additional weights occurred. This is why the need for steady mass distributions appeared. In the literature, a solution is proposed in [14]. This is a steel disk with a diameter of 300 mm and a thickness of 4 mm, with three support points (legs) positioned at angles of 120° to each other (Fig. 4).

In accordance with the USSR solution, in [18] a new disc was proposed (Fig. 5).

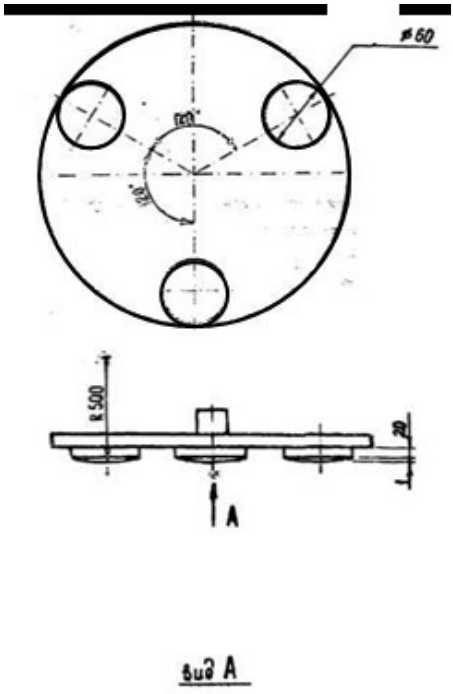

Fig. 4. Plan and cross section of the disc used in USSR

Fig. 5. New disc proposal

The proposed solution is free from the disadvantages of other previously used devices. The disk is an integral system with a sensor mounting and a load ensuring good contact of the disk with the floor surface regardless of its structure and surface layer. The disc enables non-invasive measurements and repeatability of results.

4. New Polish regulations – duration of vibration

In [6], duration of vibration is not clearly described. According to the ISO, the duration of measurement of human exposure to vibration should be sufficient to ensure statistical precision and to ensure that the vibration is typical of the exposures which are being assessed. In general, a minimum of 30 minutes should be recorded and analysed according to the ISO procedure.

In the Polish standard (both the older [16] and newer versions [17]), the duration of vibration is the range in which the vibration amplitudes are higher than 0.2 of maximum amplitude; this range should be taken for the *RMS* procedure. Moreover, one dynamic event of comfort exceedance can influence on the results of evaluation of human exposure to vibration. Polish regulations are stricter than those included in the ISO [6] or other national standards. The procedure which is in the Polish regulations is more like the *MTVV* procedure than the *RMS* procedure. The duration of vibration, in accordance with the Polish regulations, is shown in Fig. 6.

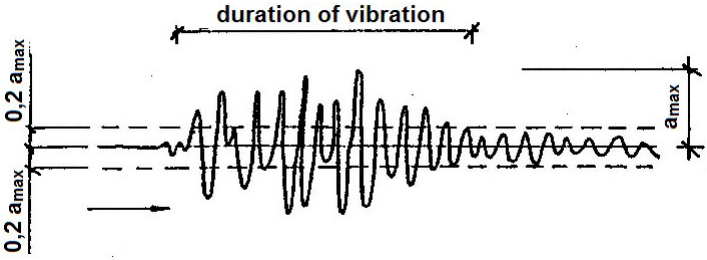

Fig. 6. Duration of vibration in accordance with [16] and [17]

The classical *RMS* method, with 30 minutes of averaging, turned out to be inadequate for transport situations. People residing close to a road, railway or tramway infrastructure complained, although the classical *RMS* procedure indicates that there is no problem with comfort exceedance. The reason for this kind of situation could be a high value of the so-called crest factor for some transport vibrations. The crest factor is defined as the modulus of the ratio of the maximum instantaneous peak value of the frequency weighted acceleration signal to its *RMS* value:

$$CF = \frac{|a_w|_{PEAK}}{a_{w\,RMS}} \tag{6}$$

For vibration with a crest factor below or equal to 9, the *RMS* method, which is called the basic method, is sufficient. However, for some types of vibration with occasional shocks, the basic evaluation method could underestimate values of discomfort. This is why an additional

method should be used in cases of higher crest factor values. In [6], it is written that the basic *RMS* method should always be used for the evaluation of human comfort with regard to vibration. However, in cases where an additional method is also used (ex. *CF* >9), both results from the basic evaluation method and from the additional evaluation method should be reported.

In the older version of Polish standard [16], it was written that regulations included in the standard can be used for crest factor values below 9. This was because in the older version, there was no additional method. In the Australian standard [2], the ranges of the crest factor are different:

- when the crest factor is lower than 6 ($CF < 6$) – *RMS* should be used,
- when crest factor is in the range of 6 to 9 ($CF \geq 6$ and $CF \leq 9$) – *RMS* and *VDV* should be used together,
- when the crest factor is higher than 9 ($CF > 9$) – *VDV* should be used.

5. Examples

To investigate accurate of the new Polish regulations, in-situ measurements were performed on a five-storey reinforced office building located in Cracow. The building is subjected to transport excitation coming from the road, the edge of which edge is 2 m from the outer wall of the analysed building. Twelve dynamic events were chosen in which, according to the *RMS* method, the comfort level is exceeded. Example of *RMS* evaluation is shown in Fig. 7.

As can be seen from Fig. 7, for the frequency band equal to 10 Hz, the comfort level is exceeded during both night and day. The crest factor in this case is 6.35. The *VDV* value for this measurement (no. 151) is 0.58 which means that according to Table 1, complaints from residents are possible. In this case, both methods yield the same result.

In Table 2, the results of the evaluation of human exposure to vibration for the twelve chosen dynamic events are listed.

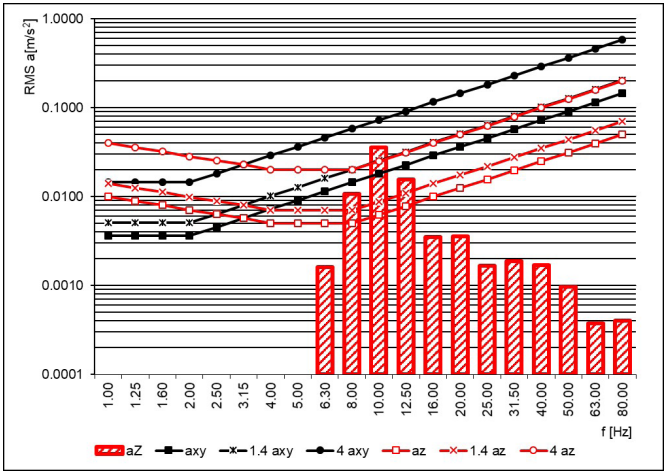

Fig. 7. *RMS* evaluation for measurement no. 151

Table 2. Results of *RMS* and *VDV* methods

Measurement no.	Time of day	Crest factor	WODL value	*VDV* value
		[-]	[-]	[m/s$^{1.75}$]
151	day	6.35	5.76	0.58
292	day	6.70	3.92	0.45
320	day	6.82	11.81	0.94
555	day	9.11	10.80	0.97
601	day	10.65	4.91	0.58
1344	night	5.33	4.03	0.50
1348	night	5.45	2.26	0.38
1385a	night	5.09	1.61	0.32
1385b	night	5.94	1.06	0.32
1397a	night	5.01	4.32	0.46
1397b	night	5.39	5.19	0.57
1407	day	7.33	2.39	0.46

In Table 2, the orange rows are dynamic events in which crest factor is higher than 9, and the yellow rows refer to cases in which the crest factor is in the range of 6 to 9.

In the dynamic events in which the crest factor is higher than 9, the evaluation of human exposure to vibration indicates that for measurement no. 555, both methods indicate exceedance of the comfort level, but for measurement no. 601, the *RMS* max is higher than 4.0 which means that the comfort level is exceeded, and *VDV* is in the mid-range between low probability and possibility of complaints.

In cases in which the crest factor is in the range of 6 to 9, in three out of four cases, the evaluations made in accordance with both methods is equal. There is one exception for measurement no. 151, in which the *RMS* max indicates that comfort level is exceeded while the *VDV* is in the mid-range.

For crest factors below 6, for all dynamic events, results of the evaluations made with the two methods differ. The *VDV* method underestimates the human perception of vibration within this range.

It is worth noting that the *RMS* procedure included in [17] is close to the *MTVV* method included in [6]. The comparison included in this paper refers to methods included in the Polish standard, and can be treated as a comparison between two additional methods from the ISO standard.

6. Conclusion

In this paper, new regulations of Polish standard [17] are clearly described. There are significant changes in this standard in comparison with the previous version. The new method of evaluation of human exposure to vibration is included in an attachment. This method,

called the *VDV* (vibration dose value), is known from such standards as: international [6], British BS [3] and Australian [2]. It is described in literature as being more sensitive to peaks in the recorded signal than the classical *RMS* method, which was introduced in [6] as the basic evaluation method.

The *RMS* method with a duration time in the region of 0.2 max amplitudes is still the basic method of evaluation in the new version of [17]. In order to improve the readability of results and to improve the quality of the assessment, the WODL ratio was proposed as an illustration of evaluation results. This ratio is very useful because it shows whether and to what extend the threshold of perception has been exceeded.

Special disc requirements were included in [17] to improve and unify measurement equipment. This is very important because according to the experience of the authors of the new Polish regulations, there were many mistakes regarding the usage of inappropriate measurement equipment. In particular, the location of measurement points and the fixing of sensors was inappropriate.

In this paper, two evaluation methods of human exposure to vibration included in the Polish standard [17] have been investigated and compared. Results show that the *RMS* max method, very close to the *MTVV* method, gives equal or higher values of evaluation than the *VDV* method. This means that results from such evaluations are on the safe side and people residing in houses designed according to these requirements are protected from the negative influence of vibrations.

The *VDV* method requires improvement; in particular, the levels of probability of adverse comments need to be changed. Additional measurements on humans in buildings in the zones of dynamic influences should be performed in order to improve this method.

References

[1] Architectural Institute of Japan, Guidelines for the evaluation of habitability to building vibration, AIJ-GEH-2004.

[2] AS 2670.2. Evaluation of human exposure to whole-body vibration Continuous and shock-induced vibration in buildings (1 to 80 Hz), 1990.

[3] British Standards Institution, BS 6472-1. Guide to evaluation of human exposure to vibration in buildings. Vibration sources other than blasting, 2008.

[4] British Standards Institution, BS 6841. Measurement and evaluation of human exposure to whole-body mechanical vibration and repeated shock, 1987.

[5] DIN 4150-2. Structural vibration, Part 2: Human exposure to vibration in buildings, 1999.

[6] International Organization for Standardization, ISO 2631-1. Mechanical vibration and shock: Evaluation of human exposure to whole-body vibration – Part 1: General requirements, 1997.

[7] International Organization for Standardization, ISO 2631-2. (2003) Mechanical vibration and shock – Evaluation of human exposure to whole-body vibration – Part 2: Vibration in buildings (1 Hz to 80 Hz).
[8] International Organization for Standardization, ISO 6897, Guidelines for the evaluation of the response of occupants of fixed structures, especially buildings and off-shore structures, to low frequency horizontal motion (0,063 to 1 Hz), 1984.
[9] International Organization for Standardization, ISO 8041-1. Human response to vibration-measuring instrumentation. Part 1: general purpose vibration meters, 2017.
[10] Kim Y.C., Tamura Y., Tanaka H., Ohtake K., Bandi E.K., Yoshida A., *Wind-induced responses of super-tall buildings with various atypical building shapes*, J. Wind Eng. Ind. Aerodyn. 133, 2014, 191–199.
[11] Kouroussis G., Verlinden O., Conti C., *Contribution of vehicle/track dynamics to the ground vibrations induced by the Brussels tramway*, Proceedings of ISMA 2including USD, 2010.
[12] Lee P.J., Lee B.K., Griffin M.J, *Evaluation of floor vibrations induced by walking in reinforced concrete buildings*, Proc. of Inter Noise Conference, Innsbruck/Austria, 15–18 September 2013, 1–6.
[13] Lombaert G., Degrande G., François S., Thompson D.J., *Ground-Borne Vibration due to Railway Traffic: A Review of Excitation Mechanisms, Prediction Methods and Mitigation Measures*, [in:] J. Nielsen et al. (eds.), *Noise and Vibration Mitigation for Rail Transportation Systems, Notes on Numerical Fluid Mechanics and Multidisciplinary Design*, vol. 126. Springer, Berlin, Heidelberg 2015.
[14] Ministry of Health of the USSR No. 2957-84, Methodological recommendations regarding the measurement and hygienic assessment of vibrations in residential buildings, 1984.
[15] Papán D., Valašková V., *Road and Railway Traffic Seismicity Effect Comparison on Historical Building in Slovakia*, IOP Conf. Ser.: Earth Environ. Sci. 44 042017, 2016.
[16] PN-B-02171:1988, Ocena wpływu drgań na ludzi w budynkach, Polish Standard 1988.
[17] PN-B-02171:2017-06, Ocena wpływu drgań na ludzi w budynkach, Polish Standard 2017.
[18] Stypuła K., Stecz P., Chełmecki J., Zgłoszenie patentowe nr W.125639, 29 września 2016.
[19] Tamura Y., Kawana S., Nakamura O., Kanda J., Nakatà S., *Evaluation perception of wind-induced vibration in buildings*, Structures & Buildings, 159, 2006, 1–11.
[20] Tatara T., Pachla F., Kuboń P., *Experimental and numerical analysis of an industrial RC tower*, Bulletin of Earthquake Engineering, Vol. 15, Iss. 5, 2017, 2149–2171.

TECHNICAL TRANSACTIONS 7/2019
CIVIL ENGINEERING
DOI: 10.4467/2353737XCT.19.075.10726
SUBMISSION OF THE FINAL VERSION: 3/06/2019

Aleksander Pistol orcid.org/0000-0002-6282-4596
aleksander.pistol@gmail.com
Piotr Krajewski orcid.org/0000-0002-2635-7273
piotrekrajewski@gmail.com
Łukasz Flaga orcid.org/0000-0001-9650-4913
lukasz.flaga@interia.pl
Andrzej Flaga orcid.org/0000-0003-1759-4872
liwpk@windlab.pl
Institute of Structural Mechanics, Cracow University of Technology

Model tests of dynamic action on the atmospheric boundary layer – concentric configuration of ventilation towers with a central ventilation chimney

Badania modelowe dynamicznego oddziaływania na warstwę przyziemną atmosfery – konfiguracja koncentryczna wież wentylacyjnych z centralnym kominem wentylacyjnym

Abstract

This paper describes model tests conducted in the Wind Engineering Laboratory of Cracow University of Technology on dynamic action on the atmospheric boundary layer in order to reduce the effects of air pollution and smog in urban areas. The paper focuses on vertical exhaust (ventilation chimney) and cooperation between a concentric system of ventilation towers and a ventilation chimney. The tests were conducted for different shapes and heights of ventilation chimneys, different diameters of the concentric system and different wind speeds provided by the ventilation towers. A heavy smoke visualisation was performed in order to qualitatively evaluate the efficiency of different solutions. The performed tests confirmed a sufficient level of efficiency of cleaning an area where the circular system is located.

Keywords: wind engineering, smog reduction, environmental engineering, urban ventilation, ventilation chimney, smoke visualisation

Streszczenie

Artykuł opisuje badania modelowe przeprowadzone w Laboratorium Inżynierii Wiatrowej Politechniki Krakowskiej dotyczące dynamicznego oddziaływania na warstwę przyziemną atmosfery w celu redukcji zanieczyszczenia powietrza i smogu w obszarach zurbanizowanych. Praca skupia się na pionowym wylocie powietrza (kominie wentylacyjnym) i współpracy pomiędzy koncentrycznym systemem wież wentylacyjnych i tym kominem. Pomiary zostały przeprowadzone dla różnych kształtów i wysokości komina, różnych średnic pierścienia wież wentylacyjnych i różnych prędkości powietrza podawanych przez wentylatory. Wykonano wizualizację dymową dla określenia jakościowego wydajności różnych rozwiązań. Badania potwierdziły wystarczającą wydajność systemu do wyczyszczenia obszaru, w którym się znajduje.

Słowa kluczowe: inżynieria wiatrowa, redukcja smogu, inżynieria środowiska, przewietrzanie miast, komin wentylacyjny, wizualizacja dymowa

1. Introduction

The deterioration of air quality is caused by the growth of industry, transportation and population, and is exacerbated by the blocking of natural ventilation channels [1]. To improve the conditions of urban areas, an idea of ventilation by dynamically forcing the movement of air mass in urban areas has been developed. However, it is crucial to examine the phenomenon of dynamic action on the atmospheric boundary layer as well as to determine whether such an action is feasible and effective.

The initial research determined the possibility of creating and maintaining an air stream through the placement of ventilation towers, either on an individual basis or arranged in a series of three parallel lines, even with large distances between the towers and with each of them producing a relatively low wind speed. It also proved to be effective on rough terrain, which simulated an urban area [2].

Despite the initial research supporting the efficiency of ventilation towers, longitudinal ventilation has its limitations due to the deterioration of the air quality as the stream length increases. Adding vertical ventilation provides an exhaust system that expels the polluted air to higher levels of the atmosphere by penetrating the smog layer which blocks natural air circulation. With this objective in mind, the idea of elevating a high chimney with fans (ventilation towers) on the bottom was developed. These fans should be able to create an airstream strong enough to penetrate the temperature inversion layer. A number of chimney shapes were tested in the Wind Engineering Laboratory of Cracow University of Technology with varying lean angles of the inlet ventilation towers and varying levels of permeability of the lower part of the chimney structure.

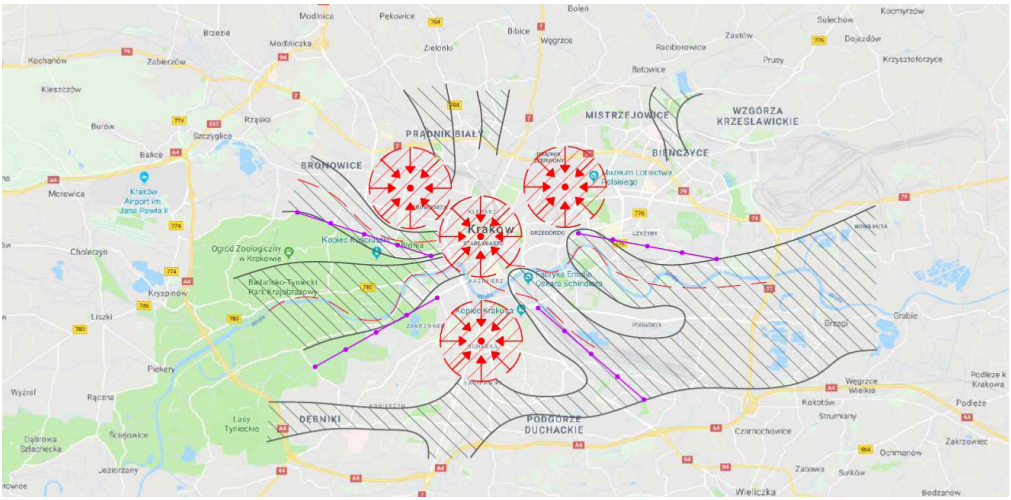

Fig. 1. Concept sketch for locating the areas for horizontal radial air stream generation and the central ventilation vertical exhaust systems on the example of an air exchange and regeneration system for Cracow [3]: black – natural ventilation channels of the city; purple – potential locations of rows of ventilation towers; red – potential location of ventilation chimneys with their supporting ventilation towers in concentric configurations

The presented system would potentially be an active solution for the smog problem. It would not limit the emission of the pollution, but would improve the aero-sanitary conditions. It would act on the polluted air or even before pollution has had a chance to accumulate by moving the air masses during wind calms. There are two basic goals of the system:

- to improve the air quality on the ground level by dispersing polluted air,
- to penetrate and break through the smog layer to enable natural air circulation.

In order to enable the results to be put into practical use, the efficiency of cooperation between the ventilation towers and the central ventilation chimney also had to be examined. A system consisting of the central ventilation chimney and an outer ring of ventilation towers located around the chimney at a certain distance from it was tested in different configurations.

The most effective and economically feasible places for the location of the system are natural ventilation channels formed by topographical and urban development. Based on the map of an air exchange and regeneration system for Cracow, Poland [3], an example of possible locations of the discussed systems is shown in Fig. 1.

2. Models, measuring devices and test method

2.1. Models

Substitute ventilation towers were used and rather than having eight to ten ventilator units uniformly distributed on both sides of the tower, these were each comprised of a single ventilator with an equivalent output of the total of the eight to ten ventilators they were substituting. These substitute ventilation units were made using 60 x 60 mm CPU fans. This resulted in 1:833 scale models. Due to the different proportions between the height and the width of the fans and the ventilation towers (80 x 20 m), only the vertical size was correctly proportioned at this scale.

The ventilation chimney was modelled as a thin shell positioned over the eight inlet ventilation towers placed under the chimney, with lean angles of 0° and 47° (see Fig. 2). The base of each chimney had a diameter of 240 mm. Four different ventilation chimney shapes were tested (see Fig. 3).

Another parameter taken into consideration were different variants of chimney shapes A & B. These variants were created by removing 25% and 50% of the height of the chimney from the top (see Fig. 4). Such variants were tested as they may prove to be vastly more economically and technically feasible to create at full scale.

The system, consisting of a ventilation chimney and ventilation towers, was planned on an octagon with eight ventilation towers located around the central chimney at distances of 150 cm and 120 cm in different series of tests. Each ventilation tower was placed on a different path and directed towards the chimney (see Fig. 5a).

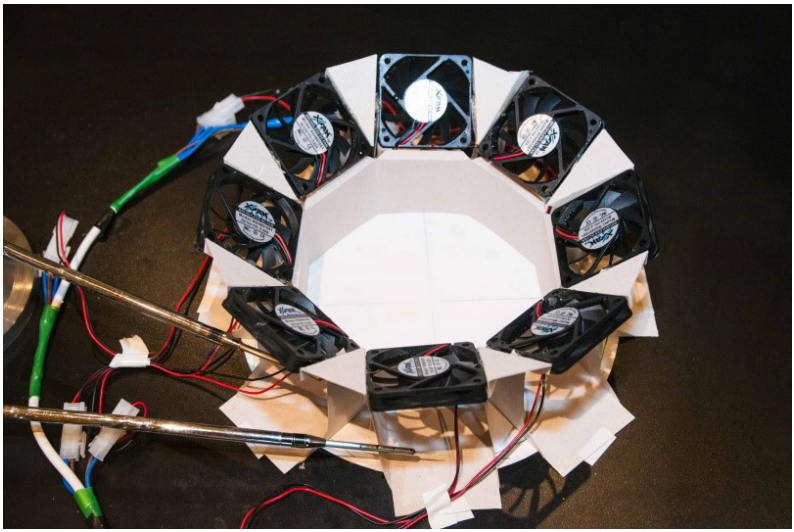

Fig. 2. Bottom of the ventilation chimney with inlet ventilation towers

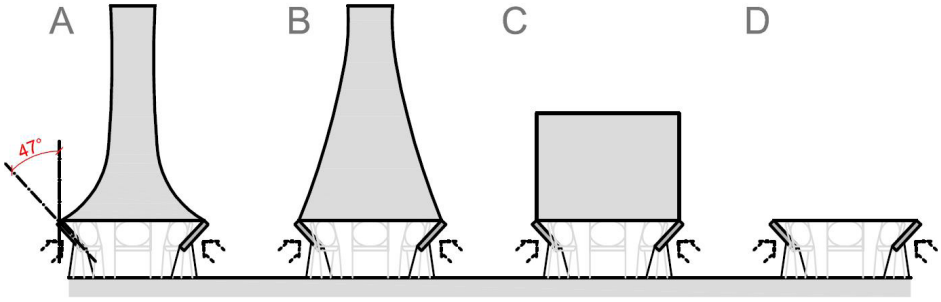

Fig. 3. Tested shapes of ventilation chimneys with inlet towers

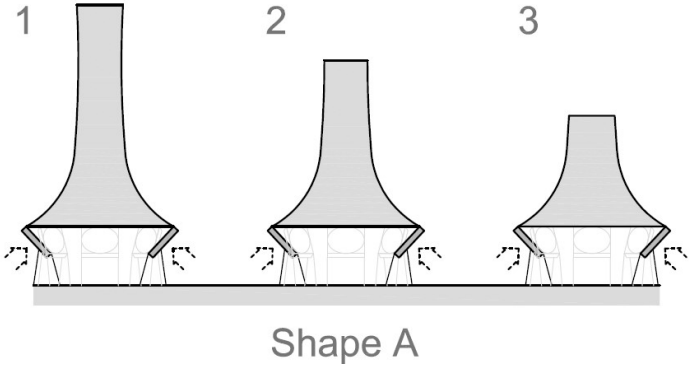

Fig. 4. Different variants of chimney shape A

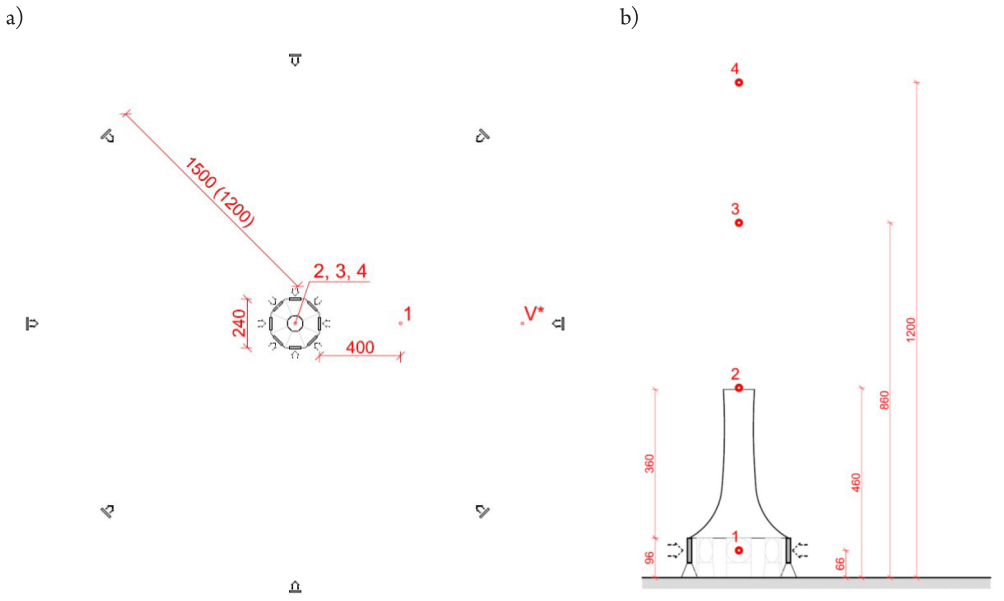

Fig. 5. Location of hot-wire probes on the model of concentric system: a) top view, b) side view

2.2. Test method and measuring devices

The main scientific aims of the investigations were:

- to find the most efficient, practical and feasible solution for the ventilation chimney, taking into account parameters such as shape, height, permeability and angle of inlet ventilation towers,
- to determine the continuity of air streams generated by ventilation towers and the possible upward exhaust resulting from combining the towers with the chimney.

This was achieved by measuring the wind speed at four different points along the path of the stream. The first measuring point of the horizontal wind speed was placed 400 mm from the outer edge of the chimney structure, along the path of one of the ventilation towers. Three other points were measuring the vertical wind speed at heights of 460 mm above the ground level (right above the chimney outlet), 860 mm above the ground level (start of the temperature inversion layer which has to be penetrated by the generated stream [4]) and 1200 mm (1 km above the ground at full scale). For a broader overlook on the location of each measuring point, see Fig. 5.

The velocity of the generated air stream was measured using ATU 2001 monofilament hot-wire anemometers. The air stream was generated through the use of CPU fans produced by *Xfan*, model: RDH6010S1 with a nominal voltage of 12 V, 0.22 A. These were powered by a stabilised DC power supply. The level of generated wind speed was controlled by adjusting the voltage provided to the fans.

2.3. Smoke visualisation

Qualitative studies were conducted using a heavy smoke generator. The ground of the workspace was clouded in heavy smoke to simulate urban air pollution (Fig. 6). The stream generation system was then turned on (Fig. 7) to observe the efficiency and thoroughness with which the area would be cleared of smoke (Fig. 8).

The smoke was made of vapour and dry ice to simulate a dense layer of smog and was dispersed uniformly in accordance with real-world urban conditions [5].

Fig. 6. Heavy fog covering ground (system turned off)

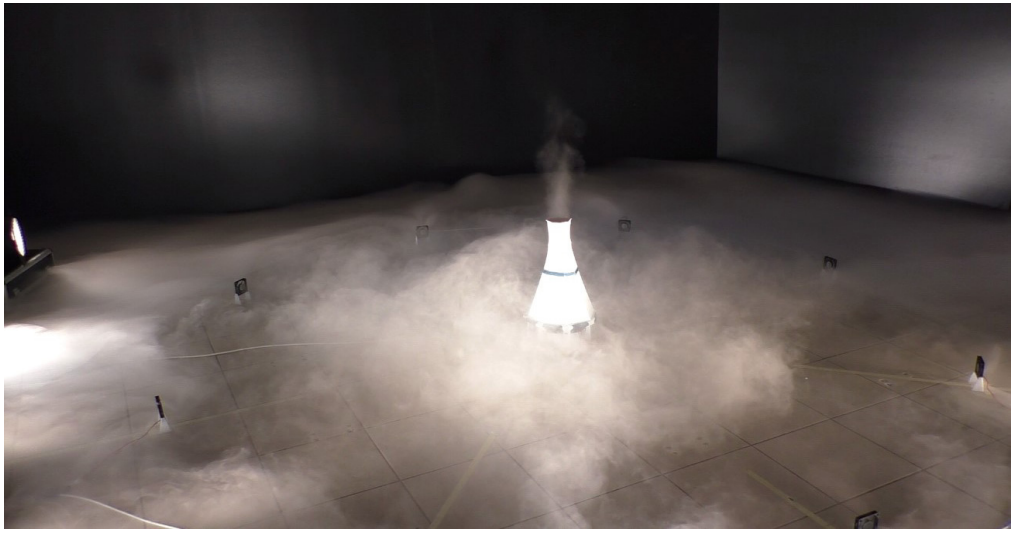

Fig. 7. Moment of turning on the system showing a visible circular gap in the fog forming due to the air movement

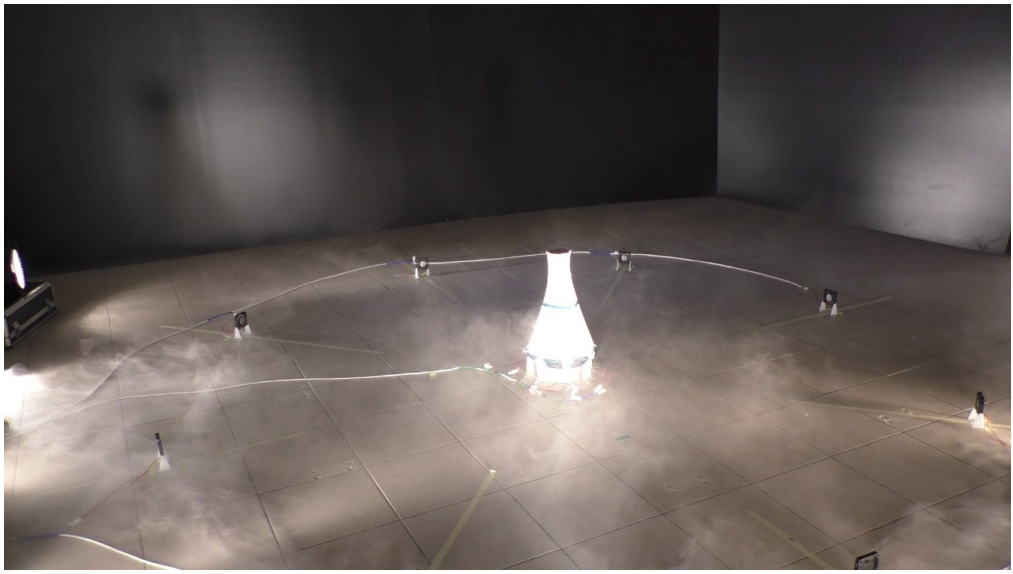

Fig. 8. Cleaned air within the circular system

During the smoke tests, a strong leak of air was observed at the bottom of the chimney. The shape of the chimney was designed to allow a sufficient level of air compression for the airstream to pass through the narrow end. A high difference of the inlet and outlet pressure was deemed to be the cause of the air leak between the fans. For this reason, tests with different types of permeability between the inlet towers have been performed. These different permeability types are shown in Fig. 9. In cases 1, 2 and 4, strong airstream leaks were observed. The best results were obtained for the third case, which was used in all of the subsequent tests [6].

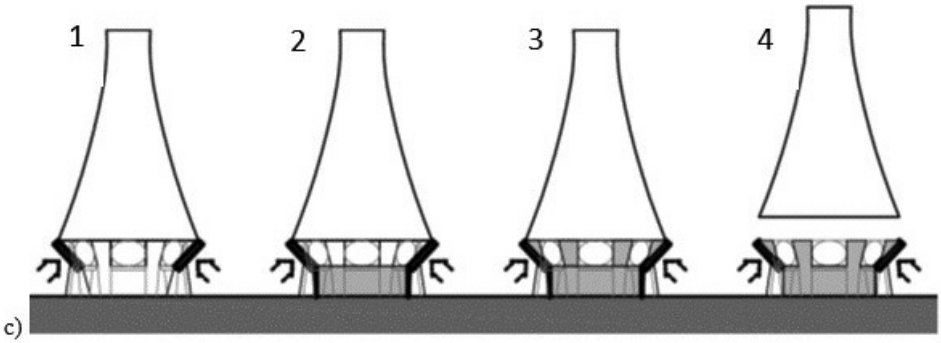

Fig. 9. Different types of permeability between the inlet ventilation towers: 1 – open space; 2 – closed space between the towers below fans level; 3 – whole space closed; 4 – whole space closed with the chimney elevated above the fans

3. Model tests and their results

The air stream velocity and continuity investigations were conducted in the three different series presented in Table 1 [7].

Table 1. Details of model test series

Series No.	Distance of 1st row of towers from the chimney	Shapes of chimney	Variants of shapes
Series I	1 500 mm	A, B, C, D	1
Series II	1 200 mm	A, B, C, D	1
Series III	1 200 mm	A, B	1, 2, 3

Each series was tested with three different wind speeds generated by the fans resulting from supplied voltages of 4.0 V, 9.5 V and 13.6 V. Comparison between the results obtained for each chimney shape at each voltage provided to the ventilation towers for Series I and II is presented in Figs. 10 and 11, respectively. The results are provided in a non-dimensional scale [8] – each velocity value is related to V^* which is the reference wind speed measured for each velocity provided by the fans at a distance of 200 mm from the outer ring of fans where the influence of the internal fan turbulence was deemed negligible. The form of the graphs (probes on horizontal axis, lines joining each points) was used solely for the purpose of presentation clarity and the lines are not meant to be interpreted as any kind of interpolation between each point.

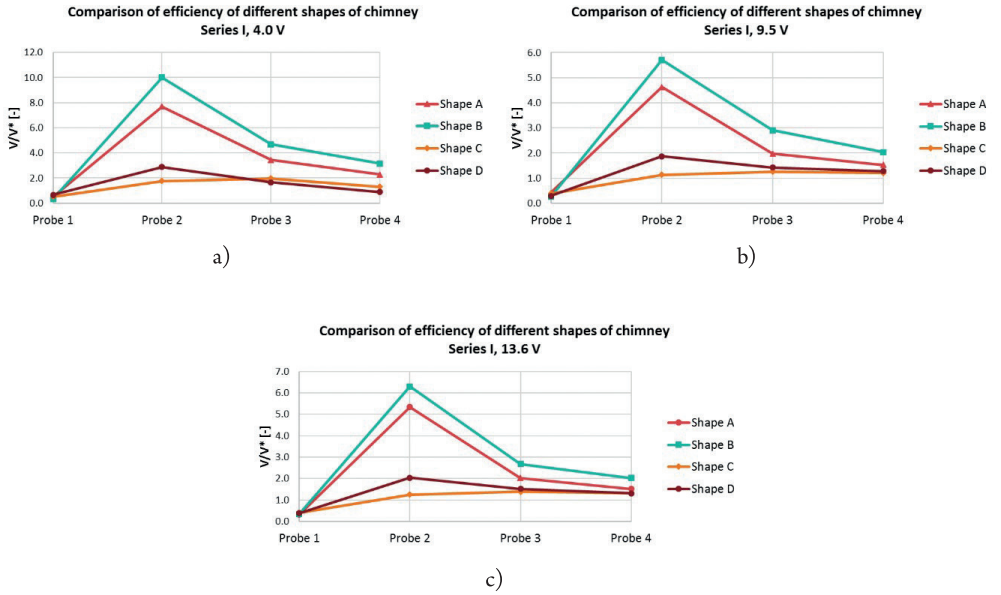

Fig. 10. Comparison between results obtained for different shapes of the chimney for Series I for a set voltage provided to the fans: a) 4.0 V, b) 9.5 V, c) 13.6 V

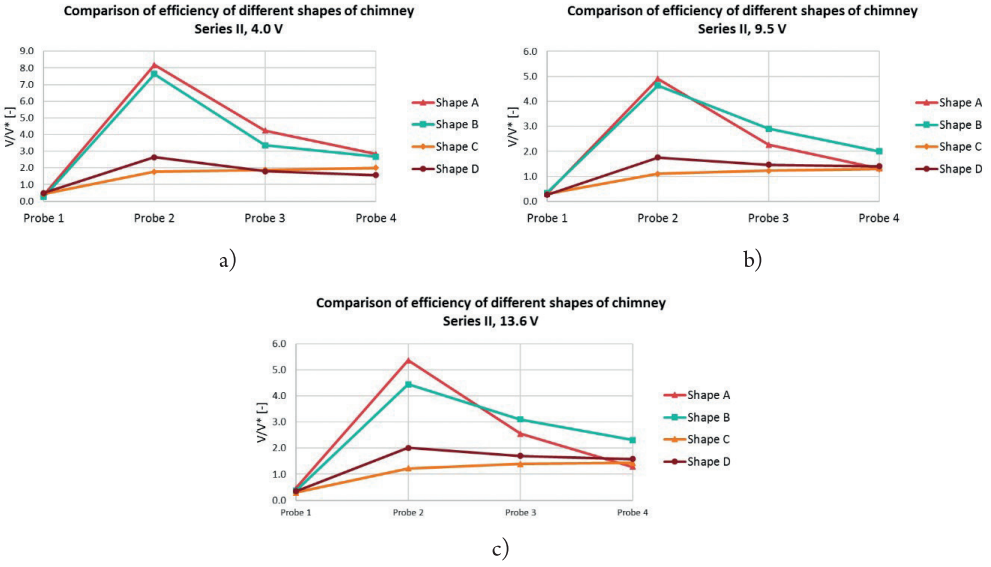

Fig. 11. Comparison between results obtained for different shapes of the chimney for Series II for a set voltage provided to the fans: a) 4.0 V, b) 9.5 V, c) 13.6 V

In order to determine the influence of the Reynolds number on the investigated phenomenon, a comparison between the results for different voltages provided to the fans (thus, different wind speeds) was performed. This comparison is shown in Figs. 12 and 13, for Series I and Series II, respectively.

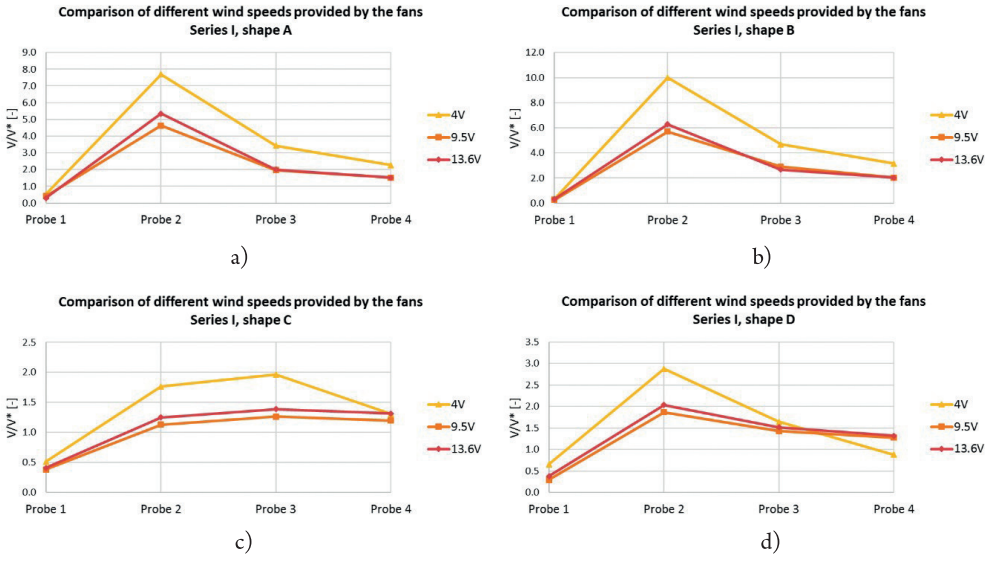

Fig. 12. Comparison between results obtained for varying voltages provided to the fans for each chimney shape – Series I: a) chimney shape A, b) chimney shape B, c) chimney shape C, d) chimney shape D

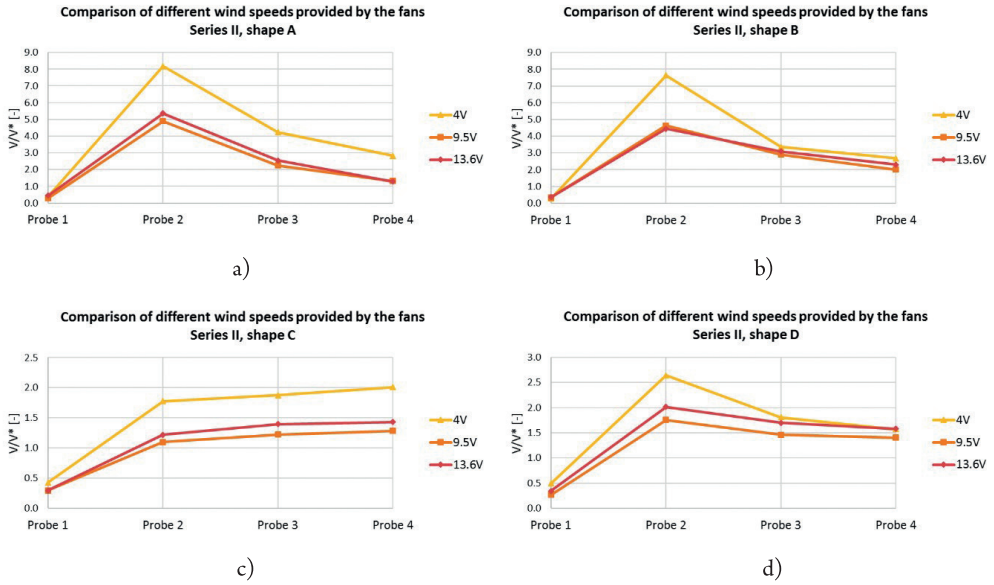

Fig. 13. Comparison between results obtained for varying voltages provided to the fans for each chimney shape – Series II: a) chimney shape A, b) chimney shape B, c) chimney shape C, d) chimney shape D

To investigate the influence of the distance of the outer ring of ventilation towers from the centre of the system, comparisons between Series I and II have been made (see Figs. 14-16).

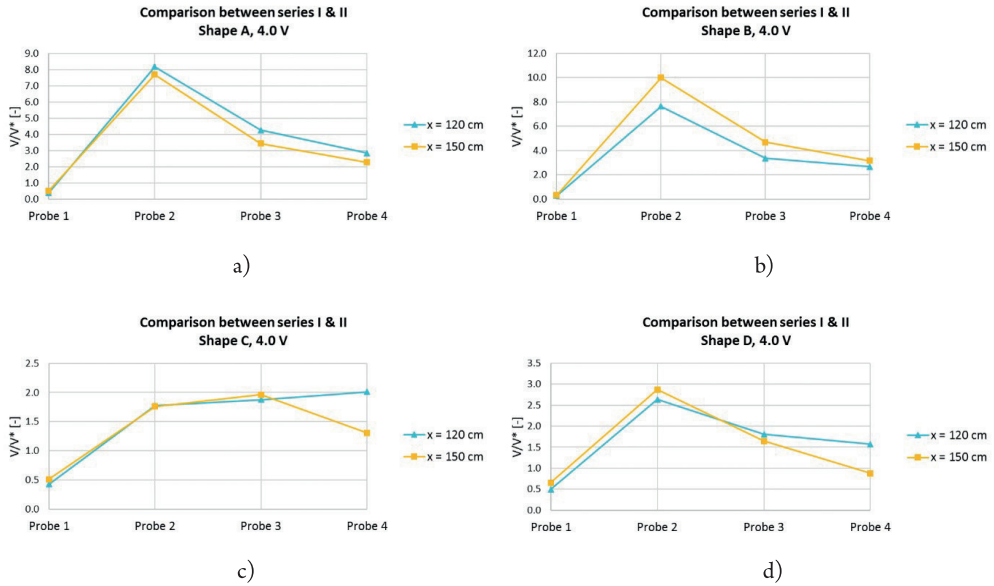

Fig. 14. Comparison between results for Series I & II for a voltage of 4.0 V: a) chimney shape A, b) chimney shape B, c) chimney shape C, d) chimney shape D

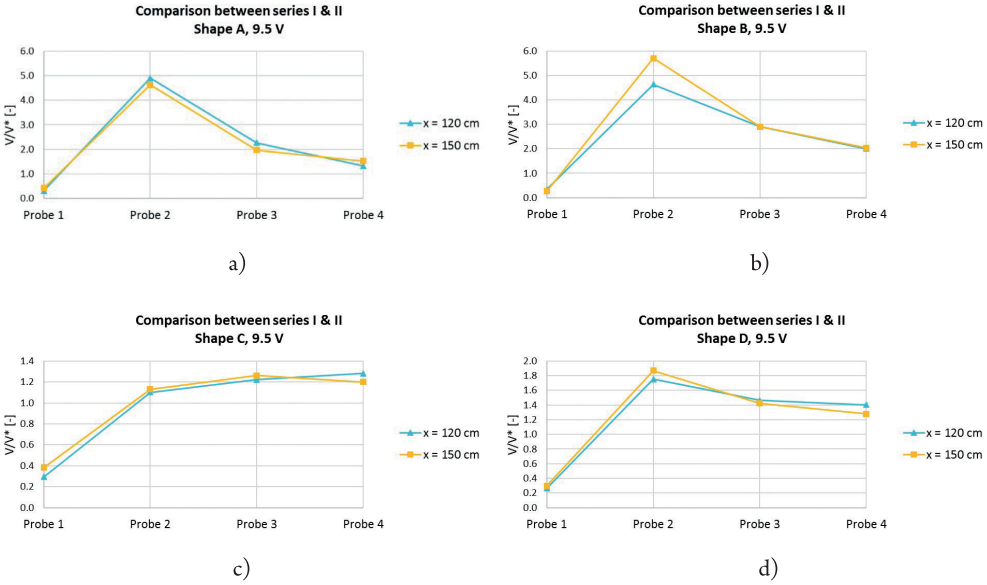

Fig. 15. Comparison between results for Series I & II for a voltage of 9.5 V: a) chimney shape A, b) chimney shape B, c) chimney shape C, d) chimney shape D

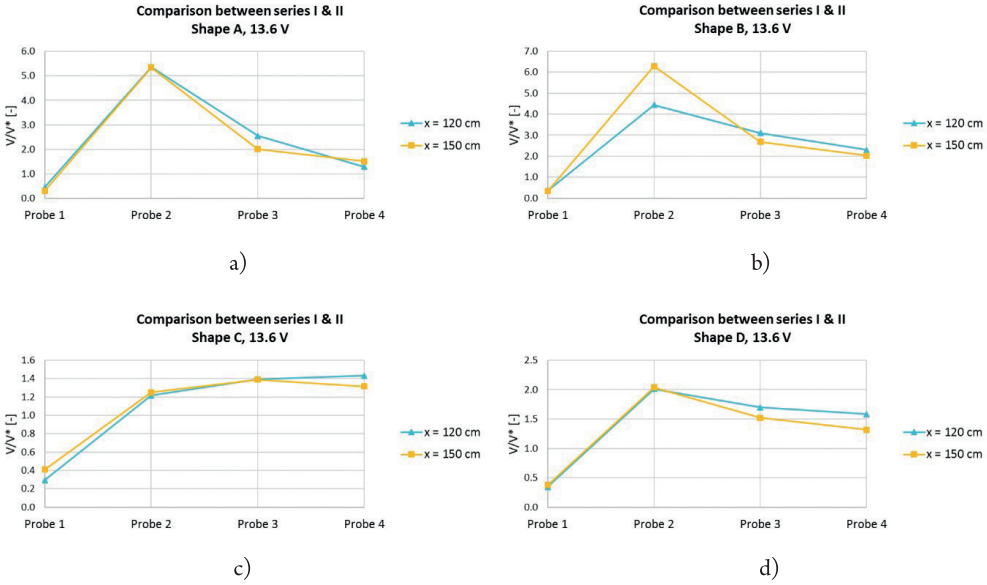

Fig. 16. Comparison between results for Series I & II for a voltage of 13.6 V: a) chimney shape A, b) chimney shape B, c) chimney shape C, d) chimney shape D

Comparisons between different variants of shapes A & B, which were conducted in Series III of the tests, are shown in Figs. 17 and 18.

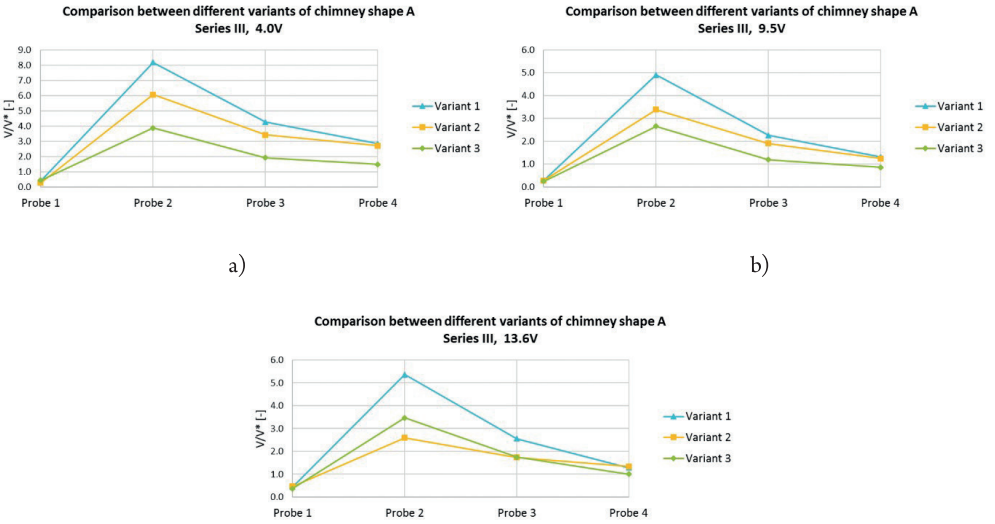

Fig. 17. Comparison between results for different variants of chimney shape A for varying voltages provided to the outer ring fans: a) 4.0 V, b) 9.5 V, c) 13.6 V

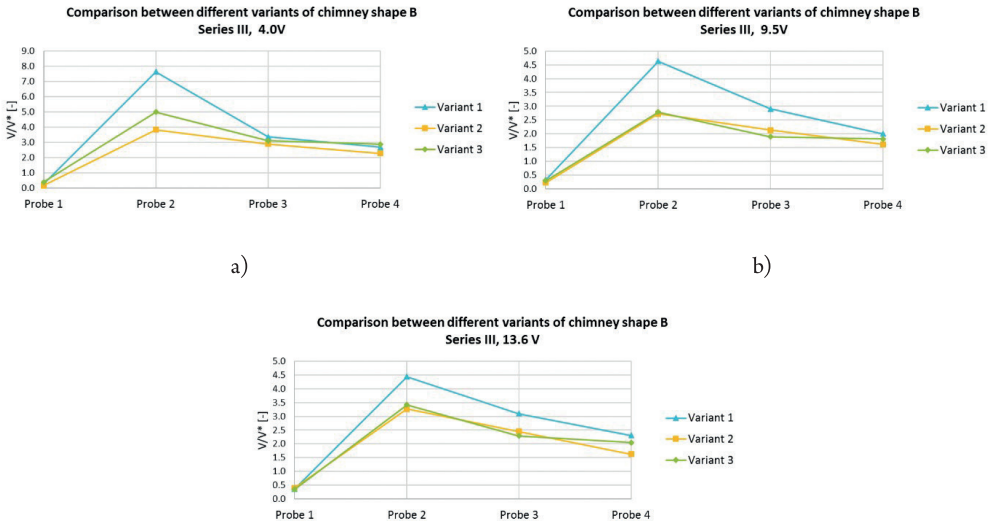

Fig. 18. Comparison between results for different variants of chimney shape B for varying voltages provided to the outer ring fans: a) 4.0 V, b) 9.5 V, c) 13.6 V

4. Results analysis and conclusions

Probe no. 1 was located at the point where the stream generated by the ventilation tower of the outer ring weakens, yet there is no noteworthy suction from the chimney inlet fans. Achieving a noticeable wind speed at this point means that there is interference between the outer ring of the ventilation towers and the inlet fans of the chimney. In practice, this would mean that the ventilation towers are able to supply the polluted air into the central vertical exhaust as a continuous airstream. For the two tested distances between the chimney and the first row of the outer ventilation towers, its influence on maintaining the continuity of the generated air stream is negligible. **The continuity was achieved** with both tested distances.

On probes no. 2 and 3, the highest wind speeds were achieved for chimney shapes A and B, which perhaps results from their forms resembling confusors. However, a similar wind speed on probe no. 4 was also achieved for shape D, which has no physical chimney at all. If verified at a larger scale, this solution would be the most advantageous for practical implementation. However, it may result in the vertical stream having too much turbulence and no longer being able to penetrate through the inversion layer. Shape C produced the most disappointing results on each measuring point in terms of wind speed; in most cases, this was slightly below the level of shape D.

The comparison of dimensionless velocity values for each tested voltage showed similarity between the graphs for 9.5 V and 13.6 V. There is a significant difference in the graph for the lowest voltage of 4.0 V, which shows there is **little influence of the Reynolds number** on the phenomenon in the investigated range of the Reynolds number for the lower values of air stream velocity. This provides the highest relative wind velocities above the chimney; however, this would not be feasible to accomplish at full scale as this wind velocity level would be too low.

Investigations of different variants of chimney shapes A and B showed that shape A produces lower wind speeds with each modification, while shape B might be **trimmed to up to half of its size with no significant deterioration of its efficiency**; furthermore, there is almost no difference between variant 2 and 3.

The most satisfying results were achieved for chimney shapes B (**highest velocity at the output of the chimney and at the inversion layer level**) and D (**most feasible solution as there is no chimney, yet the results are satisfying**). These shapes shall be tested in the forthcoming stages of the tests. At the level of temperature inversion (probe no. 3), the vertical stream achieves satisfying values of wind speed that should be able to **penetrate through the inversion layer**.

Another consideration which needs to be taken into account in future tests is the noise level generated by working ventilation towers as this may be disturbing to people. However, the estimated time of work for the fans would only be several hours a day during wind calms. Furthermore, the produced wind speed would be still at a very low level of up to 4 m/s; thus, the generated noise should not be too intrusive for people.

This work was funded by an internal grant from the Faculty of Civil Engineering of Cracow University of Technology.

References

[1] Buccolieri R., Salim S.M., Leo L. S., Di Sabatino S., Chan A., Ielpo P., de Gennaro G., Gromke Ch., *Analysis of local scale tree – atmosphere interaction on pollutant concentration in idealized street canyons and application to a real urban junction*, Atmospheric Environment 45, 2011, 1702–1713.

[2] Flaga A., Flaga Ł., Krajewski P., Augustyn A., *Badania wstępne możliwości dynamicznego oddziaływania na warstwę przyziemną. Etap I – Pomiar pola prędkości przepływu i zasięgu strumienia powietrza generowanego przez modele wentylatorów/wież wentylacyjnych w różnych wariantach ich konfiguracji*, Study report, Kraków 2017.

[3] Błażejczyk. K., *System wymiany i regeneracji powietrza jako czynnik poprawy warunków aerosanitarnych i bioklimatycznych*, B. Degórska, M. Baścik (ed.), Środowisko przyrodnicze Krakowa*, Zasoby – Ochrona – Kształtowanie*, IGiGP UJ, UMK, WGiK PW, Kraków 2013, 187–190.

[4] G. Spurr, *The penetration of atmospheric inversions by hot plumes*, Journal of Meteorology, Vol. 16, 1959, 30–37.

[5] Carpentieri M., Robins A.G., *Wind tunnel experiments of flow and dispersion in a real urban area*, The 7th International Conference on Urban Climate, 29 June – 3 July, Yokohama 2009.

[6] Flaga A., Flaga Ł., Krajewski P., Pistol A., Augustyn A., *Badania wstępne możliwości dynamicznego oddziaływania na warstwę przyziemną. Etap II – Badania w tunelu aerodynamicznym pola prędkości przepływu generowanego przez układ wentylatorów/wież wentylacyjnych w konfiguracji promienistej i specjalny membranowy komin wentylacyjny*, Study report, Kraków 2017.

[7] Flaga A., Flaga Ł., Krajewski P., Pistol A., Augustyn A., *Badania wstępne możliwości dynamicznego oddziaływania na warstwę przyziemną. Etap III – Badania w tunelu aerodynamicznym wybranych zagadnień z Etapów I i II przy uwzględnieniu wpływu chropowatości podłoża, zabudowy miejskiej)*, Study report, Kraków 2018.

[8] Flaga A., *Inżynieria Wiatrowa. Podstawy i zastosowania*. Arkady, Warszawa 2008.

If you want to quote this article, its proper bibliographic entry is as follow: Pistol A., Flaga Ł., Krajewski P., Flaga A., *Model tests of dynamic action on the atmospheric boundary layer – concentric configuration of ventilation towers with a central ventilation chimney*, Technical Transactions, Vol. 7/2019, pp. 115–128.

TECHNICAL TRANSACTIONS 7/2019
CIVIL ENGINEERING
DOI: 10.4467/2353737XCT.19.076.10727
SUBMISSION OF THE FINAL VERSION: 29/05/2019

Yasushi Uematsu orcid.org/0000-0002-9186-7835
yasushi.uematsu.d8@tohoku.ac.jp
Department of Architecture and Building Science, Tohoku University, Japan

Roma Yamamura orcid.org/0000-0002-6282-4596
r.yamamura0623@gmail.com
Central Japan Railway Company (formerly Graduate Student, Graduate School of Engineering, Tohoku University)

Wind loads for designing the main wind-force resisting systems of cylindrical free-standing canopy roofs

Obciążenia wiatrem przy projektowaniu głównych systemów odpornych na siłę wiatru cylindrycznych dachów wolnostojących

Abstract

Wind loads on cylindrical free-standing canopy roofs were investigated in a wind tunnel. First, the overall aerodynamic forces and moments were measured using a force balance. The distributions of net wind pressures provided by the difference between wind pressures on the top and bottom surfaces of the roof were then measured along two representative arc lines. Based on the results, the net wind-pressure coefficients for designing such roofs are proposed as a function of the rise-to-span ratio for two representative wind directions: one perpendicular to the eaves, the other inclined at an angle of 45° to the eaves. The roof is divided into three zones and constant net wind-pressure coefficients are specified for these zones. Two load cases providing the maximum tension and compression in the columns supporting the roof are considered as the most important load effect for discussing the design wind loads.

Keywords: cylindrical free-standing canopy roof, wind load, main wind-force resisting system, wind tunnel experiment, dynamic load effect

Streszczenie

Obciążenia wiatrem na cylindrycznych dachach wolnostojących zadaszenia zbadano w tunelu aerodynamicznym. Ogólne siły i momenty aerodynamiczne zmierzono za pomocą równowagi sił. Następnie zmierzono rozkłady ciśnień wiatru netto, które wynikają z różnicy ciśnień wiatru na górnej i dolnej powierzchni dachu, wzdłuż dwóch reprezentatywnych linii łuku. Na podstawie wyników zaproponowano współczynniki ciśnienia wiatru netto do projektowania takich dachów jako funkcję stosunku wzrostu do rozpiętości dla dwóch reprezentatywnych kierunków wiatru: jednego prostopadłego do okapu, drugiego nachylonego pod kątem 45° do okap. Dach podzielony jest na trzy strefy i dla tych stref określono stałe współczynniki ciśnienia wiatru netto. Dwa przypadki obciążeń zapewniające maksymalne naprężenie i ściskanie kolumn podtrzymujących dach są uważane za najważniejszy efekt obciążenia do omawiania obliczeniowych obciążeń wiatrem.

Słowa kluczowe: cylindryczny dach wolnostojący, obciążenie wiatrem, główny system oporu wiatru, eksperyment w tunelu aerodynamicznym, efekt obciążenia dynamicznego

1. Introduction

Free-standing canopy roofs are widely used for structures providing shade and weather protection in public spaces. The roofs are usually supported by columns and no walls. Because both sides of the roof are exposed to the flow, the wind forces acting upon the roof are more complicated than those acting upon enclosed structures. Furthermore, being light and flexible, the roofs are vulnerable to dynamic wind actions. Therefore, wind resistance is one of the most important technological problems when designing these roofs.

Although a large database of knowledge exists on wind-pressure distributions on enclosed structures of various shapes (e.g., Architectural Institute of Japan, 2015 [1]), only a few studies have been conducted on wind loading on free-standing canopy roofs. This may be due to difficulties in making models and measuring wind-pressure distributions in wind tunnel experiments. Many pressure taps are required to be installed on both the top and bottom surfaces of the roof in order to measure the distribution of net wind pressures in detail. In practice, however, the number of pressure taps is limited because the roof thickness should be as small as possible, considering the practical situation.

Regarding planar free-standing canopy roofs, such as gable and mono-sloped roofs, extensive research has been performed by several researchers, e.g., Gumley [3], Letchford and Ginger [4], Ginger and Letchford [2], Natalini et al. [6] and Uematsu et al. [10–12]. Indeed, the net wind-pressure coefficients for designing such roofs are specified in building codes and standards (e.g., Architectural Institute of Japan [1]). By comparison, only a few studies have been performed on the wind loading of curved free-standing canopy roofs. The Australian/New Zealand standard specifies the net wind-pressure coefficients for HP-shaped free-standing canopy roofs, although the range of roof geometry is rather limited. Wind loads on HP-shaped free-standing canopy roofs were studied experimentally by Uematsu et al. [13, 14] and numerically by Takeda et al. [8] for a wide range of roof geometry. Natalini et al. [7] investigated the wind loads on cylindrical free-standing canopy roofs in a wind tunnel. They measured only the mean wind pressures acting on the roof. The dynamic load effect of turbulent winds was not discussed.

The present paper investigates the design wind loads for the main wind-force resisting systems of cylindrical free-standing canopy roofs, based on measurements of the overall aerodynamic forces and moments on the roof model as well as of the distributions of the net wind-pressure coefficient along two representative arc lines on the roof. The wind tunnel models were made using a 3D printer, which made the model thickness as thin as 1 mm for the overall wind-force measurements and 2 mm for the wind-pressure measurements.

2. Experimental apparatus and procedure

Figure 1 shows the model structure under consideration together with the notation and coordinate system used in the present paper. The span B and the width W were both 15 m. The mean roof height H was fixed at 8 m regardless of the rise-to-span ratio f/B. Therefore,

the ridge height h depended on f/B, ranging from 8.8 m to 11.8 m. The wind tunnel models were made using a 3D printer with a geometric scale of $\lambda_L = 1/100$. Two series of wind tunnel experiments were performed. In the first series of experiments, the lift L and the aerodynamic moments, M_x and M_y, about the x and y axes were measured using a six-component force balance, changing the f/B ratio from 0.1 to 0.5. In the second series of experiments, the net wind-pressure distributions along two representative arc lines, referred to as lines C and E in the present paper (see Fig. 2a), were measured by using differential pressure transducers, changing the f/B ratio from 0.1 to 0.4. The roof thickness and the diameter of four columns supporting the roof were respectively 1 mm and 5 mm in the first series of experiments, and 2 mm and 6.5 mm in the second series of experiments. Figure 2b shows the wind tunnel models with $f/B = 0.2$ and 0.4 used in the second series of experiments.

The wind tunnel flow was a turbulent boundary layer simulating natural winds over typical suburban terrain. The power law exponent of the mean wind speed profile was approximately 0.22. The design wind speed U_H at the mean roof height H was determined based on the AIJ Recommendations for Loads on Buildings (2015) [1], assuming that the 'basic wind speed' U_0 is 35 m/s and the terrain category is III, which corresponds to suburban terrain. In practice, the value of U_H was calculated as 27.8 m/s. In the wind tunnel experiment, the wind speed U_H was 9 m/s for $f/B \leq 0.2$ and 10 m/s for $f/B \geq 0.3$, except in Section 3.1, where the effect of the Reynolds number on the wind-pressure distribution is investigated. The velocity scale λ_V and the time scale λ_T of the wind tunnel experiments were calculated respectively as 1/3.0 and 1/32.4 for $f/B \leq 0.2$ and 1/2.8 and 1/36.0 for $f/B \geq 0.3$. The turbulence intensity I_{uH} of the wind tunnel flow at the mean roof height H was approximately 0.16. The wind direction θ was changed from 0° to 90° with an increment of 5°, considering the symmetry of the model (see Fig. 1).

The sampling rate of measurements was 200 Hz in the first series of experiments and 500 Hz in the second series of experiments. In the second series of experiments (pressure measurements), the wind pressures at all pressure taps were measured simultaneously. The tubing effect on the measured fluctuating wind pressures was compensated for in the frequency domain by using the frequency response function of the measuring system used in the experiment. Each measurement was performed for a duration of 10 minutes at full scale. The measurements were repeated 10 times under the same condition. The statistical values of wind-pressure coefficients etc. were evaluated by applying ensemble average to the results of these consecutive 10 runs.

3. Experimental results

3.1. Effect of the Reynolds number on the wind-pressure distribution on the roof

It is well accepted that the wind pressures on curved structures are affected by the Reynolds number *Re*. This is because the location of flow separation from the structure's surface depends on *Re*. Therefore, in this section, the effect of *Re* on the wind-pressure distribution on the roof is

first investigated by changing the wind speed U_H. The Reynolds number is defined in terms of U_H and twice the radius of the curvature (R) of the cylindrical roof in the (x, z)-plane in order to relate the flow around the circular free-standing canopy roof with the flow around a circular cylinder, in which the diameter (= twice the radius) of the cylinder is usually used for defining *Re*.

In the experiment of this section, the wind speed U_H is varied from 3 to 11 m/s; the corresponding Reynolds numbers range from 0.33×10^5 to 3.09×10^5. Figures 3 and 4 respectively show the distributions of the mean values of wind-pressure coefficients, C_{pt} and C_{pb}, on the top and bottom surfaces and the net wind-pressure coefficient C_f along the centreline (line C) for $f/B = 0.1$ and 0.4, which are obtained at various Reynolds numbers. The wind direction is $\theta = 0°$. The wind-pressure coefficients are defined in terms of the velocity pressure q_H ($= 1/2\rho U_H^2$, with ρ being the air density) at the mean roof height H of the wind tunnel flow. The net wind-pressure coefficient C_f is defined as $C_f = C_{pt} - C_{pb}$. In the figure, 's' represents the coordinate along the arc line with the origin at the windward edge, normalised by the maximum value s_{max}.

When $f/B = 0.1$ (see Fig. 3), the mean C_{pt} distribution does not change with *Re*, which implies that the wind flows along the roof's top surface without separation. By contrast, when $f/B \geq 0.2$, the mean C_{pt} distribution changes with *Re*. This feature indicates that the flow separates from the roof's top surface at some point and the separation point shifts with *Re*. When $f/B = 0.2$, the separation point is close to the trailing edge of the roof; the results are not shown here in order to save space. As the f/B ratio increases, the separation point shifts windward. Figure 4 shows the results for $f/B = 0.4$. It is found that the mean C_{pt} distributon is hardly affected by *Re* when $Re > 1.0\times10^5$. This feature is consistent with the finding by Macdonald et al. [5] for cylindrical structures. They investigated the Reynolds number effect on the flow around circular cylinders by comparing the wind tunnel results obtained at various Reynolds numbers with the results of full-scale measurements on actual silos. According to their results, the wind-tunnel results obtained at $Re > 1.0\times10^5$ in a turbulent boundary layer may reasonably represent the practical full-scale situation.

The flow separates downward at the windward edge of the roof in any case of f/B. However, the mean C_{pb} distribution on the bottom surface is hardly affected by *Re*. Therefore, the change in the net wind-pressure coefficient distribution is mainly attributed to the C_{pt} distribution. In conclusion, the measurements are made at $Re > 1.0\times10^5$ in the following sections; in practice, $U_H = 9$ m/s or 10 m/s.

3.2. Comparison with the previous experimental results

Natalini et al. [7] measured the distributions of mean wind-pressure coefficients on the top and bottom surfaces of cylindrical free-standing canopy roofs. The geometry of their models was as follows: $B = 15$ cm, $W = 30$ cm or 60 cm ($W/B = 1$ or 2), $f = 3$ cm ($f/B = 0.2$), $h = 5 - 9$ cm, and the roof thickness was 2 mm. The wind tunnel flow was a turbulent boundary layer with a power law exponent of 0.24. The test condition is similar to that of the present study.

Figures 5 and 6 show the distributions of mean wind-pressure coefficients along lines E and C when $\theta = 0°$ and 30°, respectively; the f/B ratio was 0.2. The results were compared with those

of Natalini et al. [7] for $W = 30$ cm and $h = 6$ cm. It was found that both results agree relatively well with each other for the distributions along the centreline. Regarding the distributions along the edge line (line E in the present experiment), the agreement is somewhat poor, paticularly when $\theta = 30°$, although both results follow similar trends. This difference may be due to the difference in the distance between the line of pressure taps and the verge of the roof; it was 2.5 mm in the present experiment, while it was 5 mm in Natalini et al.'s experiment. The pressure distribution near the verge seems to be sensitive to the 3-dimensional effect of the flow.

Next, the present results for the mean wind-pressure coefficients on the top surface were compared with those on the enclosed buildings with circular roofs obtained in a previous study. Figure 7 shows a comparison between the present results for $f/B = 0.1$ and 0.4 and those of Ueda et al. [9] for enclosed buildings with $f/B = 0.1$ and 0.5 when $\theta = 0°$. The geometry of Ueda et al.'s model was as follows: $B = 25$ cm, $W = 50$ cm $(W/B = 2)$, and the eave height is 5 cm. The value of I_{uH} of their wind tunnel flow was approximately 0.2, which is somewhat larger than that of the present experiment.

When the f/B ratio is relatively large, the distributions on a free-standing canopy roof and enclosed building look similar to each other. The location of flow separation is almost the same. By comparison, when $f/B = 0.1$, the distributions are quite different from each other, particularly in the windward area $(s/s_{max} < 0.5)$. In the case of an enclosed building, the flow separates upward at the leading edge of the roof and then re-atchhes on the roof, generating large levels of suction near the leading edge. By contrast, in the case of a free-standing canopy roof, the flow does not separate at the leading edge and the windward area is subjected to positive (downward) wind pressures. It is thought that these flow patterns are quite different from each other. Generally speaking, it seems difficult to estimate the net wind-pressure coefficient distribution on free-standing canopy roofs from the wind-pressure distributions on the corresponding enclosed buildings, particularly for smaller values of f/B.

3.3. Mean wind-pressure distributions

Figure 8 shows the effects of f/B on the distributions of mean wind-pressure coefficients and mean net wind-pressure coefficients along line C when $\theta = 0°$. In the case of $f/B \geq 0.2$, the distribution on the top surface (a) has an inflection point, the location of which roughly corresponds to the flow separation point. As the f/B ratio increases, the location shifts windward and both the maximum and minimum pressure coefficients increase in magnitude. The distribution on the bottom surface (b) significantly changes with f/B. The flow separates downward at the leading edge of the roof. When $f/B = 0.1$, the separated flow soon re-attaches on the bottom surface of the roof and the pressure gradient is large in the separation bubble zone. By contrast, when $f/B \geq 0.3$, the bottom surface is entirely within the separation bubble and subjected to large suctions. The mean net wind pressure resulting from the difference between the mean wind pressures on the top and bottom surfaces is positive in the windward area (e.g., $s/s_{max} < 0.2$) while it is nearly constant in the leeward area (e.g., $s/s_{max} > 0.8$).

Figure 9 shows the distributions of mean wind-pressure coefficients and mean net wind-pressure coefficients along line E when $\theta = 30°$. It is found that the area of $0.5 < s/s_{max} < 0.8$ on

the top surface is subjected to high levels of suction when $f/B \geq 0.2$. This phenomenon may be due to a conical vortex generated along the leeward verge. However, the area of such high suction is thought to be limited, according to the results of Natalini et al. [7].

3.4. Aerodynamic force and moment coefficients

With regard to the aerodynamic force and moment coefficients, the lift coefficient C_L and the aerodynamic moment coefficient C_{My}, defined by Eqs. (1) and (2), are important for evaluating the design wind-force coefficients (see Uematsu et al. [11, 13]).

$$C_L = \frac{L}{q_H \cdot B \cdot W} \qquad C_{My} = \frac{M_y}{q_H \cdot R \cdot f \cdot W} \tag{1, 2}$$

Figure 10 shows the variation of mean *CL* and *CMy* values with wind direction θ. Both values become the maximum at θ≈0° when $f/B = 0.1$. However, they become the maximum at an oblique wind direction when $f/B \geq 0.2$. The wind directions providing the maximum C_L and C_{My} values increase with an increase in f/B.

The local (sectional) values of C_L and C_{My} are calculated from the C_f distribution along line C. When the wind pressures are perfectly correlated with each other in the *y* direction, the local value coincides with that for the overall roof. The results for the mean C_L and C_{My} values (local values) are plotted in Figure 11 together with those obtained from the overall wind-force measurements by using a force balance. The open and closed symbols represent the results of overall wind-force measurements and those predicted from the wind-pressure distributions along line C , respectively. When θ = 0° and 90°, both results agree well with each other. This is because the variation of wind-pressure coefficients in the *y* direction is relatively small for these wind directions. In the case of oblique winds, the difference becomes larger as the f/B ratio increases, although both results follow similar trends. The local values are generally larger in magnitude than those for the overall roof. This feature implies that we can evaluate the net wind-pressure coefficients for designing the cylindrical free-standing canopy roofs based on the wind-pressure distributions along line C, which may provide somewhat conservative estimations of the design wind loads.

3.5. Load effects

In this section, focus is on the axial forces induced in the columns as the most important load effect for discussing the design wind loads for the main wind-force resisting systems, assuming that the roof is rigid and supported by four corner columns in the same manner as in our previous studies (Uematsu et al. [11, 13]). Uematsu et al. [15, 16] investigated the application of the proposed net wind-pressure coefficients for planar free-standing canopy roofs. They examined whether the proposed net wind-pressure coefficients based on the axial forces can evaluate the other load effects appropriately and whether they can be applied to the other structural systems, such as a cantilever type. They computed the bending moments and shear forces in the columns using the proposed net wind-pressure coefficients and compared the results with the maximum

values of the bending moments and shear forces obtained from the time history analyses of these load effects, in which the time history of wind-pressure coefficients at many points on the roof was used. It was found that the proposed net wind-pressure coefficients could provide appropriate estimation of the bending moments and shear forces.

The axial forces N were computed using the time history of C_L, C_{Mx} and C_{My}, and then non-dimensionalised by $1/4q_H BW$. Figure 12 shows the variation of the maximum and minimum peak values, N^*_{max} and N^*_{min}, of the non-dimensional axial forces N^* in the columns with wind direction θ. The general behaviour of N^*_{max} and N^*_{min} with θ is similar to that of the mean C_L and C_{My} values shown in Figure 10. In the case of larger f/B ratios, such as $f/B \geq 0.3$, the values of $|N^*_{max}|$ and $|N^*_{min}|$ at θ = 30 – 45° are larger than those at θ = 0°. The difference becomes larger as the f/B ratio increases. When $f/B \geq 0.4$, the values of N^*_{max} and N^*_{min} at θ = 30 – 45° are more than twice those for θ = 0°.

The net wind-pressure coefficients for designing the cylindrical free-standing canopy roofs are usually determined on the basis of the results for θ = 0°. The results shown in Figures 10 and 12 clearly indicate that such a procedure is not appropriate for cylindrical free-standing canopy roofs with larger f/B ratios. A diagonal wind direction should be taken into account for discussing the design wind loads.

4. Discussion of design wind-force coefficients

4.1. Basic concept

In accordance with the abovementioned results, we consider two wind direction ranges, i.e., θ = 0 – 15° and 20 – 70° (referred to as 'WD0' and 'WD45', respectively), when discussing the design wind loads. The representative wind direction is 0° for WD0 and 45° for WD45. In the specification of net wind-pressure coefficients for planar free roofs (e.g., Architectural Institute of Japan [1]), the roof is divided into two zones (the windward and leeward halves) and the constant net wind-pressure coefficients are provided for these zones as a function of roof pitch. Such a zoning is not appropriate for cylindrical free-standing canopy roofs, judging from the distribution of net wind-pressure coefficients in the arc direction (see Figure 8, for example). In the present paper, the roof is therefore divided into three zones, R_1, R_2 and R_3, as shown in Figure 13, and the constant values of net wind-pressure coefficients, C_{NW}, C_{NC} and C_{NL}, are provided for these zones. Such a zoning is similar to that for enclosed buildings with cylindrical roofs in the AIJ Recommendations for Loads on Buildings (2015) [1]. This model of net wind-pressure coefficients seems reasonable for WD0 because the contour lines of net wind-pressure coefficients are almost perpendicular to the wind direction (see Natalini et al. [7]). By contrast, for WD45, the distribution of the net wind-pressure coefficient seems different from such a simple model. However, according to Figure 11, the distribution of net wind-pressure coefficients along line C can be used for evaluating the overall wind forces on the roof, assuming that the distribution in the arc direction does not change in the y-direction. Therefore, this model can also be applied to the WD45 case with some modification.

Assuming that the C_f distribution in the arc direction does not change in the y direction, the lift L and the aerodynamic moment M_y about the y axis may be given by the following equations:

$$L = \int_{-\varphi_0}^{+\varphi_0} \left(-p(\varphi)\cdot\cos\varphi\right)\cdot WRd\varphi = -q_H WR\int_{-\varphi_0}^{+\varphi_0} C_f(\varphi)\cdot\cos\varphi d\varphi \tag{3}$$

$$M_y = \int_{-\varphi_0}^{+\varphi_0} p(\varphi)\cdot WRd\varphi\cdot R\sin\varphi = = qHWR^2\int_{-\varphi_0}^{+\varphi_0} C_f(\varphi)\cdot\sin\varphi d\varphi \tag{4}$$

The definition of the symbols used in these equations is presented in Figure 13. By putting the C_f values in zones R_1, R_2 and R_3 as C_{NW}, C_{NC} and C_{NL} (constant values), respectively, and using Eqs. (1) and (2), we obtain the following equations:

$$C_L = \frac{R}{W}\left\{(C_{NW}+C_{NL})(\sin\varphi_0-\sin\varphi_1)+2C_{NC}\sin\varphi_1\right\} \tag{5}$$

$$C_{My} = \frac{R}{f}\left\{(C_{NL}-C_{NW})(\cos\varphi_0-\cos\varphi_1\right\} \tag{6}$$

Two load cases named 'A' and 'B', providing the maximum tension and compression in the columns, are considered for each wind direction range. Two sets of net wind-pressure coefficients, C_{NW}, C_{NC} and C_{NL}, are specified so that they provide the maximum tension and compression in the columns, which can be obtained from the time history of C_L, C_{Mx} and C_{My}.

It should be mentioned that C_{NW}, C_{NC} and C_{NL} include the dynamic load effect of turbulent wind. In codes and standards, the wind loads are usually presented by equivalent static loads and the dynamic load effect is taken into account by the gust effect factor. In this framework, the net wind-pressure coefficients C^*_{NW}, C^*_{NC} and C^*_{NL} for designing the main wind-force resisting systems may be provided by the following equations:

$$C^*_{NW} = \frac{\gamma\cdot C_{NW0}}{G_f},\ C^*_{NC} = \frac{\gamma\cdot C_{NC0}}{G_f},\ C^*_{NL} = \frac{\gamma\cdot C_{NL0}}{G_f} \tag{7-9}$$

where C_{NW0}, C_{NC0} and C_{NL0} are the 'basic values' of C_{NW}, C_{NC} and C_{NL}, which provide the maximum tension or compression in the columns when $\theta = 0°$ or 45°. γ represents the correction factor for evaluating the effect of wind direction on the axial forces in the columns, which is defined by the ratio of the peak axial force within the wind direction range (WD0 or WD45) to that computed from the C_{NW0}, C_{NC0} and C_{NL0} values for $\theta = 0°$ or 45°. G_f represents the gust effect factor, which is determined on the basis of the load effect, i.e., the ratio between the maximum peak and the mean values of axial forces in the columns.

4.2. Basic values of wind-force coefficients

In the case of planar free roofs, the basic values of net wind-pressure coefficients on the windward and leeward halves are determined on the basis of the combinations of C_L and C_{My},

which provide the maximum tension and compression in the columns. By contrast, in the case of cylindrical free-standing canopy roofs, the roof is divided into three zones, as shown in Figure 13. In order to determine the values of C_{NW0}, C_{NC0} and C_{NL0}, we need three conditions, two of which are given by Eqs. (5) and (6). We require one more condition; thus, we focus on the distribution of net wind-pressure coefficient C_f along the centreline for obtaining the additional condition.

Zone R_2 is the widest in area of the three zones and the net wind-pressure coefficient in this zone affects the axial forces in the columns most significantly. Figure 14 shows the maximum, mean and minimum values of the spatially-averaged net wind-pressure coefficient for Zone R_2 obtained from the C_f distribution along the centreline when $\theta = 0°$ or 45°. The minimum (negative) and the maximum (positive) values may be related to the maximum tension and compression induced in the columns. Therefore, these values are used as the basic values C_{NC0}, for WD0 and WD45.

Using Eqs. (5) and (6), we can obtain the values of C_{NW0} and C_{NL0} based on the combination of C_L and C_{My} together with the abovementioned C_{NC0} value, which provide the maximum tension (load case A) and the maximum compression (load case B) in the columns. Figure 15 shows sample results on the phase plane representation (trajectory) of the C_{My}–C_L relation for $f/B = 0.1$ and 0.3 when $\theta = 30°$. The correlation between C_{My} and C_L is positive when $f/B = 0.1$, and negative when $f/B = 0.3$. In any case, the envelope of the C_{My}–C_L trajectory can be approximated by a hexagon defined by the maximum, mean and minimum values of C_{My} and C_L, as illustrated in Figure 16. Two apexes of the hexagon provide the combinations of C_{My} and C_L for load cases A and B. The axial forces induced in the columns are computed for the six combinations of C_L and C_{My} at the six apexes and two critical conditions are then detected.

4.3. Correction factor for wind-direction effect

The maximum tension or compression may occur at a wind direction other than 0° or 45°, as Figure 12 indicates. The correction factor γ is introduced to compensate this feature. This is defined by the ratio of the practical maximum or minimum axial force, which can be obtained from a time history analysis, to the predicted values from the basic values of wind--force coefficients, C_{NW0}, C_{NC0} and C_{NL0}. The calculated results of γ, represented by γ_0 and γ_{45}, are shown in Figure 17. In some cases, the value of γ is less than 1.0, which indicates that the values of C_{NW0}, C_{NC0} and C_{NL0} estimated in the previous section are so conservative that they provide larger axial forces than the practical peak values. For evaluating the design wind-force coefficients, the value of γ is replaced by 1.0 when $\gamma < 1.0$.

4.4. Gust effect factor

Figure 18 shows the gust effect factor, defined by the ratio of the maximum or the minimum to the mean axial force induced in the columns, plotted as a function of the mean reduced axial force N^*_{mean} for all f/B ratios and wind directions. When the value of $|N^*_{mean}|$ is small, G_f exhibits a large value. However, with an increase in $|N^*_{mean}|$, the values of Gf

collapse into a narrow range of around $G_f = 1.8$. This value of G_f corresponds to a peak factor of $g_f \approx 2.1$, based on the quasi-steady assumption (i.e., $G_f \approx (1+g_v I_{uH})^2 \approx (1+2.1\times0.16)^2 = 1.8$). Therefore, $G_f = 1.8$ is used for evaluating the design wind-force coefficients in the present paper. In practical applications, the value of G_f specified in building codes and standards for each terrain category can be used for evaluating the design wind loads. The value of g_v mentioned above is somewhat smaller than those used in conventional building design. The reason for this is not clear at present, but it may be related to the turbulence scale of the approach flow. The longitudinal turbulence scale of wind tunnel flow is of the same order of the model size. Therefore, the dynamic load effect may be relatively small compared with the practical ones.

4.5. Net wind-pressure coefficients for designing the main wind-force resisting systems

The net wind-pressure coefficients obtained from the abovementioned procedure are summarised in Table 1. It is found that the values of net wind pressure for WD45 are rather large in magnitude compared with those for WD0, particularly for larger f/B ratios. This is due to the flow separation from the top surface of the roof, which generates large levels of suction in the leeward region.

5. Concluding remarks

The net wind-pressure coefficients for designing the main wind-force resisting systems of cylindrical free-standing canopy roofs have been investigated based on wind tunnel experiments on the wind-pressure distributions along two representative arc lines as well as on the aerodynamic forces and moments acting on the whole roof. The wind tunnel models were made using a 3D printer, which made the roof thickness as thin as 1 mm or 2 mm.

First, a discussion was presented of the effect of the Reynolds number on the wind--pressure distribution on the top surface by changing the wind speed U_H at the mean roof height H over a wide range. The Reynolds number Re is defined in terms of U_H and twice the radius of curvature of the cylindrical roof. When Re is larger than approximately 1.0×10^5, the wind-pressure distribution is minutely affected by Re. The wind-pressure distribution reasonably represents the full-scale practical situation.

The effects of rise-to-span ratio f/B and wind direction θ on the wind-pressure coefficients acting on the roof were then investigated. It was found that the overall wind forces can be evaluated by the local distribution of net wind-pressure coefficients along the centreline. The distribution of the net wind-pressure coefficient along the centreline significantly changed with θ.

Finally, the net wind-pressure coefficients, C^*_{NW}, C^*_{NC} and C^*_{NL}, for designing the main wind-force resisting systems were proposed for two wind direction ranges: $\theta = 0$–$15°$ (WD0) and $\theta = 20$–$70°$ (WD45). The roof was divided into three zones (windward, central and leeward) and the wind-force coefficients for these zones were provided as a function of f/B.

For discussing the design wind loads, focus was on the axial forces induced in the columns as the most important load effect, assuming that the roof is rigid and supported by four corner columns. Two load cases providing the maximum tension and compression in the columns were considered; two sets of C^*_{NW}, C^*_{NC} and C^*_{NL} were provided as a function of f/B for both WD0 and WD45. For evaluating the design wind loads, the gust effect factor approach was employed.

The present study was financially supported by the Nohmura Foundation for Membrane Structure's Technology (2015).

References

[1] Architectural Institute of Japan, Recommendations of Loads on Buildings, 2015 (in Japanese).

[2] Ginger J.D., Letchford C.W., *Wind loads on planar canopy roofs, Part 2 Fluctuating pressure distributions and correlations*, Journal of Wind Engineering and Industrial Aerodynamics, Vol. 51, 1994, 353–370.

[3] Gumley S.J., *A parametric study of extreme pressures for the static design of canopy structures*, Journal of Wind Engineering and Industrial Aerodynamics, Vol. 16, 1984, 43–56.

[4] Letchford C.W., Ginger J.D., *Wind loads on planar canopy roofs, Part 1 Mean pressure distributions*, Journal of Wind Engineering and Industrial Aerodynamics, Vol. 45, 1992, 25–45.

[5] Macdonald P.A., Kwok K.C.S., Holmes J.D., *Wind loads on circular storage bins, silos and tanks: I. Point pressure measurements on isolated structures*, Journal of Wind Engineering and Industrial Aerodynamics, Vol. 31, 1988, 165–188.

[6] Natalini B., Marighetti J.O., Natalini M.B., *Wind tunnel modeling of mean pressures on planar canopy roof*, Journal of Wind Engineering and Industrial Aerodynamics, Vol. 90, 2002, 427–439.

[7] Natalini M.B., Morel C., Natalini B., *Mean loads on vaulted canopy roofs*, Journal of Wind Engineering and Industrial Aerodynamics, Vol. 119, 2013, 102–113.

[8] Takeda F., Yoshino T., Uematsu Y., *Design wind force coefficients for hyperbolic paraboloid free roofs*, Journal of Physical Science and Application, Vol. 4(1), 2014, 1–19.

[9] Ueda H., Hagura H., Oda H., *Characteristics of stress generated by wind pressures and wind loads acting on stiff two-hinged arches supporting a barrel roof*, Journal of Structural and Construction Engineering, Architectural Institute of Japan, Vol. 496, 1997, 29–35 (in Japanese).

[10] Uematsu Y., Iizumi E., Stathopoulos T., *Wind loads on free-standing canopy roofs: Part 1 local wind pressures*, Journal of Wind Engineering and Industrial Aerodynamics, Vol. 96, 2008, 1015–1028.

[11] Uematsu Y., Iizumi E., Stathopoulos T., *Wind loads on free-standing canopy roofs: Part 2 overall wind forces*, Journal of Wind Engineering and Industrial Aerodynamics, Vol. 96, 2008, 1029–1042.

[12] Uematsu Y., Sakurai H., Miyamoto Y., Gavanski E., *Wind force coefficients for designing porous canopy roofs*, Journal of Civil Engineering and Architecture, Vol. 7(9), 2013, 1047–1055.
[13] Uematsu Y., Miyamoto Y., Gavanski E., *Wind loading on a hyperbolic paraboloid free roof,* Journal of Civil Engineering and Architecture, Vol. 8(10), 2014, 1–19.
[14] Uematsu Y., Miyamoto Y., Gavanski E., Effects of porosity on the *Wind loads on a hyperbolic paraboloid canopy roof.* Journal of Civil Engineering and Architecture, Vol. 9(6), 2015, 715–726.
[15] Uematsu Y., Iizumi E., Stathopoulos, T., *Wind loads on free-standing canopy roofs Part 3 Validity and application of the proposed wind force coefficients*, Journal of Wind Engineering, JAWE, Vol. 31(4), 2006, 115–122 (in Japanese).
[16] Uematsu Y., Iizumi E., Stathopoulos, T., *Wind force coefficients for the main wind force resisting system of a free-standing canopy roof of cantilever type*, Proceedings of the 19th National Symposium on Wind Engineering, 2006, 343–348 (in Japanese).

If you want to quote this article, its proper bibliographic entry is as follow: Uematsu Y., Yamamura R., *Wind loads for designing the main wind-force resisting systems of cylindrical free-standing canopy roofs*, Technical Transactions, Vol. 7/2019, pp. 129–148.

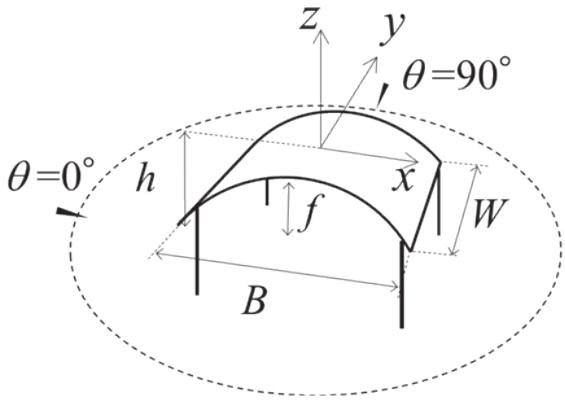

Fig. 1. Model building and coordinate system

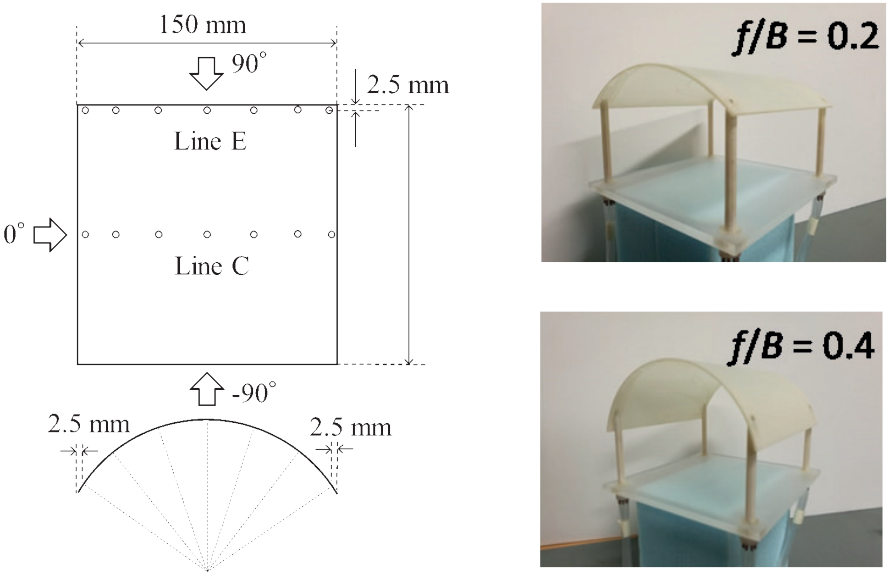

(a) Layout of pressure taps

(b) Pictures

Fig. 2. Wind tunnel models for pressure measurements

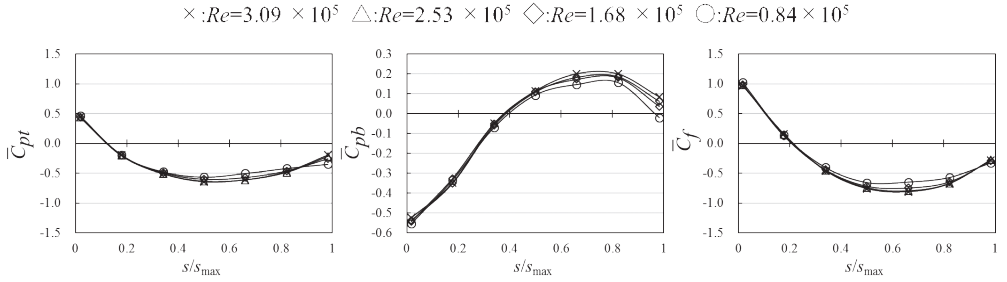

(a) $\overline{C}_{pt}$ (b) $\overline{C}_{pb}$ (c) $\overline{C}_{f}$

Fig. 3. Distributions of the mean wind-pressure coefficients and the net wind-pressure coefficients (f/B = 0.1, θ = 0°, line C)

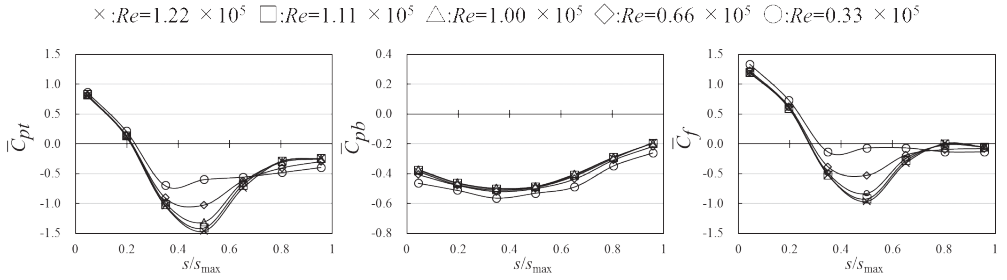

(a) $\overline{C}_{pt}$ (b) $\overline{C}_{pb}$ (c) $\overline{C}_{f}$

Fig. 4. Distributions of the mean wind-pressure coefficients and the net wind-pressure coefficients (f/B = 0.4, θ = 0°, line C)

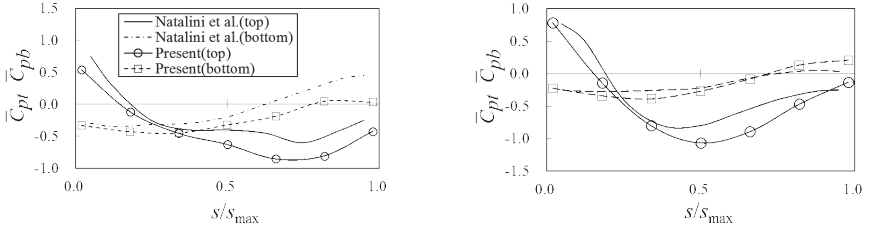

(a) Line E (b) Line C

Fig. 5. Distributions of the mean wind-pressure coefficients along lines E and C when f/B = 0.2 and θ = 0°: comparison between the present and previous experiments

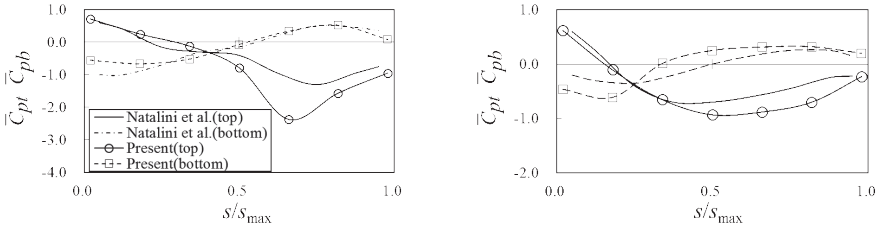

(a) Line E (b) Line C

Fig. 6. Distributions of the mean wind-pressure coefficients along lines E and C when $f/B = 0.2$ and $\theta = 30°$: comparison between the present and previous experiments

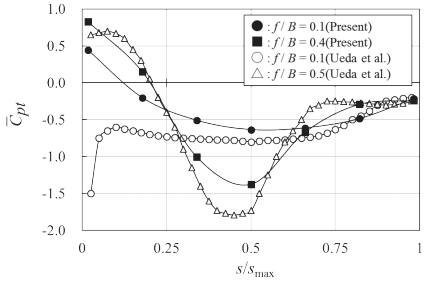

Fig. 7. Mean wind-pressure coefficients on the top surface: a comparison with those on enclosed structures

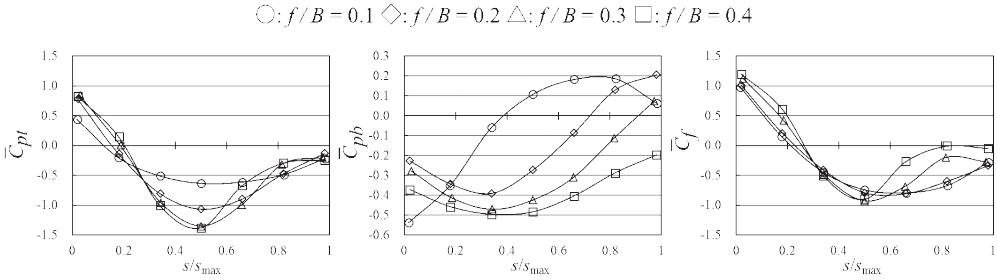

(a) $\overline{C}_{pt}$ (b) $\overline{C}_{pb}$ (c) $\overline{C}_{f}$

Fig. 8. Distributions of the mean wind-pressure coefficients and the net wind-pressure coefficients along line C ($\theta = 0°$)

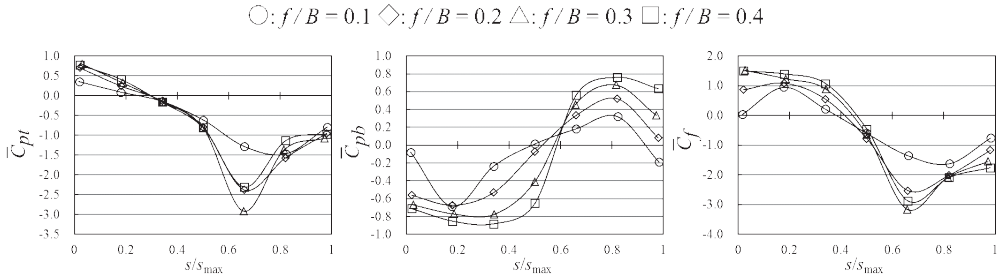

(a) $\overline{C}_{pt}$ (b) $\overline{C}_{pb}$ (c) $\overline{C}_{f}$

Fig. 9. Distributions of the mean wind-pressure coefficients and the net wind-pressure coefficients along line E (θ = 30°)

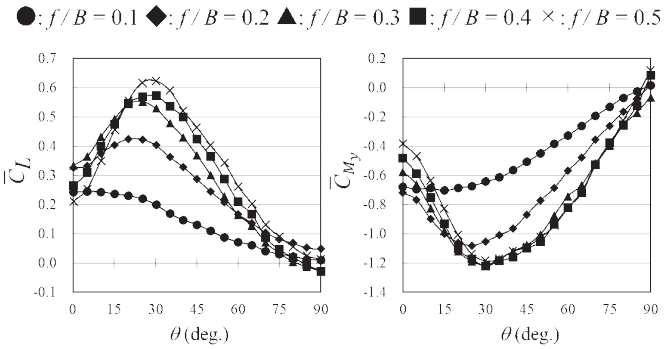

(a)C_L (b) $\overline{C}_{My}$

Fig. 10. Variation of the mean C_L and C_{My} values with θ

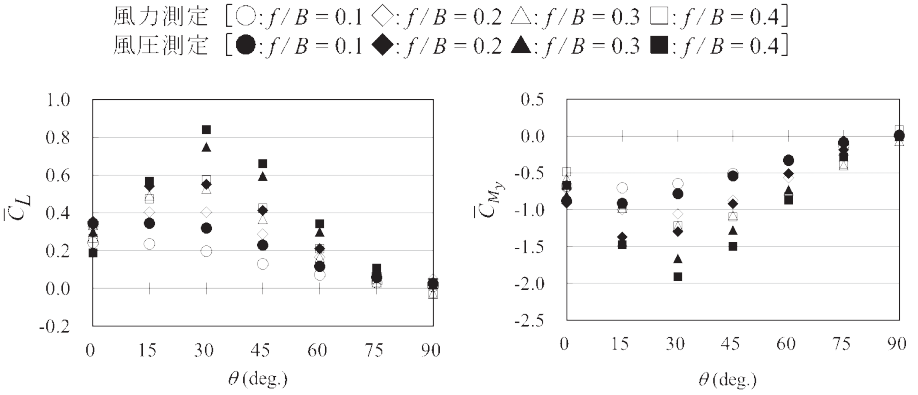

(a)C_L (b) $\overline{C}_{My}$

Fig. 11. Comparison between the local and overall values for the mean C_L and C_{My} values

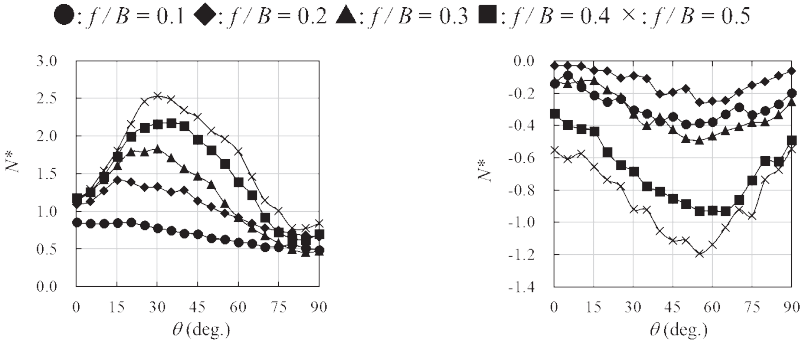

(a) N^*_{max} (tension) (b) N^*_{min} (compression)

Fig. 12. Variation of N^*_{max} and N^*_{min} with wind direction θ

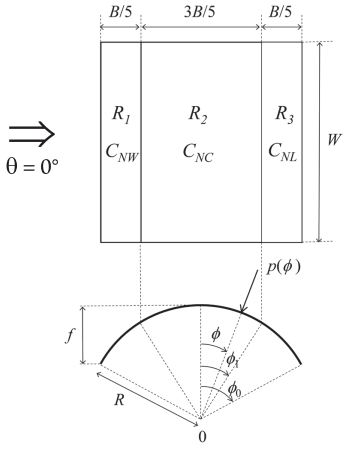

Fig. 13. Zoning of the roof and wind-force coefficients

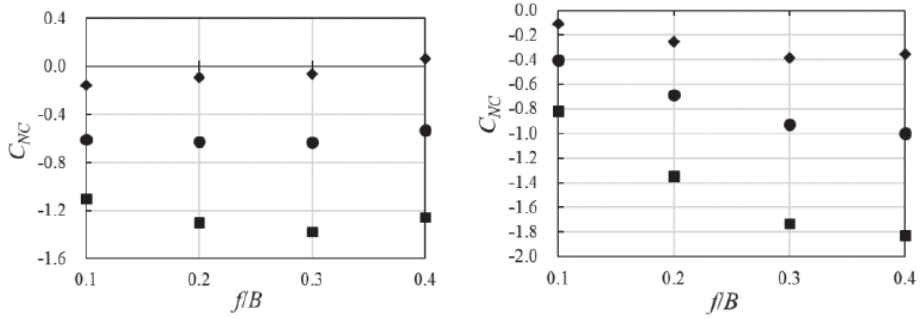

(a) θ = 0° (b) θ = 45°

Fig. 14. Spatially-averaged wind force coefficient for Zone R_2

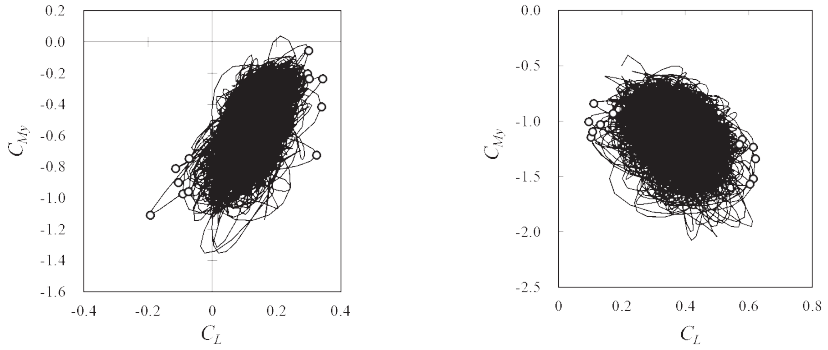

(a) $f/B = 0.1$ (b) $f/B = 0.3$

Fig. 15. C_{My}–C_L trajectory ($\theta = 30°$)

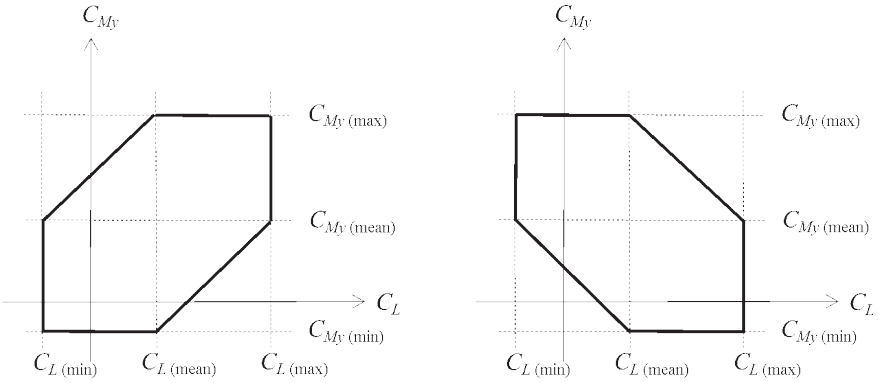

(a) Positive correlation (b) Negative correlation

Fig. 16. Model of the envelope of the C_{My}–C_L trajectory

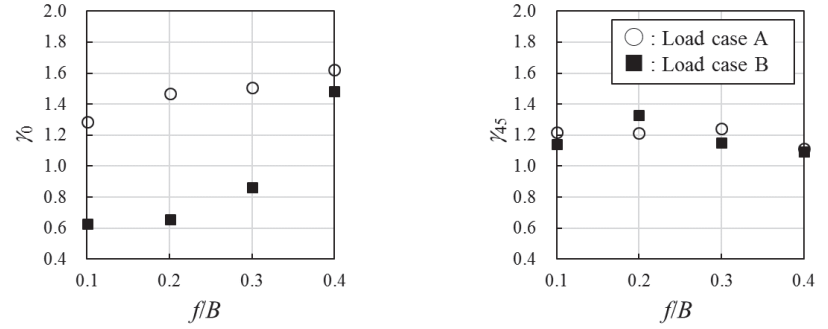

(a) WD0 (b) WD45

Fig. 17. Correction factor for the wind-direction effect on the maximum and minimum column axial forces

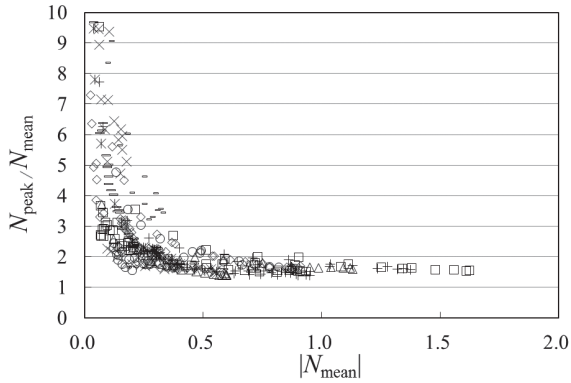

Fig. 18. Gust effect factor based on the load effect

Table 1. Design wind-force coefficients

(a) Wind direction WD0

		C^*_{NW}		C^*_{NC}		C^*_{NL}	
Load case		A	B	A	B	A	B
f/B	0.1	1.3	0.6	−0.5	0.0	−0.5	−0.4
	0.2	0.8	0.1	−0.6	0.0	−1.0	−0.3
	0.3	0.8	0.2	−0.7	0.0	−1.0	−0.4
	0.4	0.9	0.3	−0.8	0.0	−0.7	−0.7

(b) Wind direction WD45

		C^*_{NW}		C^*_{NC}		C^*_{NL}	
Load case		A	B	A	B	A	B
f/B	0.1	0.2	0.7	−0.6	0.0	−0.4	−0.4
	0.2	0.8	0.6	−0.7	−0.1	−1.0	−1.3
	0.3	0.8	0.8	−0.8	−0.3	−1.1	−2.3
	0.4	0.7	0.8	−0.8	−0.4	−1.3	−2.7